

WL-TR-1997-7051

**Ultra-Wideband Antennas and Propagation
Vol. 4: Impulse Propagation Measurements of Water,
Dry Sand, Moist Sand, and Concrete**

Everett G. Farr and Charles A. Frost

Farr Research, Inc.
614 Paseo Del Mar NE
Albuquerque, NM 87123

Contract No. F08630-95-C-0014

JULY 1997

FINAL REPORT FOR PERIOD APRIL 1995 - APRIL 1997

Approved for public release; distribution is unlimited.

19970828 086

DTIC QUALITY INSPECTED 4

WRIGHT LABORATORY, ARMAMENT DIRECTORATE

Air Force Materiel Command ■ United States Air Force ■ Eglin Air Force Base

REPORT DOCUMENTATION PAGE

Form Approved
OMB No. 0704-0188

Public reporting burden for this collection of information is estimated to average 1 hour per response, including the time for reviewing instructions, searching existing data sources, gathering and maintaining the data needed, and completing and reviewing the collection of information. Send comments regarding this burden estimate or any other aspect of this collection of information, including suggestions for reducing this burden, to Washington Headquarters Services, Directorate for Information Operations and Reports, 1215 Jefferson Davis Highway, Suite 1204, Arlington, VA 22202-4302, and to the Office of Management and Budget, Paperwork Reduction Project (0704-0188), Washington, DC 20503.

1. AGENCY USE ONLY (Leave blank)		2. REPORT DATE July 1997	3. REPORT TYPE AND DATES COVERED Final Report April 1995 - April 1997	
4. TITLE AND SUBTITLE Ultra-Wideband Antennas and Propagation Vol. 4: Impulse Propagation Measurements of Water, Dry Sand, Moist Sand, and Concrete			5. FUNDING NUMBERS C: F08635-95-C-0014 PE 65502F PR 3005 TA 41 WU 51	
6. AUTHOR(S) Farr, Everett G. Frost, Charles A.				
7. PERFORMING ORGANIZATION NAME(S) AND ADDRESS(ES) Farr Research, Inc. 614 Paseo Del Mar NE Albuquerque, NM 87123			8. PERFORMING ORGANIZATION REPORT NUMBER	
9. SPONSORING/MONITORING AGENCY NAME(S) AND ADDRESS(ES) Wright Laboratory, Armament Directorate Fuzes Branch 306 W. Eglin Blvd., Bldg 432 Eglin Air Force Base, FL 32542-5430			10. SPONSORING/MONITORING AGENCY REPORT NUMBER WL-TR-1997-7051	
11. SUPPLEMENTARY NOTES This is Volume 4 of four volumes.				
12a. DISTRIBUTION/AVAILABILITY STATEMENT Approved for public release; distribution is unlimited.			12b. DISTRIBUTION CODE	
13. ABSTRACT (Maximum 200 words) In this report we continue the measurement and analysis of the complex dielectric constant of water that was begun in Volume 3. Furthermore, we provide measurements and analyses of dry sand, moist sand, and concrete. We also fit Debye and Lorentz models to the measured dielectric constant curve using a least mean square algorithm. Finally, we calculate how impulses with various pulse widths would propagate through these media.				
14. SUBJECT TERM Dielectric Constant, Coaxial Test Fixture, Debye Model, Lorentz Model, Sand, Concrete			15. NUMBER OF PAGES 112	
			16. PRICE CODE	
17. SECURITY CLASSIFICATION OF REPORT UNCLASSIFIED	18. SECURITY CLASSIFICATION OF THIS PAGE UNCLASSIFIED	19. SECURITY CLASSIFICATION OF ABSTRACT UNCLASSIFIED	20. LIMITATION OF ABSTRACT UL	

Small Business Innovation Research Program (SBIR)

NOTICE

WHEN GOVERNMENT DRAWINGS, SPECIFICATIONS, OR OTHER DATA ARE USED FOR ANY PURPOSE OTHER THAN IN CONNECTION WITH A DEFINITE GOVERNMENT-RELATED PROCUREMENT, THE UNITED STATES GOVERNMENT INCURS NO RESPONSIBILITY OR ANY OBLIGATION WHATSOEVER. THE FACT THAT THE GOVERNMENT MAY HAVE FORMULATED OR IN ANY WAY SUPPLIED THE SAID DRAWINGS, SPECIFICATIONS, OR OTHER DATA IS NOT TO BE REGARDED BY IMPLICATION, OR OTHERWISE IN ANY MANNER CONSTRUED, AS LICENSING THE HOLDER, OR ANY OTHER PERSON OR CORPORATION; OR AS CONVEYING ANY RIGHTS OR PERMISSION TO MANUFACTURE, USE, OR SELL ANY PATENTED INVENTION THAT MAY IN ANY WAY BE RELATED THERETO.

This report is approved for public release; distribution is unlimited.

Contract Number: F08630-95-C-0014

Contractor: Farr Research, Inc.

This technical report has been reviewed and is accepted under the provisions of the Small Business Innovation Research Program.

Ellis E. Youngblood

ELLIS E. YOUNGBLOOD
Contract Monitor

Aaron D. Brinson

AARON D. BRINSON
Technical Director, Munitions Division

Publication of this report does not constitute approval or disapproval of the ideas or findings. It is published in the interest of the scientific and technical information exchange. Copies of this report should not be returned unless return is required by security considerations, contractual obligations, or notice on a specific document.

Table of Contents

Section	Title	Page
I.	Introduction	1
II.	General Model for Dielectric Constants	2
III.	Water: Fit to Dielectric Constant Model, and Model Validation	5
IV.	Dry Sand: Measurements and Fit to Dielectric Constant Model	18
V.	Dry Sand: Model Validation	27
VI.	Dry Sand: Propagation Waveshapes and Data Compilation	33
VII.	Concrete: Measurements	38
VIII.	Concrete: Data Processing and Fit to Dielectric Constant Model	41
IX.	Concrete: Model Validation	52
X.	Concrete: Propagation Waveshapes and Data Compilation	58
XI.	Moist Sand: Measurements	63
XII.	Moist Sand: Data Processing and Fit to Dielectric Constant Model	67
XIII.	Moist Sand: Propagation Waveshapes and Data Compilation	81
XIV.	Dry Sand and Concrete: Model Refinements to Include Conductivity	89
XV.	Free-Field Measurements of Dielectric Constants	94
XVI.	Conclusion	104
Appendix A	Correlation Between Frequency Domain and Time Domain Figures of Merit for UWB Antennas	105
Appendix B	The Lens Effect of a Dielectric Slab	108
	References	111

I. Introduction

This note is a continuation of [1], in which we described a procedure for measuring the dielectric properties of materials using coaxial test fixture. In that work, we also measured the dielectric properties of water, as a calibration standard. The reader is referred to [1] for a description of the apparatus and for the details of the measurement procedures.

In this note we extend the work of [1] in a number of ways. First, we develop a method of fitting a model to measured dielectric constant data, in order to describe it compactly. This model can be either a Debye or Lorentz model, and it may or may not include a dc conductivity term. A Debye model is calculated for the previously measured data on distilled water. This model can serve as a compact description of the dielectric properties of the measured materials over the measured range of frequencies.

Next, we measure the dielectric properties of dry sand, moist sand (1.58% and 3.23% water by weight), and concrete. We fit models to each of these materials, and we verify the models by demonstrating their ability to predict waveshapes in cases different than those that were used to generate the model.

Finally, we predict how a simple Gaussian impulse with a variety of pulsewidths would propagate through these materials, out to a variety of distances. We also compile data on peak magnitude, Full Width Half Max (FWHM), and energy of the transmitted pulses, as an aid to system design.

Let us begin now by deriving a technique for modeling a dielectric medium in a general fashion, which includes conductivity.

II. General Model for Dielectric Constants

In [1], we introduced a Debye Model for distilled water, and we showed that our data followed reasonably well the Debye model described in [2]. However, there is some concern that for some materials a simple Debye model cannot adequately describe a medium that has a low-frequency conductivity. We will see later that this is an important capability to have, so we provide here an extension to the Debye model that includes conductivity.

First, as a review, the Debye model is of the form

$$\epsilon_r(\omega) = \epsilon_\infty + \frac{\epsilon_s - \epsilon_\infty}{1 + j\omega t_o} \quad (2.1)$$

where ϵ_∞ is the relative dielectric constant at high frequencies, ϵ_s is the relative dielectric constant at low frequencies, and t_o is the relaxation time. For water, one set of parameters that has previously been used [2] is $\epsilon_\infty = 1.8$, $\epsilon_s = 81$, and $t_o = 9.4$ ps.

In order to develop an extension to the Debye model, it is helpful to identify an equivalent circuit model for the Debye model of materials. We proceed in a heuristic manner, without rigorous proof. To do so, we express Maxwell's curl equation for H as

$$\nabla \times H = j\omega \epsilon(\omega) E(\omega) + \sigma E(\omega) = J_{tot}(\omega) \quad (2.2)$$

where for unit area the total current, J_{tot} , can be expressed as a sum of the conduction current, J_c , and the displacement current, J_d . Thus, we have

$$\begin{aligned} J_{tot}(\omega) &= J_d(\omega) + J_c(\omega) \\ J_d(\omega) &= j\omega \epsilon(\omega) E(\omega) \\ J_c(\omega) &= \sigma E(\omega) \end{aligned} \quad (2.3)$$

With the Debye model, $J_c = 0$, and using (2.1), the displacement current is

$$\begin{aligned} J_{tot}(\omega) &= J_d(\omega) = j\omega \epsilon(\omega) E(\omega) \\ &= j\omega \epsilon_o \left[\epsilon_\infty + \frac{\epsilon_s - \epsilon_\infty}{1 + j\omega t_o} \right] E(\omega) \end{aligned} \quad (2.4)$$

Consider now the circuit model shown in Figure 2.1. The current that flows into the port on the left is

$$I(\omega) = j\omega \left[C_\infty + \frac{C_1}{1 + j\omega R_1 C_1} \right] V(\omega) \quad (2.5)$$

By comparing the above two equations, we can identify a direct correlation between the Debye model and the circuit model, as shown in Table 2.1.

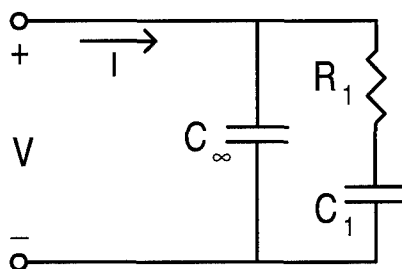


Figure 2.1. Circuit model of the Debye Model.

Table 2.1. Correspondence of the Debye Model to the Circuit Model.

Debye Model	Circuit Model
J_{tot}	I
E	V
$\epsilon_{\infty} \epsilon_0$	C_{∞}
$(\epsilon_s - \epsilon_{\infty}) \epsilon_0$	C_1
t_0	$R_1 C_1$
σ	$1/R_{\infty}$

It now becomes clear how to extend the Debye model to include a conductivity. If we include the conducting current, J_c in equation 2.4, we now have

$$\begin{aligned}
 J_{tot}(\omega) &= J_c(\omega) + J_d(\omega) = \sigma E(\omega) + j\omega\epsilon_r(\omega)E(\omega) \\
 &= j\omega\epsilon_0 \left[\frac{\sigma}{j\omega\epsilon_0} + \epsilon_{\infty} + \frac{\epsilon_s - \epsilon_{\infty}}{1 + j\omega t_0} \right] E(\omega)
 \end{aligned} \tag{2.6}$$

This corresponds to the equivalent circuit of Figure 2.2, which is described by

$$I(\omega) = \left[\frac{1}{R_{\infty}} + j\omega C_{\infty} + \frac{j\omega C_1}{1 + j\omega R_1 C_1} \right] V(\omega) \tag{2.7}$$

Thus, we can add to our correspondence list in Table 2.1 that σ corresponds to $1/R_{\infty}$.

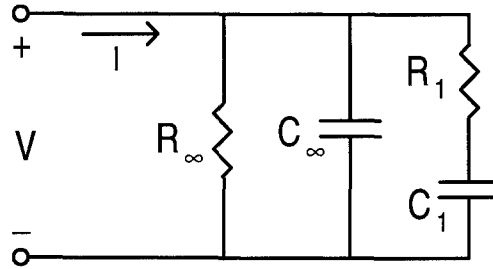


Figure 2.2. Circuit model of the Debye Model, with conductivity included.

The above model is of great interest, because it provides a method of extracting a general relative dielectric constant, ϵ_r , which includes the conductivity, σ . Thus, instead of attempting to extract the three Debye parameters from our data, we extract four, including the conductivity. The new model for the dielectric constant is

$$\boxed{\epsilon_r = \frac{\sigma}{j\omega\epsilon_0} + \epsilon_\infty + \frac{\epsilon_s - \epsilon_\infty}{1 + j\omega t_0}} \quad (2.8)$$

The extra model parameter, σ , adds little complexity to the Least Mean Square (LMS) fit to the data. In the next section, we fit a three-parameter model to the distilled water data, and in later sections we fit a four-parameter model to the data for other materials.

The circuit model we have used is directly analogous to one used in [3]. In that paper, the authors showed how to use a large number of poles, or RC pairs, in the equivalent circuit. One can use additional poles in a model if experimental data is found which cannot be fitted with a single pole.

III. Water: Fit to Dielectric Constant Model, and Model Validation

We use here a Least Mean Squares (LMS) method to fit a Debye model to the dielectric constant of distilled water, as measured previously in [1]. The parameters we found are shown in Table 3.1, and they are compared to the model published by Kunz and Luebbers [2] (the K&L model). The model was fit to the measured dielectric constant data between 0.5 and 3.0 GHz. There is generally a good correlation between the three models, although there is some difference in ϵ_∞ .

To implement the LMS fit, we used a routine in MatLab called "fmins." The technique requires an initial guess, and follows the guess to a local minimum. A bit of trial and error is necessary in order to obtain the best fit, because the routine can only return a local minimum, not a global minimum. The optimum is chosen to minimize the squared magnitude of the difference between the model and the measured data.

Plots of the measured dielectric constant (from [1]), the K&L Model, and the calculated model fit are all shown in Figure 3.1. Furthermore, the attenuations for the three cases are shown in Figure 3.2. The calculated Debye model is a slightly better fit to the experimental data than the K&L Debye model, and this is probably to be expected. Note that ϵ_∞ has little effect on the dielectric constant in the frequency range of interest.

Table 3.1. Comparison of Measured Debye Parameters to the K&L Model[3].

Parameter	Calculated Debye Fit	K&L Debye Model[3]
ϵ_s	81.8358	81
ϵ_∞	23.4606	1.8
t_0	9.4 ps	11.5 ps

Next, we verify the measured Debye model by using it to predict the transmitted voltage for the penetration of water through various lengths of water columns, with various pulse shapes. In each case, the predictions used the measured transmitted waveform through an air-filled line as the incident pulse. This was then modified to include the Fresnel losses at both interfaces and the propagation terms through the water dielectric. It was not necessary to account for multiple reflections, because they were time-gated out of the experimental data. The pulse shapes included a broad impulse, a doublet, a step, and a narrow impulse. Tables 3.2.-3.4 summarize the raw data that was taken for the three waveforms. The waveform parameters recorded in these tables were measured using the built-in functions of the Tektronix 11801 scope, with the IEEE options selected. The measurement setup was the same as that used in [1], with additional impulse forming networks and risetime limiters to shape the pulse.

Results for these predictions are shown in Figures 3.3-3.4 for the broad impulse, Figures 3.5-3.6 for the doublet, Figures 3.7-3.8 for the step function, and Figures 3.9-3.10 for the narrow impulse. Overlaid on the raw data are the predictions using both the calculated Debye model and the K&L Debye model. Both models are seen to provide very good agreement to the measured data. Note that the absolute time delay has been removed from the plotted data, but it can be reconstructed from the Scope Delays in the tables.

Because our predictions match so well with the measured data, we have demonstrated the ability to predict the transmitted waveform through a layer of water for a variety of pulse shapes and material thicknesses.

Table 3.2. Propagation Through Water, Broad Impulse.

Water Length (cm)	Scope Delay (ns)	Pulse Width (FWHM ps)	Amplitude (mV)	File #
00.00	83.865	118	265.2	F6102101
4.77	84.915	272	41.6	F6102102
9.54	85.915	378	30.7	F6102103
38.18	93.215	728	15.7	F6102104

Table 3.3. Propagation Through Water, Doublet.

Water Length (cm)	Scope Delay (ns)	File #
00.00	84.115	F6102105
4.77	85.115	F6102106
9.54	85.315	F6102107
38.18	93.265	F6102108

Table 3.4. Propagation Through Water, Step Function.

Water Length (cm)	Scope Delay (ns)	Rise Time (10-90% ps)	Amplitude (0-100% mV)	File #
00.00	83.365	70	406	F6102109
4.77	84.465	271	148	F6102110
9.54	85.515	377	146	F6102111
38.18	92.915	766	146	F6102112

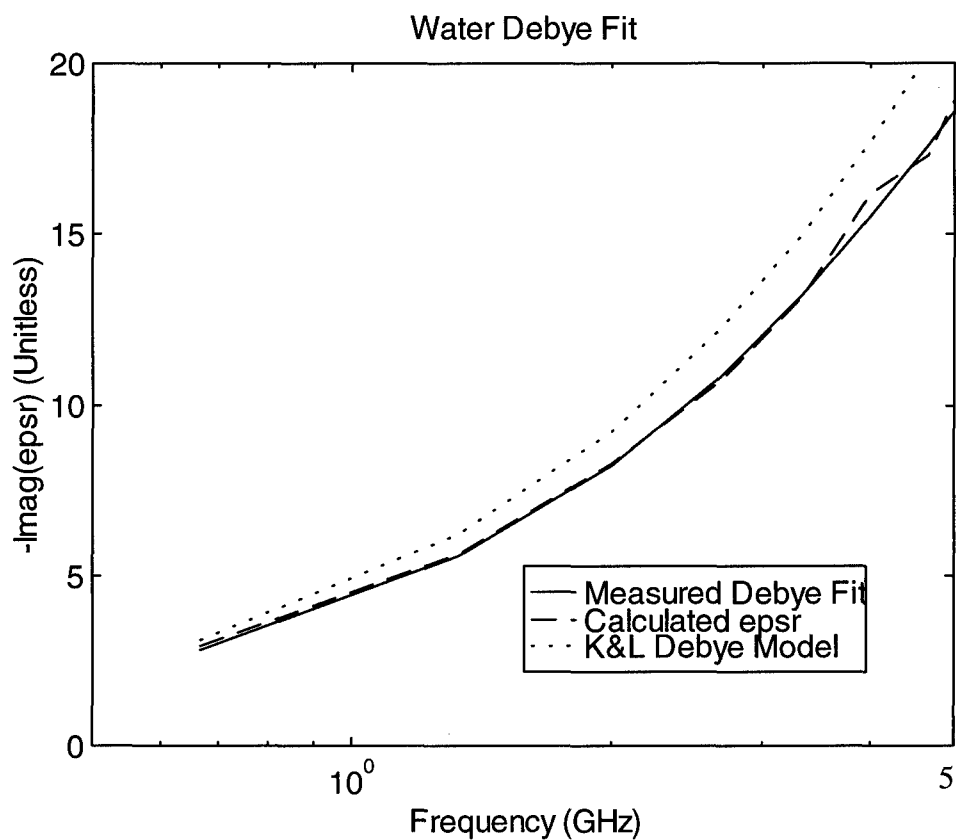
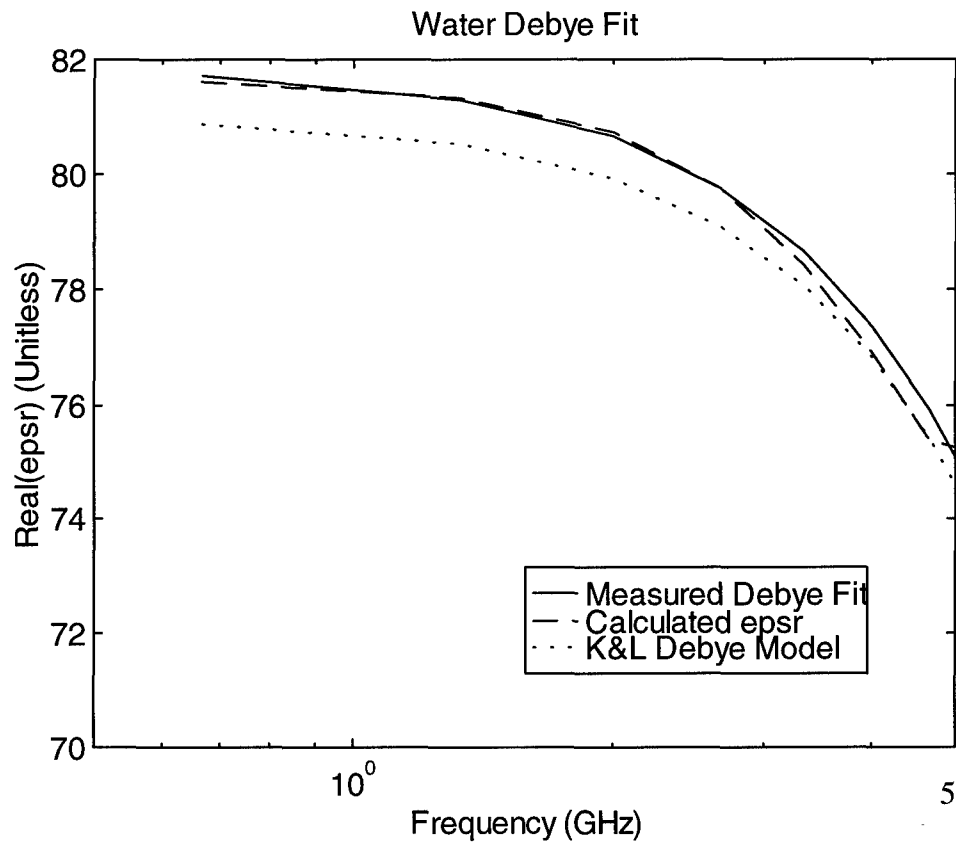


Figure 3.1. Debye fit to the calculated water dielectric constant.

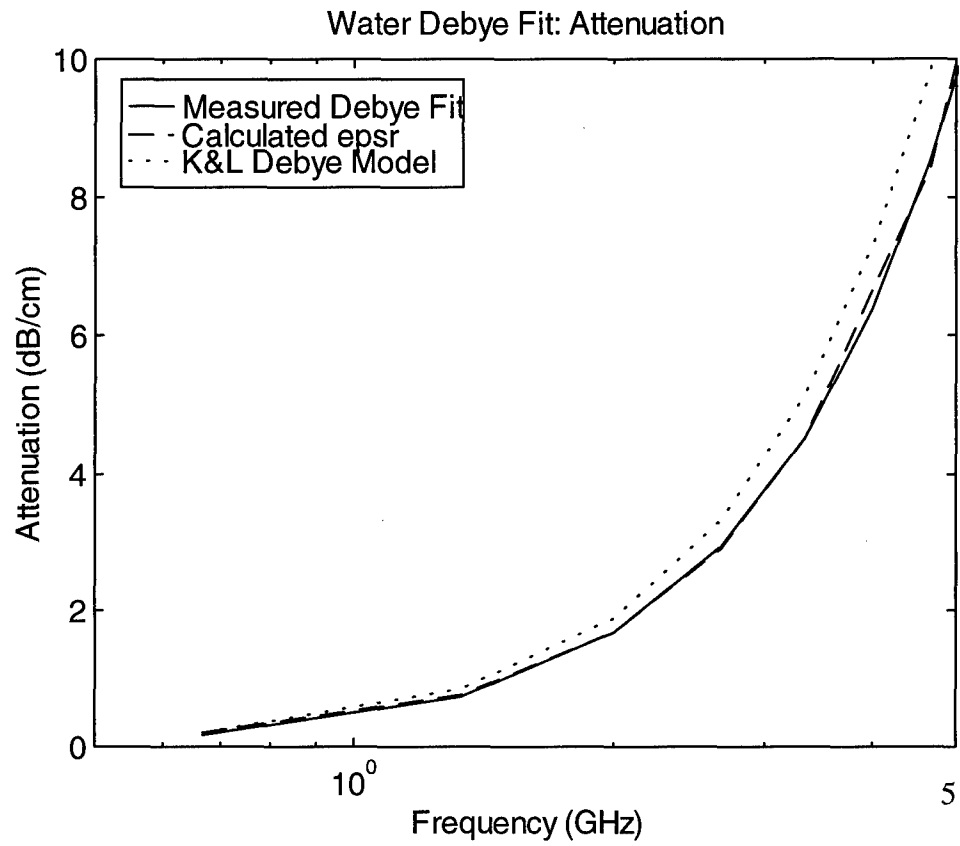


Figure 3.2. Comparison of the attenuation of water using the measured values, the Debye fit to the measurements, and the K&L Debye fit.

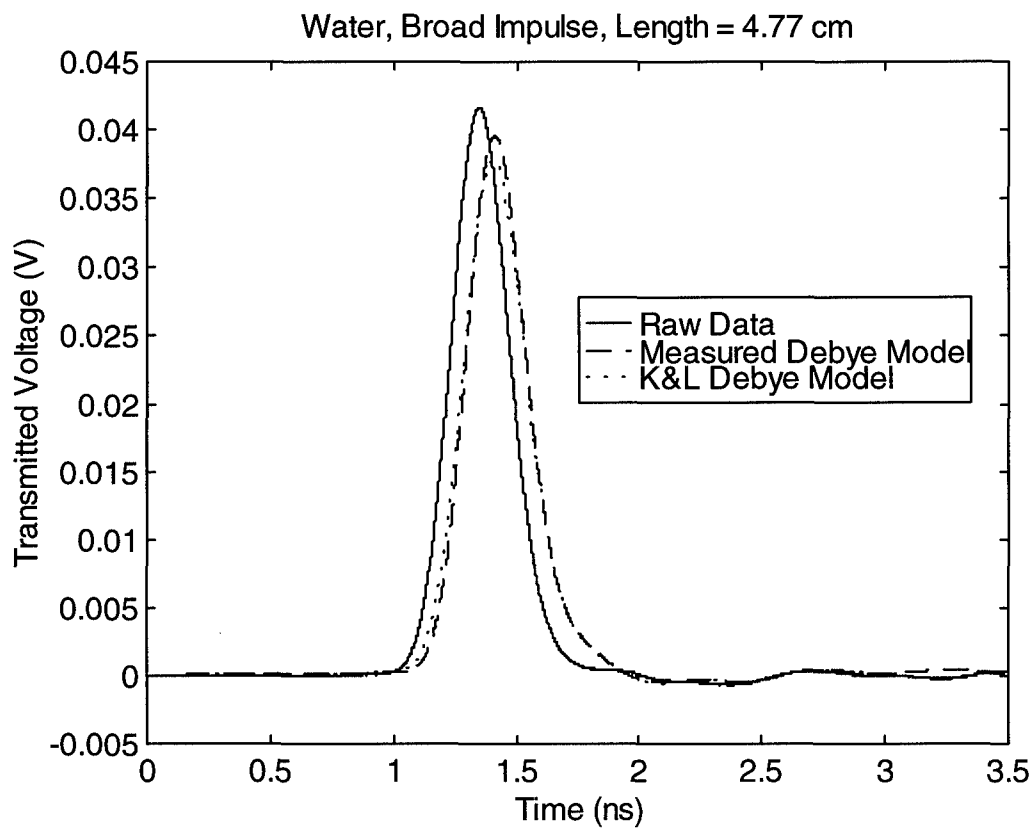
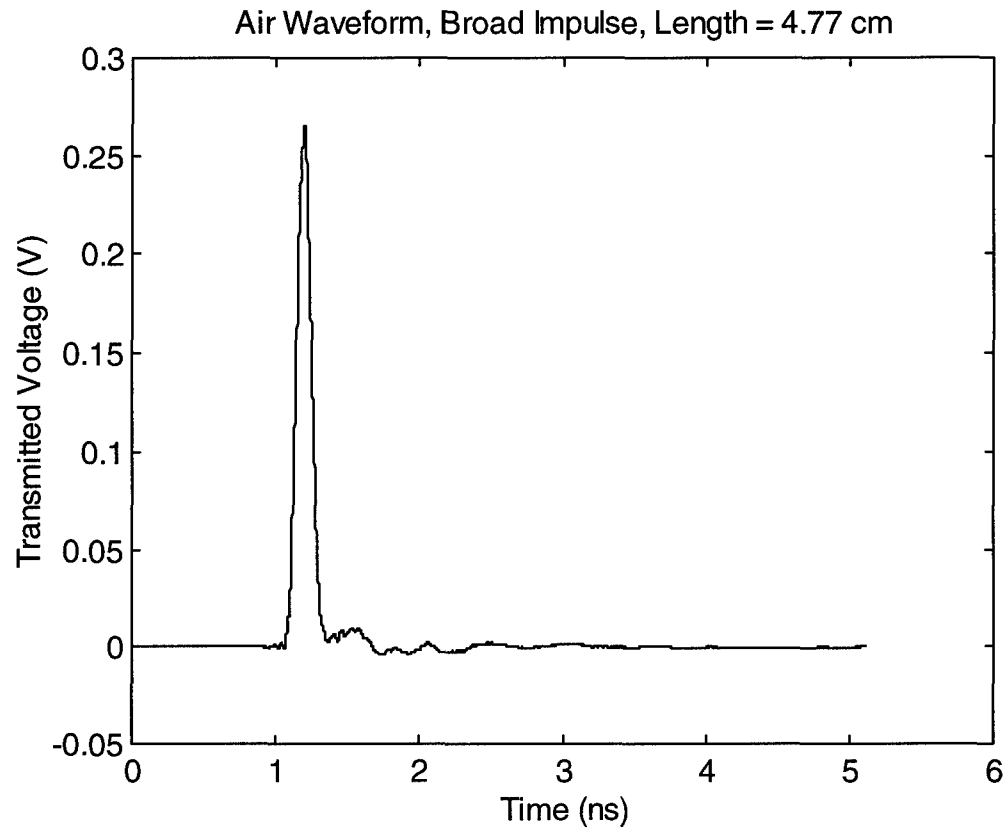


Figure 3.3. Broad impulse air waveform, and transmission through 4.77 cm water.

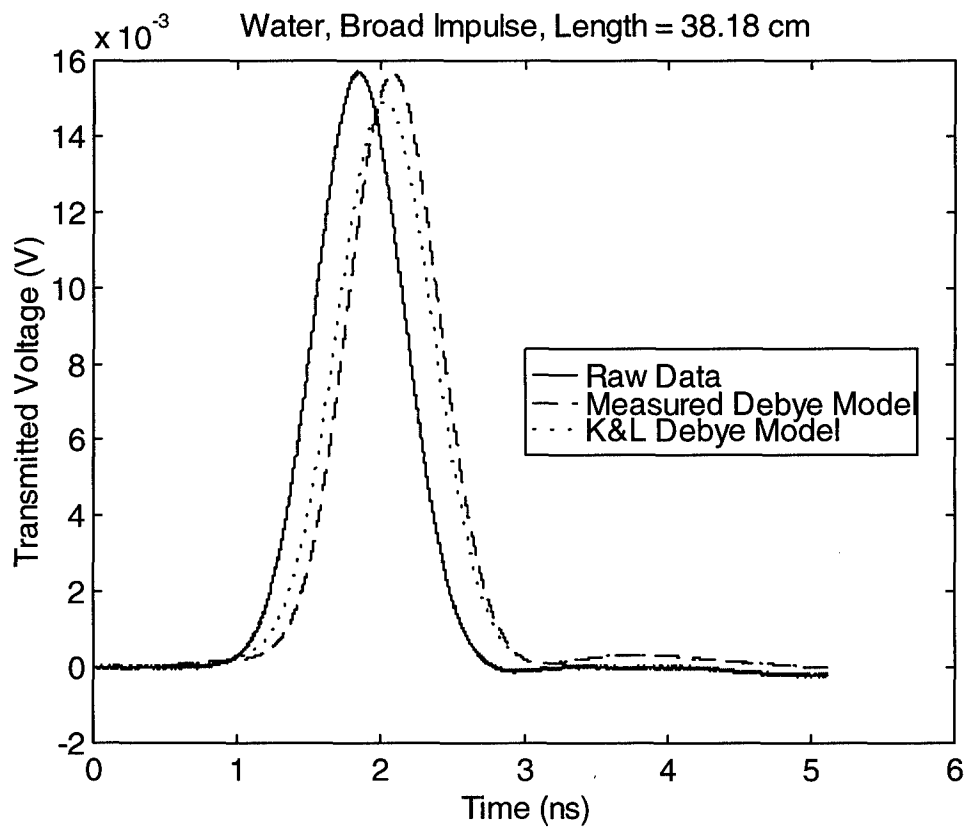
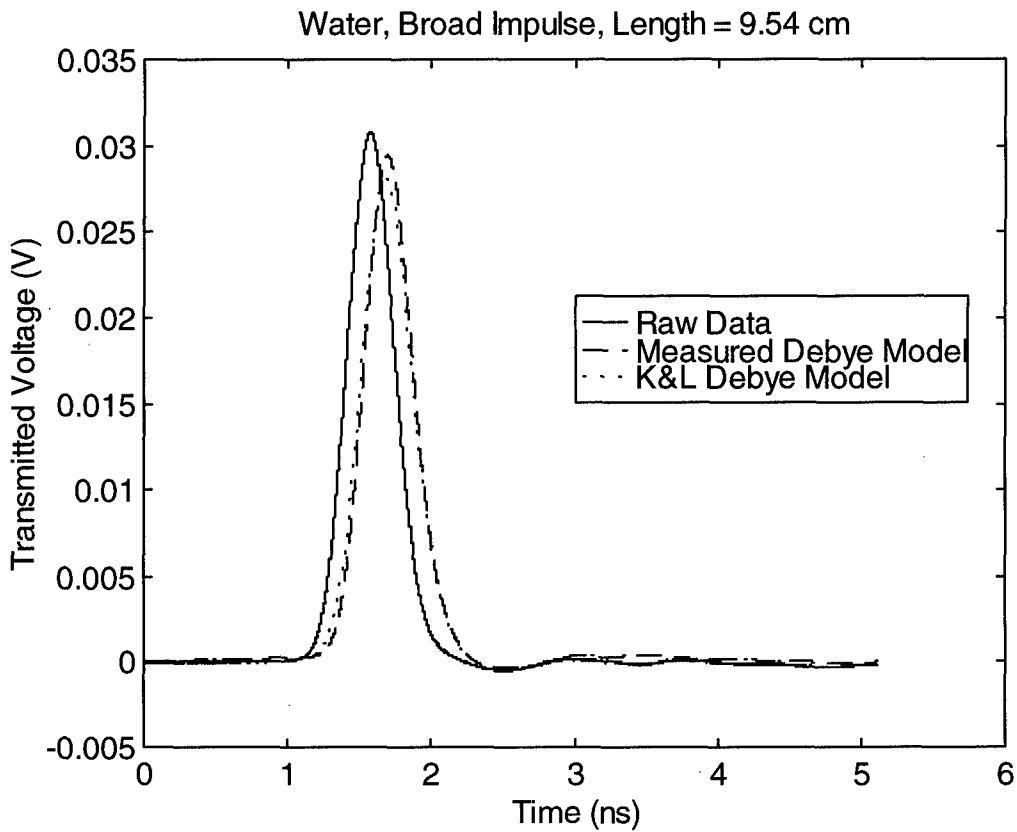


Figure 3.4. Broad impulse transmission through 9.52 cm and 38.18 cm water.

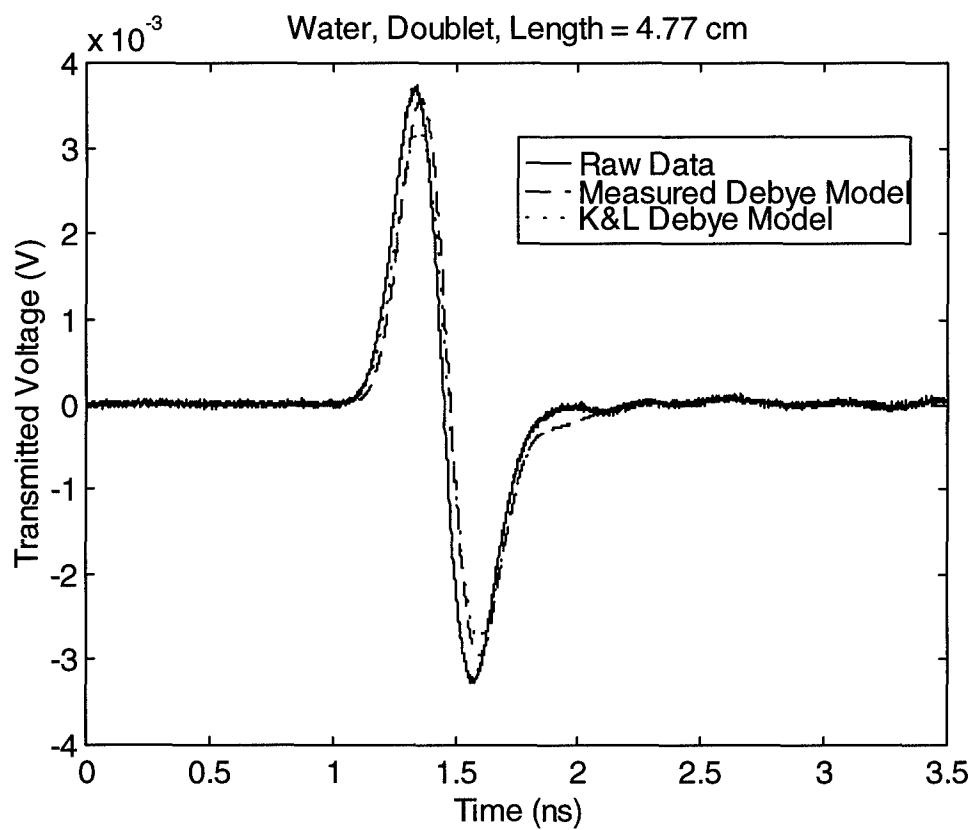
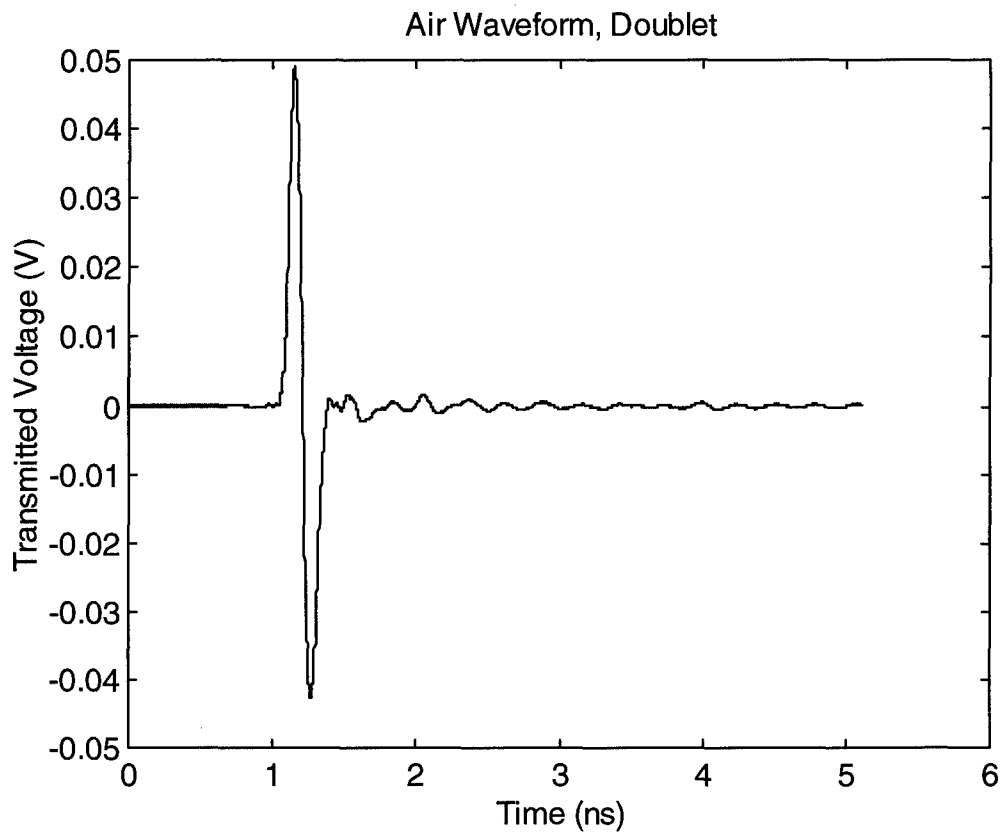


Figure 3.5. Doublet air waveform, and transmission through 4.77 cm water.

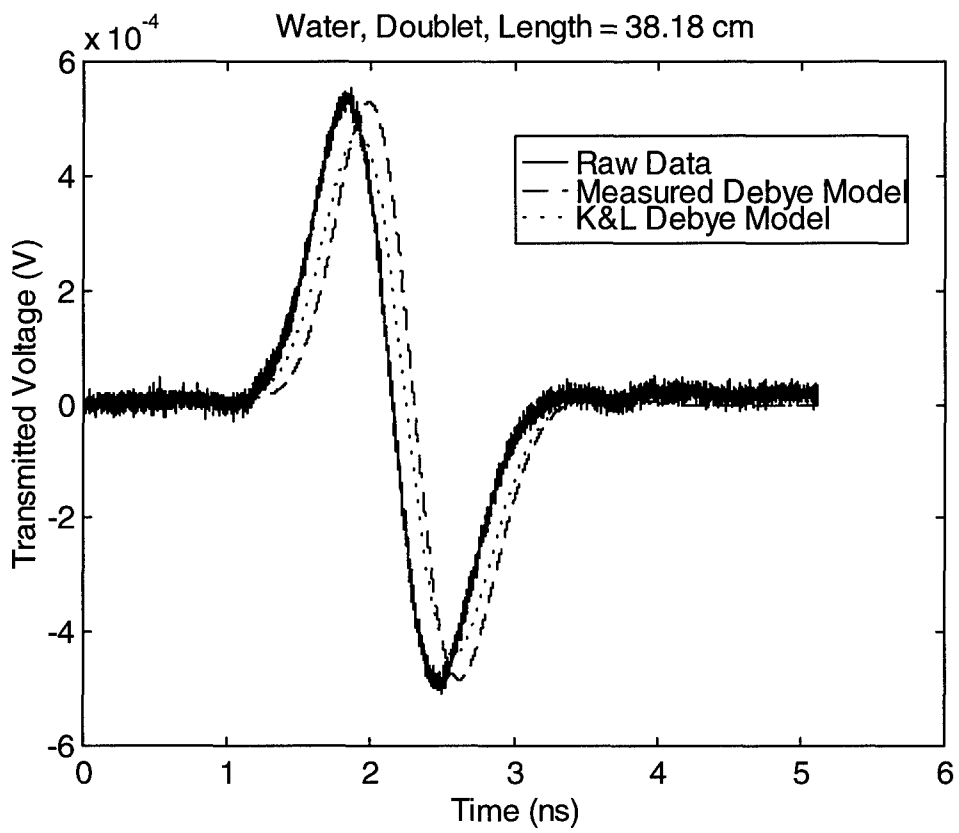
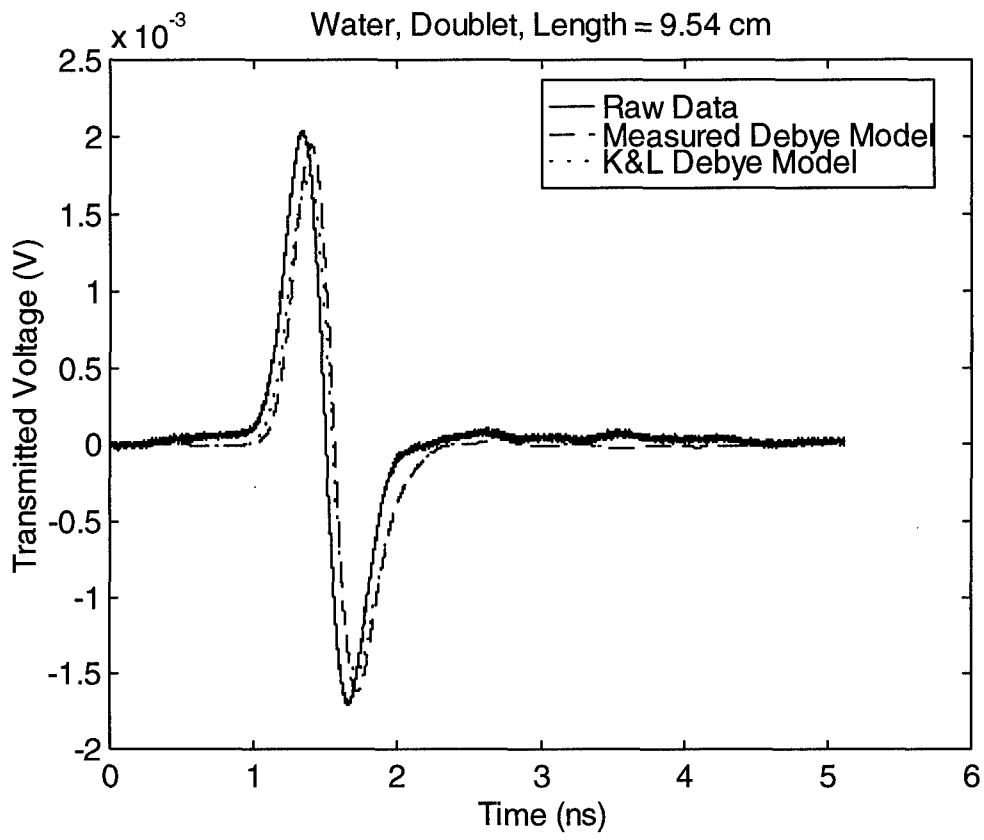


Figure 3.6. Doublet transmission through 9.52 cm and 38.18 cm water.

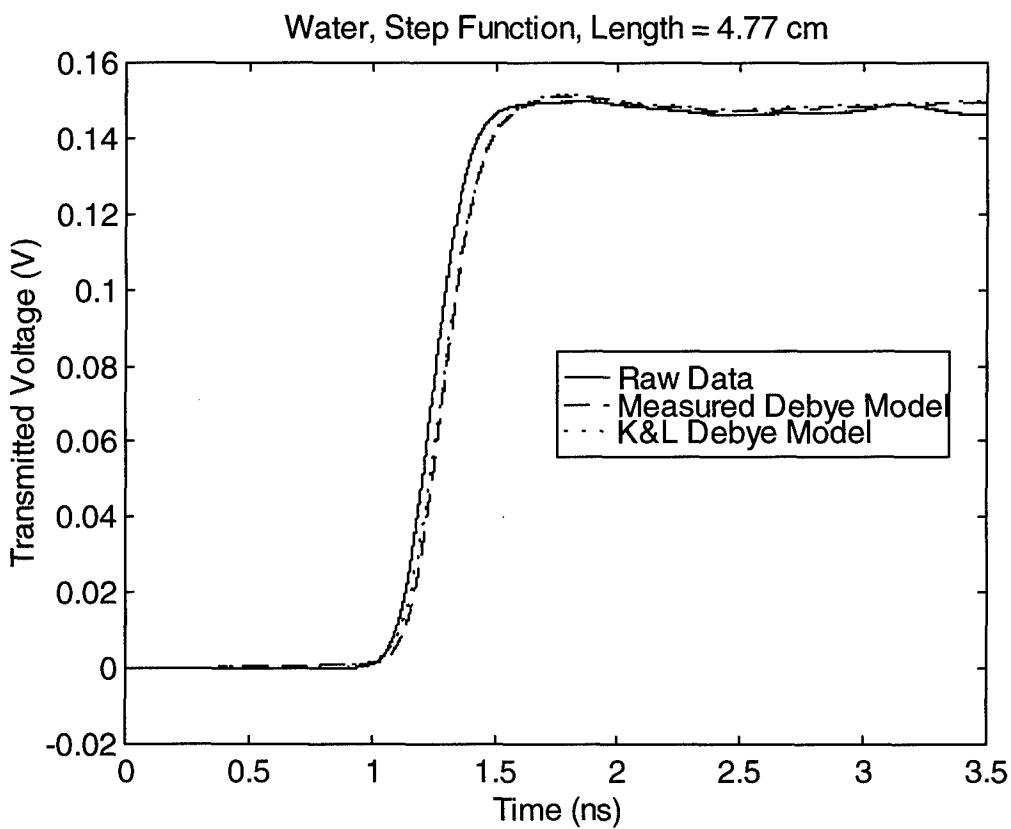
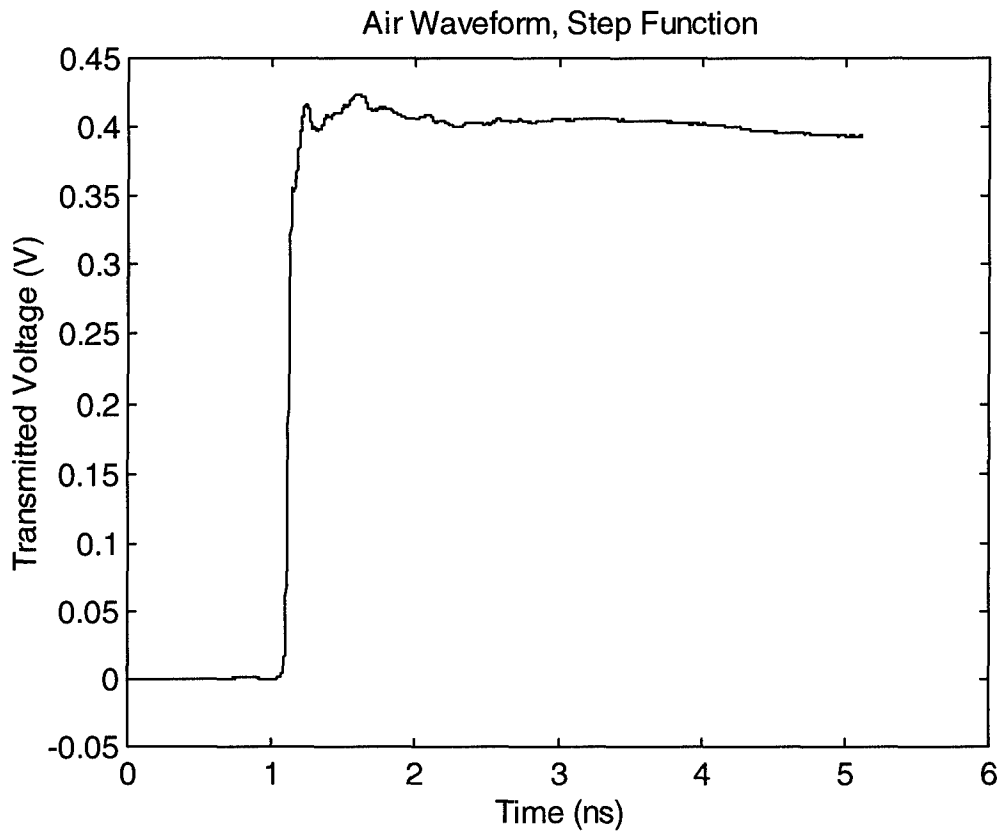


Figure 3.7. Step air waveform, and transmission through 4.77 cm water.

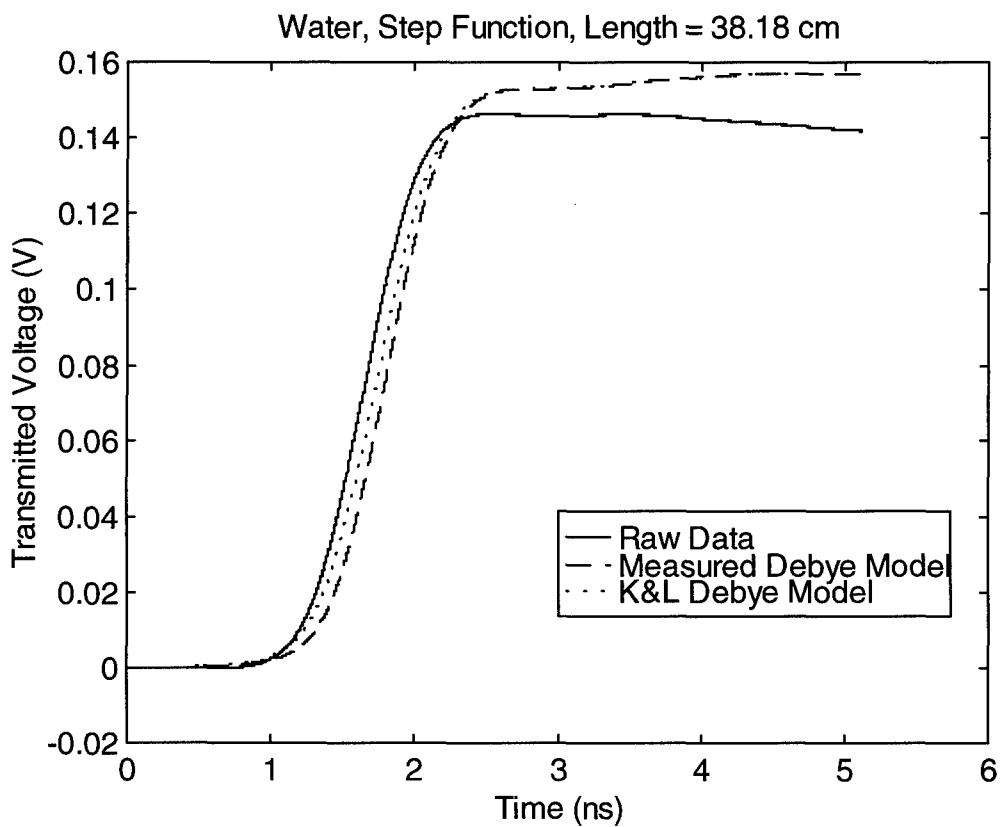
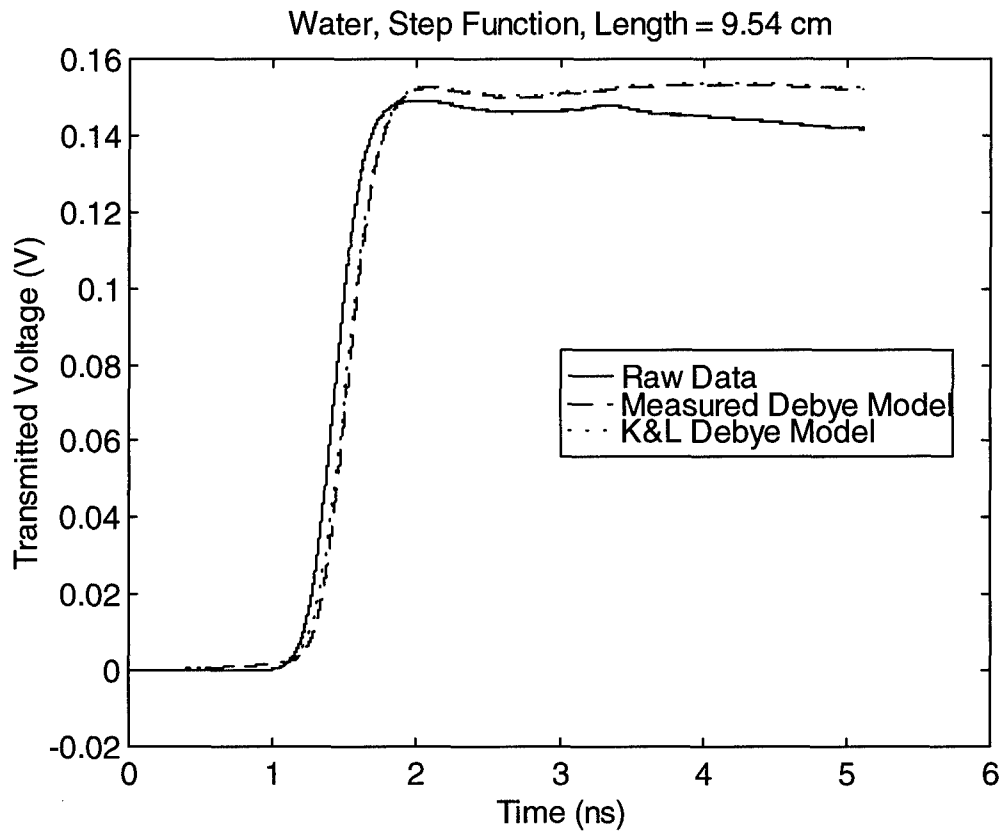


Figure 3.8. Step transmission through 9.52 cm and 38.18 cm water.

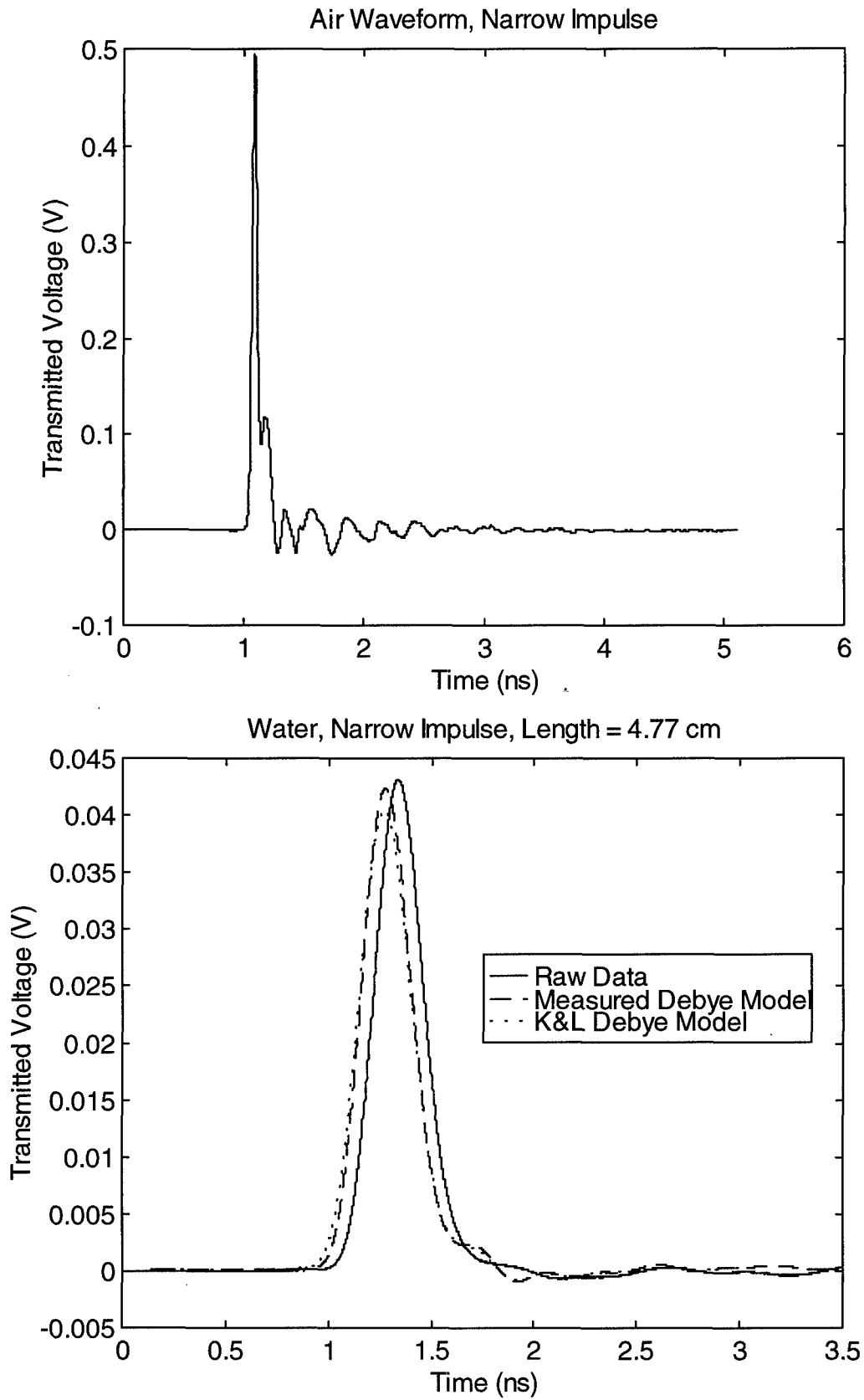


Figure 3.9. Narrow impulse air waveform, and transmission through 4.77 cm water.

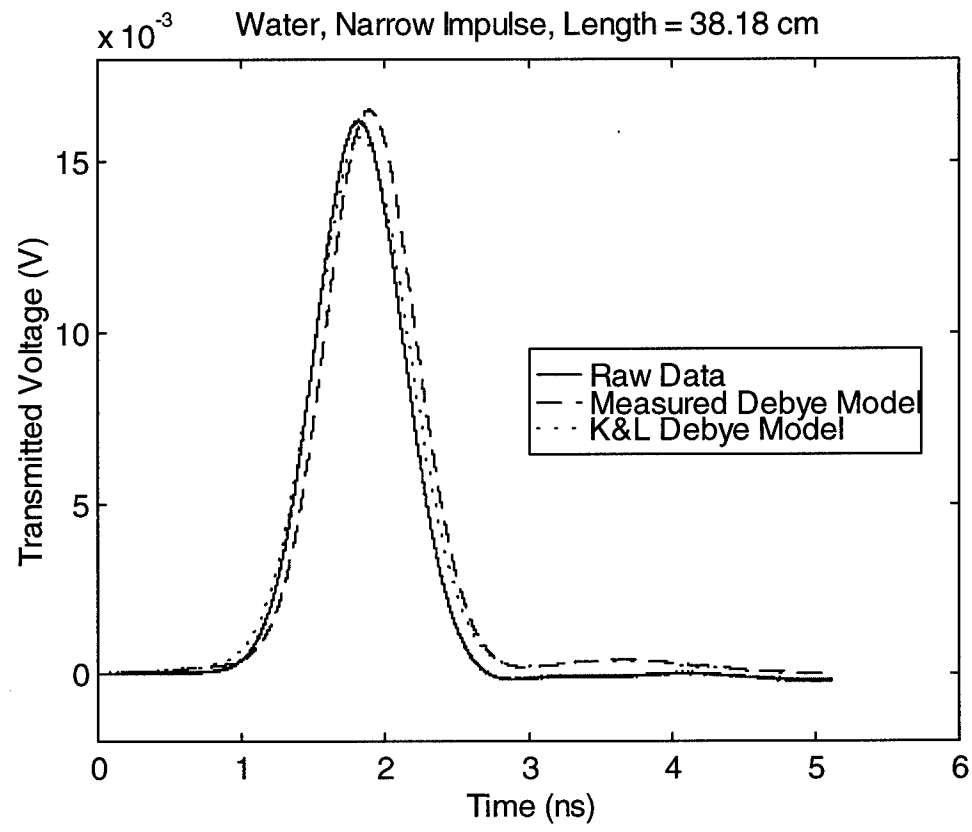
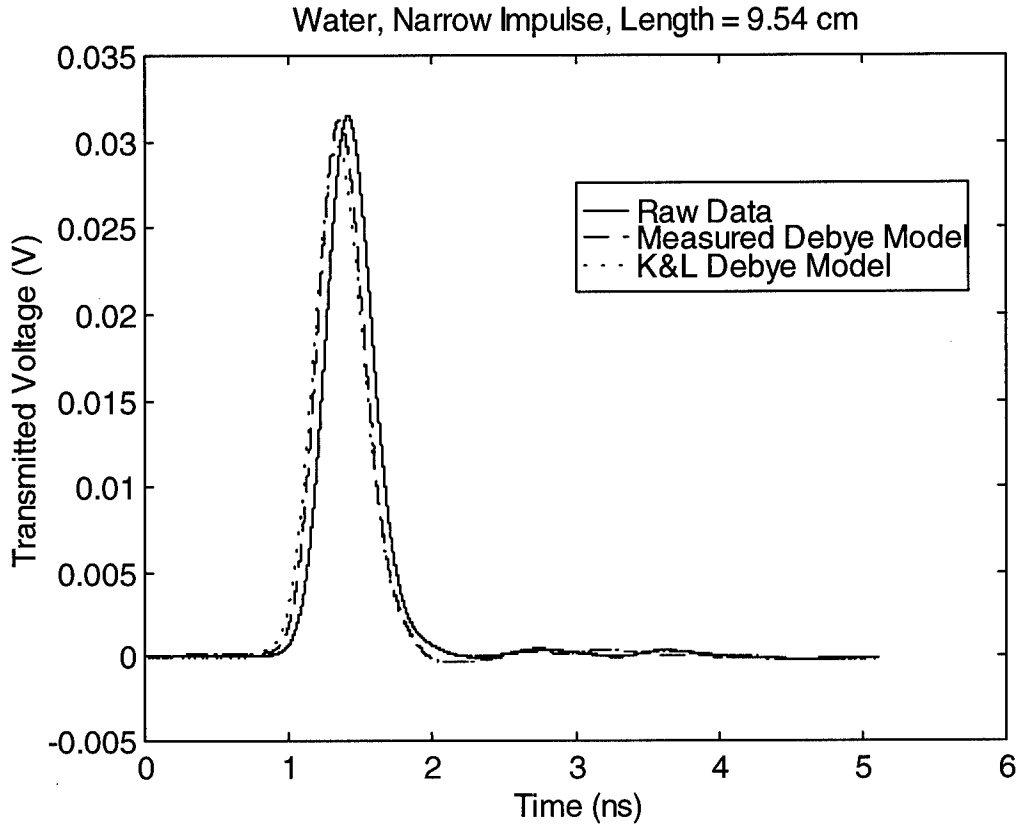


Figure 3.10. Narrow impulse transmission through 9.52 cm and 38.18 cm water.

IV. Dry Sand: Measurements and Fit to Dielectric Constant Model

We provide here a complete set of data for a sample of dry sand. This data format is very similar to that provided earlier in [1]. The measurement technique is the same, and the processing is almost exactly the same, with minor exceptions as noted below.

Our sample of sand was taken from the Eglin AFB Sand Box facility. All the sand was heated on a flat open tray to a temperature of 107°C (225° F) for one hour, in order to dry the sample thoroughly. The loose dry sand was weighed on a digital scale and found to have a density of 1.50 g/cm³. Compressed sand would have a higher density. The sand was introduced into the coaxial test fixture without compaction.

First, we provide all six raw waveforms which were taken with the narrow impulse. These are shown in Figure 4.1. Details relating to the data appear in Table 4.1. Examination of the data shows that dry sand is a good medium for propagating narrow impulses.

The air waveform of the narrow impulse (FWHM = 41.3 ps) through the coaxial test fixture is shown in Figure 4.2. This is simply the waveform after it has passed through the coax test fixture when no material is present. The waveform is shown in both the time and frequency domains, in order to show the effective bandwidth of the measurement system. The frequency domain plot shows an effective bandwidth in the system of around 20 GHz.

Next, we show the transmitted voltage through 35.97 cm and 59.65 cm of dry sand (Figure 4.3). This is the raw data upon which the calculation of the dielectric constant is based. The ratio of these two waveforms in the frequency domain represents the impulse response for the difference of the two lengths, or 23.86 cm. The ratio was taken by limiting the smallest value of the denominator to 1% of its peak in the frequency domain, and by applying a 10th-order modified Butterworth filter at 20 GHz. The resulting ratio is shown in Figure 4.4, and the corresponding time domain impulse response and its integral are shown in Figure 4.5.

With the above data, we can now calculate the dielectric constant, using the techniques of [1]. The real and imaginary parts of the dielectric constant are shown in Figure 4.6. The corresponding attenuation is shown in Figure 4.7. A Debye fit was generated for this above dielectric constant data. This data is overlaid onto Figures 4.6 and 4.7. The Debye fit was implemented using a least mean squares fit to the dielectric constant model of Eqn. 2.1, using data between 500 MHz and 15 GHz. A table of our fitted values for these parameters is shown in Table 4.2. The fit is quite good at midband, and differs somewhat from the data at higher frequencies, near where the low-pass filter is applied.

We hypothesize now that the above three Debye parameters will be sufficient to predict the transmitted voltage through other lengths of dry sand, and using other wave shapes. This is demonstrated in the section that follows.

Table 4.1. Experimental Data For Transmission Through Dry Sand In Coax Line With a Narrow Impulse.

Sample Length (cm)	FWHM (ps)	File Number
0.	41.3	F6092401
11.90	48.5	F6092402
23.86	50.6	F6092403
35.97	55.1	F6092404
47.72	60.1	F6092405
59.65	67.6	F6092406

(NOTE: Air Length for all data = 100.00 cm - sample length;
Scope Delay = (83.51 + 0.5) ns for all data.

Table 4.2. Debye Parameters for Dry Sand.

Parameter	Debye Fit for Dry Sand
ϵ_s	2.5220
ϵ_∞	2.4725
t_0	21.5 ps

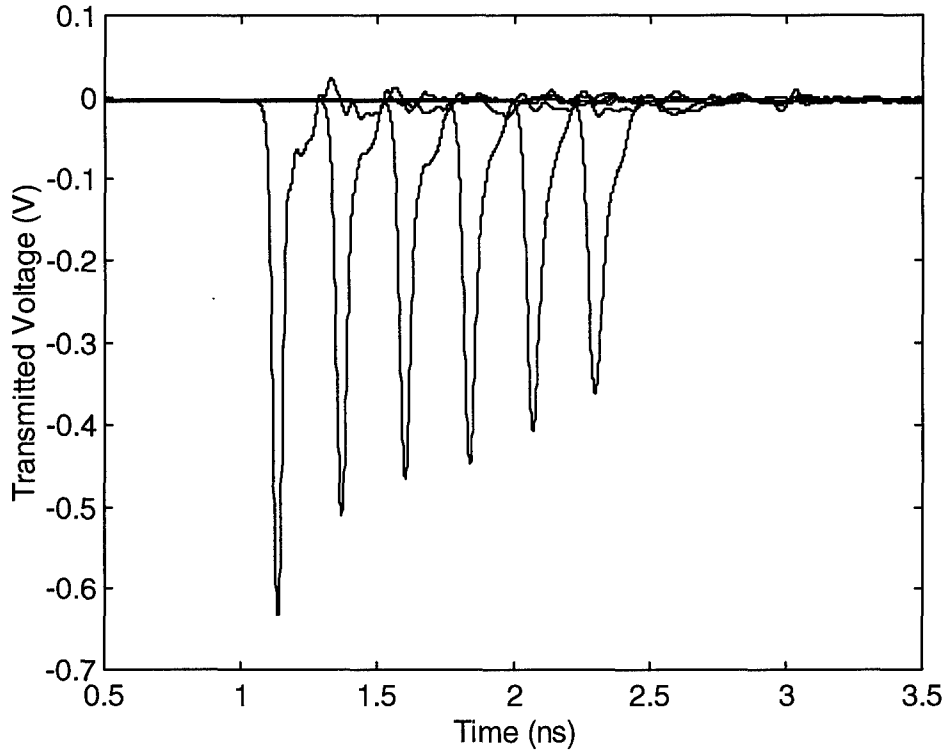


Figure 4.1. Propagation through dry sand, with thicknesses of 0, 11.9, 23.86, 35.79, 47.72, and 59.65 cm.

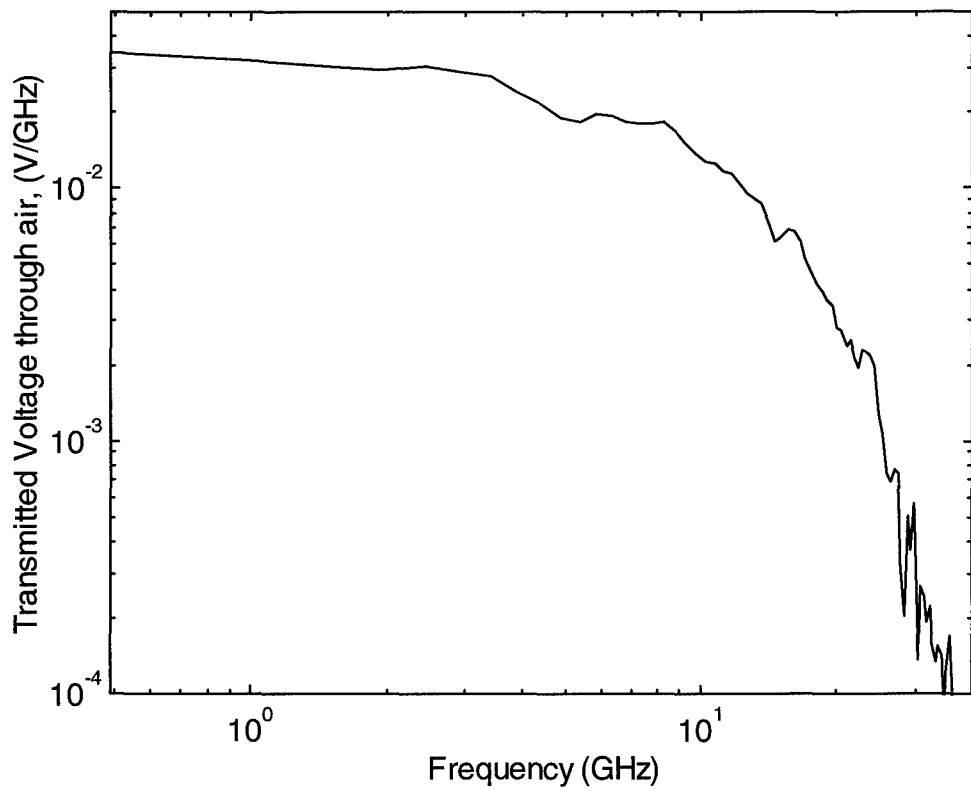
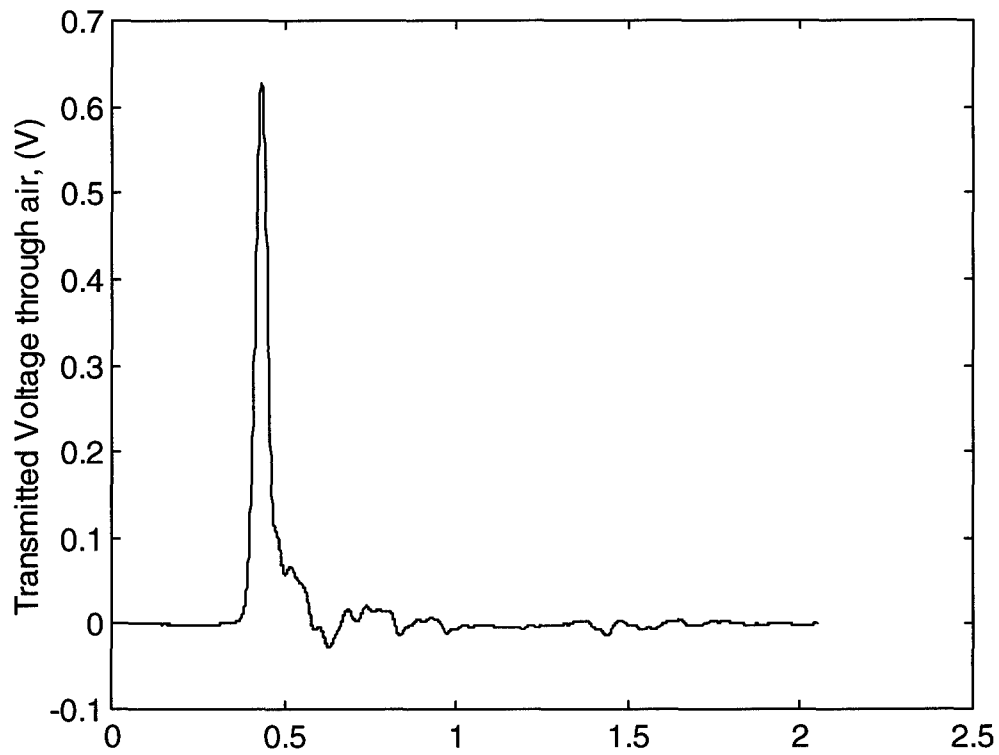


Figure 4.2. Air waveform for the dry sand measurements, time domain (top) and frequency domain (bottom).

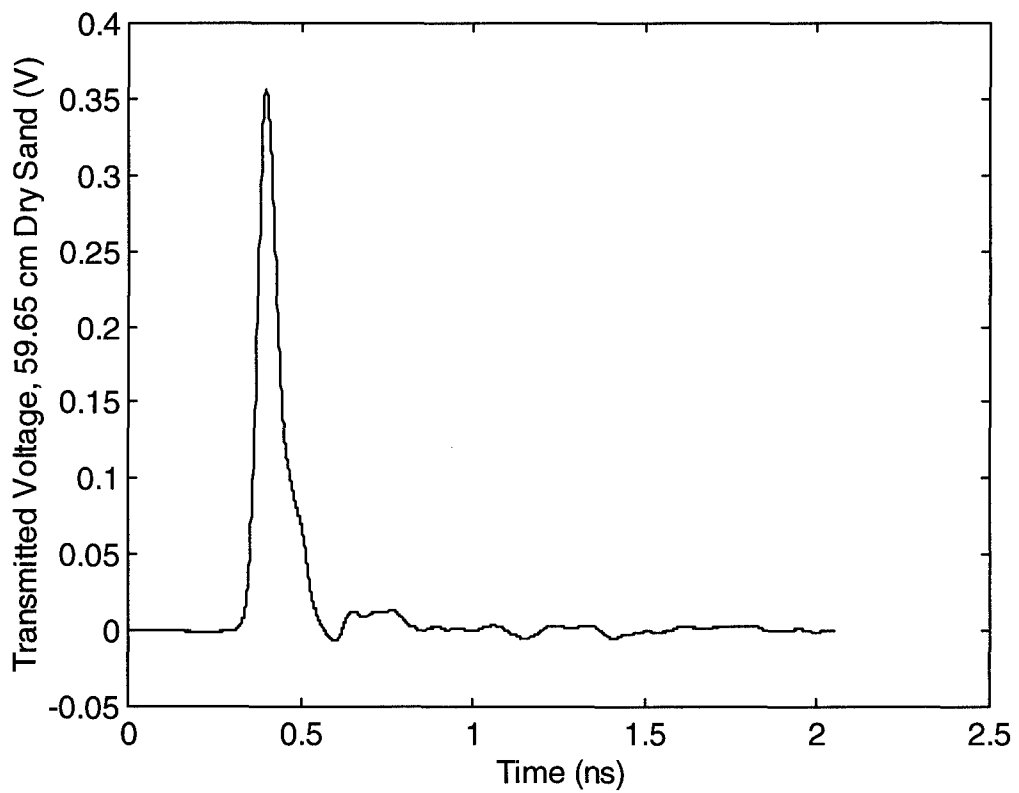
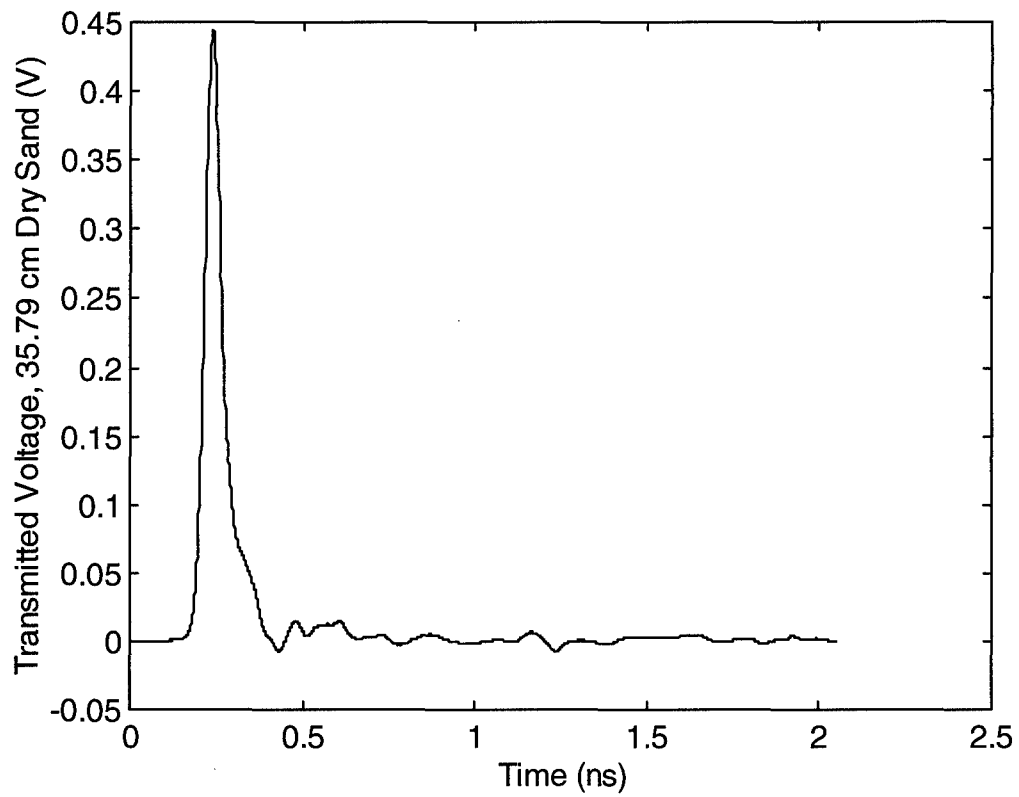


Figure 4.3. Transmitted signals through 35.79 cm and 59.65 cm of dry sand.

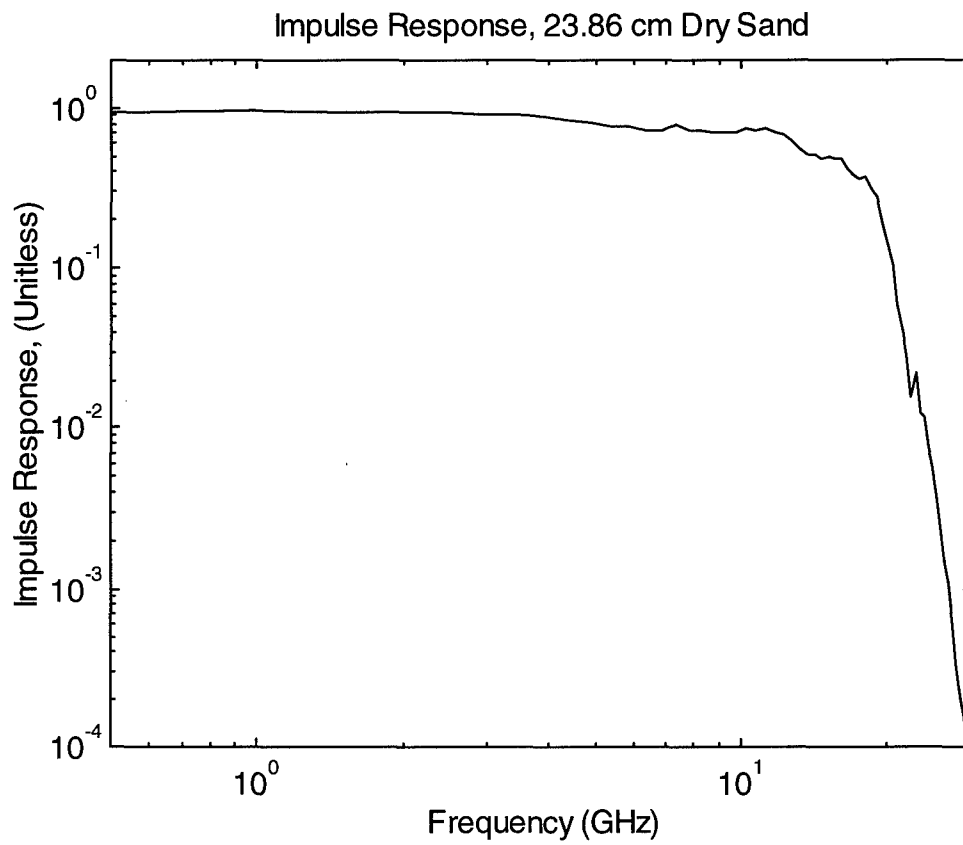


Figure 4.4. The impulse response of 23.86 cm of dry sand.

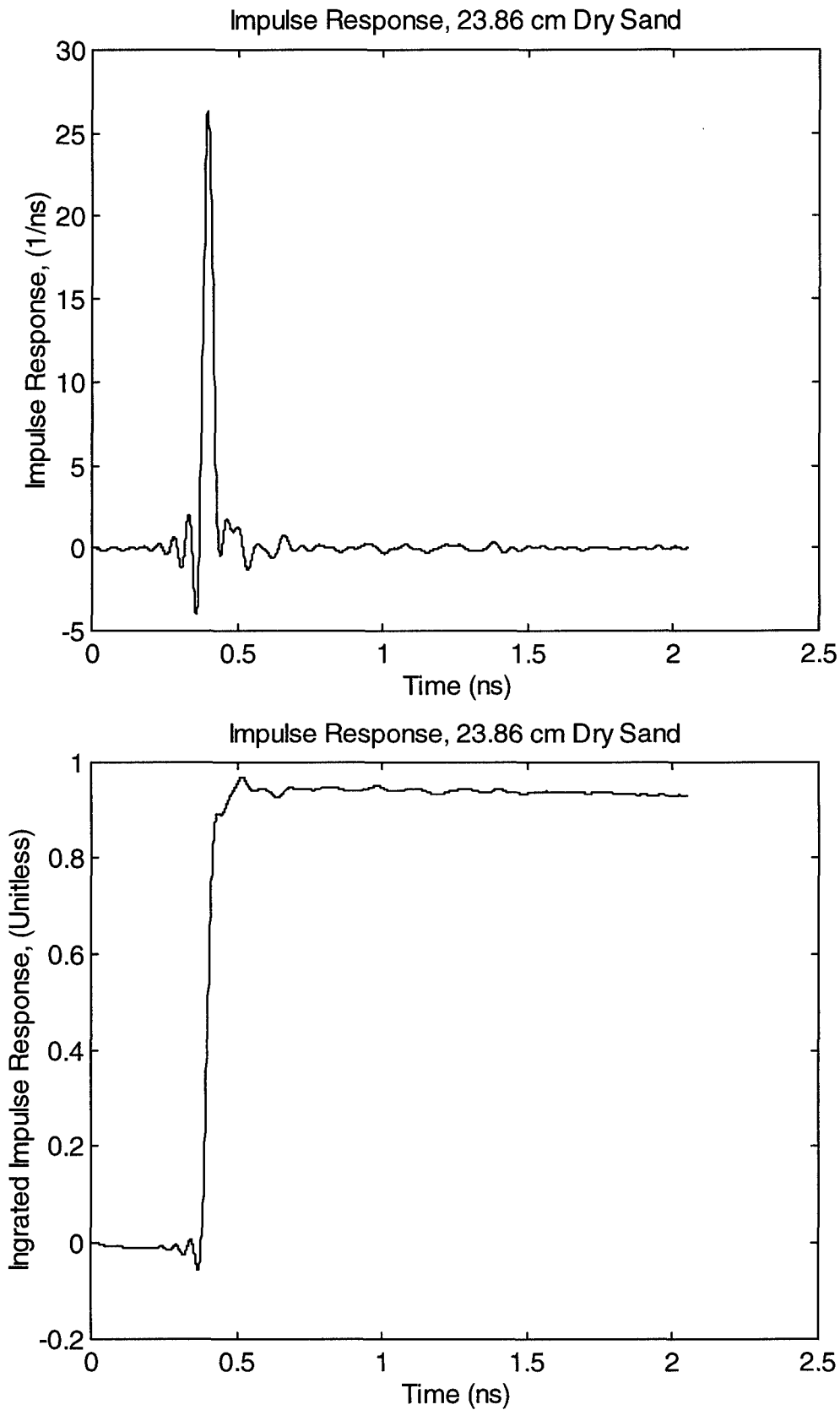


Figure 4.5. The impulse response (top) and its integral (bottom) of 23.86 cm dry sand.

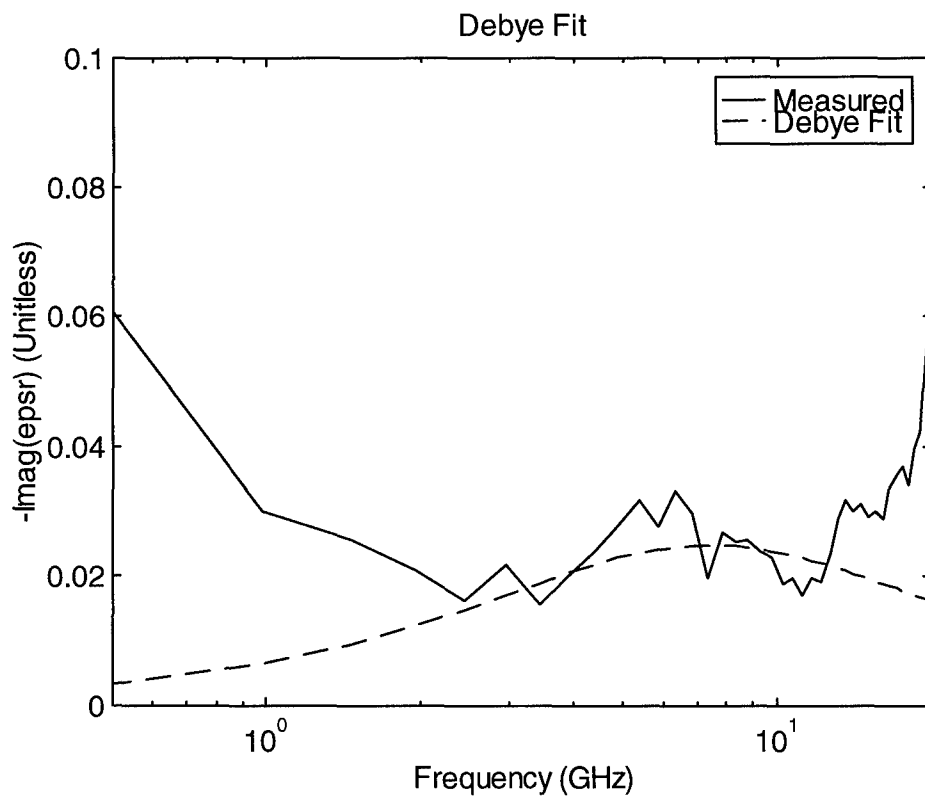
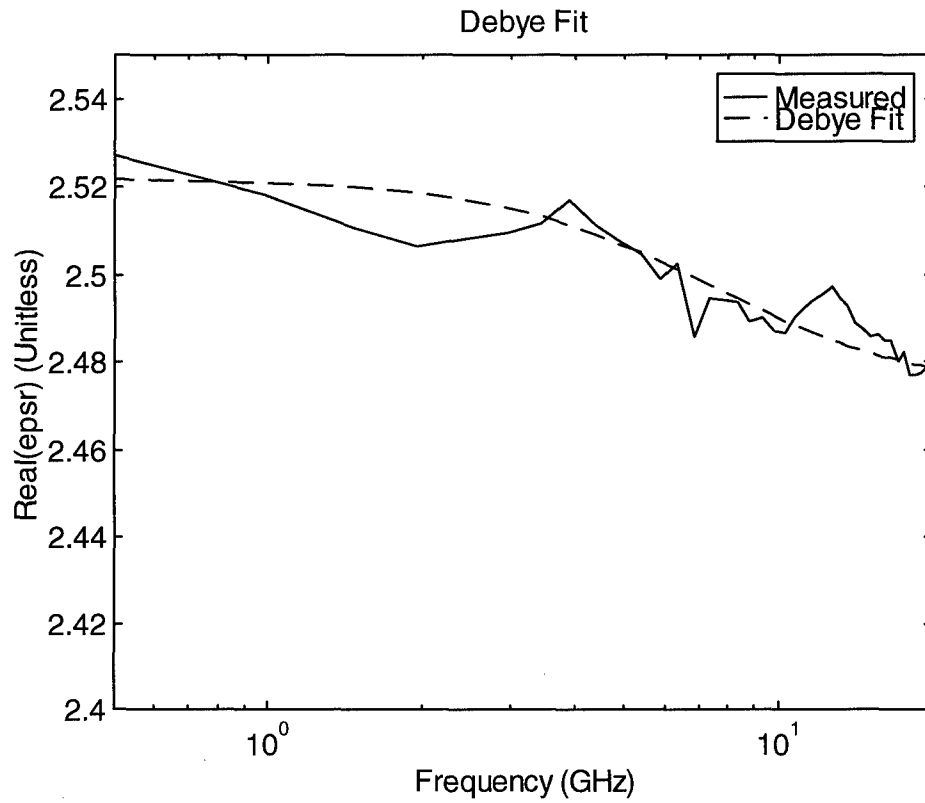


Figure 4.6. Measured dielectric constant of dry sand, and the Debye fit, real and imaginary parts.

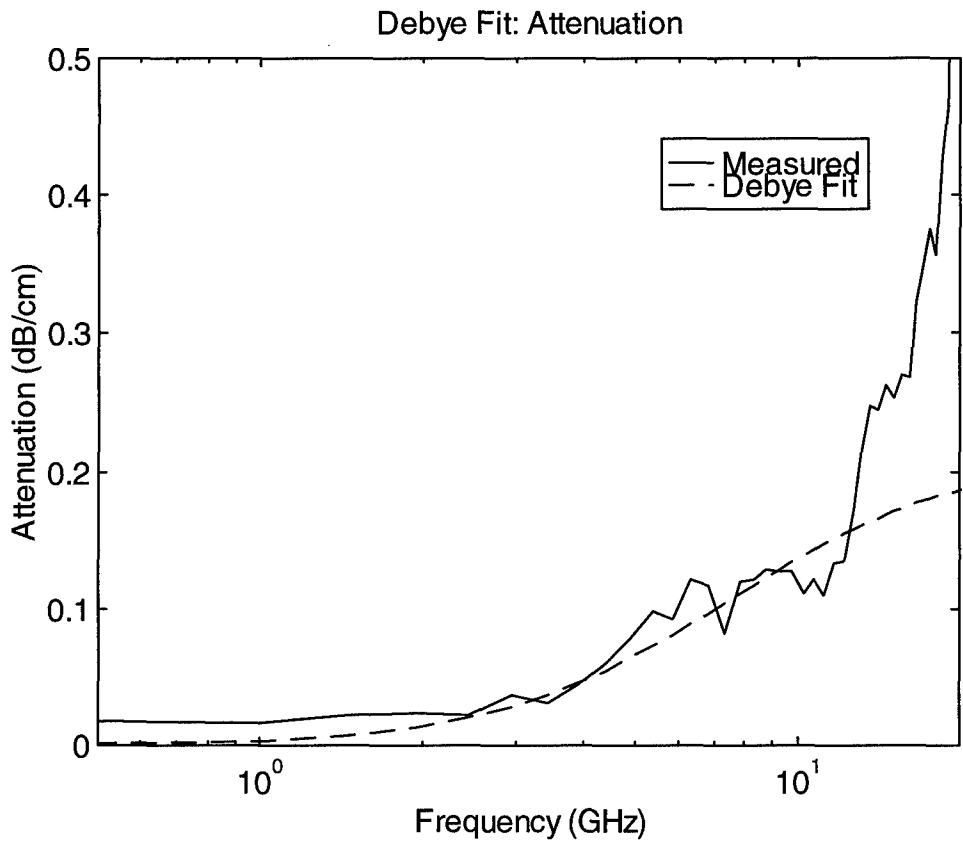


Figure 4.7. Attenuation constant of dry sand, measured and Debye fit.

V. Dry Sand: Model Validation

Now that we have determined the dielectric constant of dry sand, we validate the model by predicting the transmitted voltage for other waveshapes and other sand column lengths. These predictions are then compared to the raw measured time domain waveforms. Various pulse shapes were produced by using waveshaping modules to tailor the output from the PSPL 4015C pulser. Table 5.1 summarizes the raw data on propagation of various pulse shapes through dry sand.

In order to predict the voltage transmitted through the sand, we need only the air waveform and the Debye parameters from the previous section. First, we generate the relative dielectric constant, $\epsilon_r(\omega)$ as a function of frequency from equation (2.1). Next, we calculate the transmission coefficients at the front and back interfaces, as

$$\tau_1(\omega) = \frac{2}{\sqrt{\epsilon_r(\omega) + 1}}, \quad \tau_2(\omega) = \frac{2\sqrt{\epsilon_r(\omega)}}{\sqrt{\epsilon_r(\omega) + 1}} \quad (5.1)$$

Next, we calculate the propagation factor through the sand as

$$T(\omega) = e^{-jk_0(\sqrt{\epsilon_r(\omega)}-1)\ell} \quad (5.2)$$

where k_0 is the free-space propagation constant, and ℓ is the sample length. Note that the above propagation factor is actually the difference between the propagation through the sample and the propagation term through free space. In other words, there is an additional time correction required to compensate for the reduced air path length, which is displaced as material is added to the coax line. We can therefore calculate the transmitted voltage as

$$V_{trans}(\omega) = \tau_1(\omega) \tau_2(\omega) T(\omega) V_{air}(\omega) \quad (5.3)$$

We then convert the transmitted voltage to the time domain, and we have our result. Note that in the above formulation we have ignored multiple reflections, which are time-gated out of our measurements.

Let us first consider the propagation of a broad impulse (122.2 ps FWHM) through the air-filled coax, as shown in Figure 5.1. Note that this is a different waveshape than that used in the previous section to calculate the dielectric constant. The waveshape used here is a broader impulse. We predict the transmitted voltage through 23.86 cm and 59.65 cm of dry sand using our Debye parameters from the last section, the air waveform, and equation (5.3). The results are shown in Figure 5.2, and are overlaid with raw data taken for the same case. We find excellent agreement between our predictions and the measurement.

Finally, we repeat the process for a doublet waveform, with sand columns of the same length as above. The air waveform for the doublet is shown in Figure 5.3, and the predictions

and measurements for the voltages transmitted through the samples are shown in Figure 5.4. Once again, there is excellent agreement between our predictions and the measurements.

Table 5.1. EXPERIMENTAL DATA FOR TRANSMISSION THROUGH DRY SAND IN COAX LINE USING VARIOUS PULSE SHAPES.

(NOTE: Air Length for all data = 100.00 cm - sample length;
Scope Delay = 82.82 ns for all data.)

DOUBLET			
Sample Length (cm)	Amplitude Pk-Pk(mV)	File #	
00.00	101	F6110801	
23.86	89	F6110802	
59.65	82	F6110803	

IMPULSE			
Sample Length (cm)	Pulsewidth (FWHM ps)	Amplitude (mV)	File #
00.00	122.2	291	F6110804
23.86	125.9	266	F6110805
59.65	125.8	256	F6110806

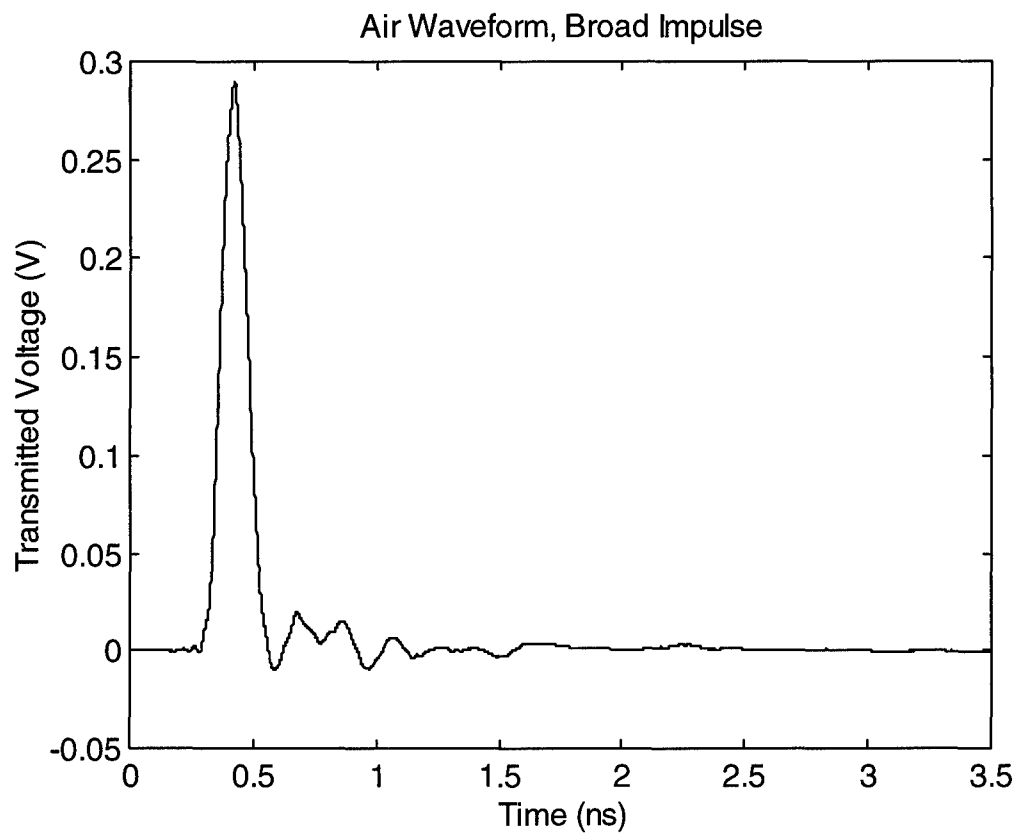


Figure 5.1. Air waveform for the broad impulse.

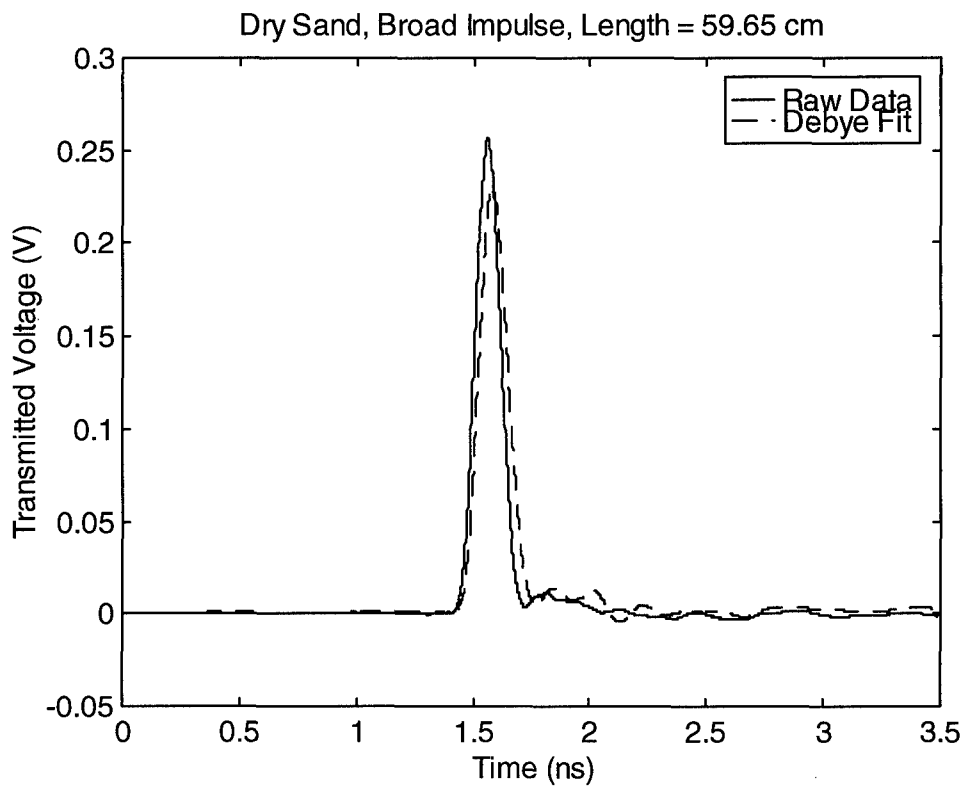
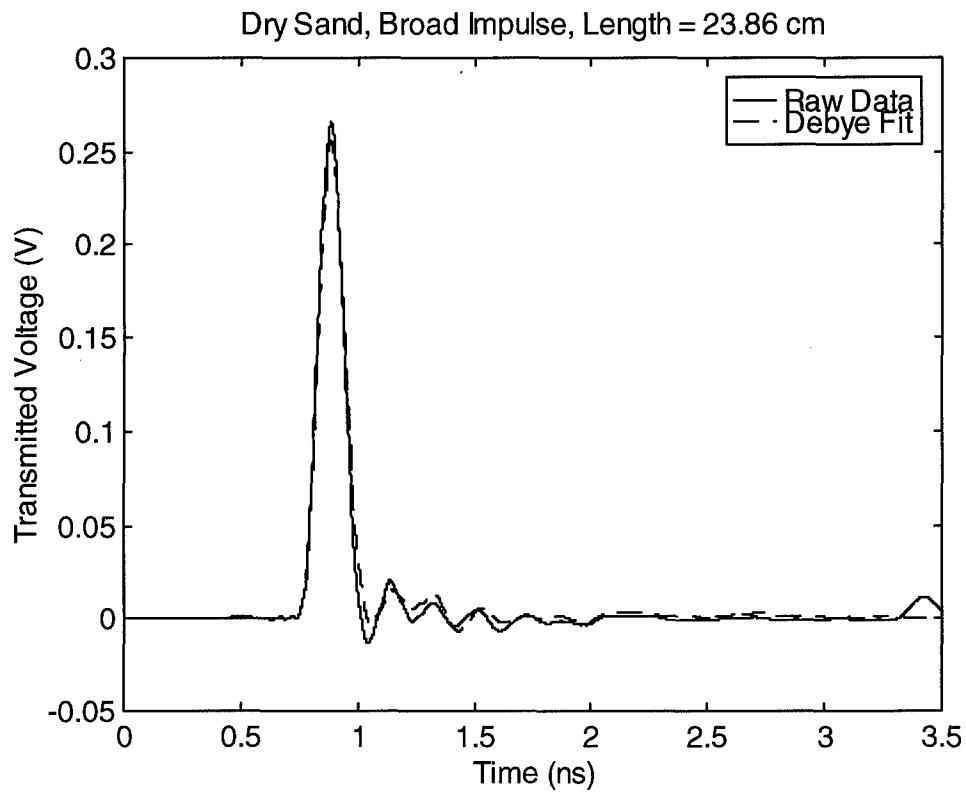


Figure 5.2. Propagation through 23.86 cm and 59.65 cm of dry sand, raw data and prediction with Debye model.

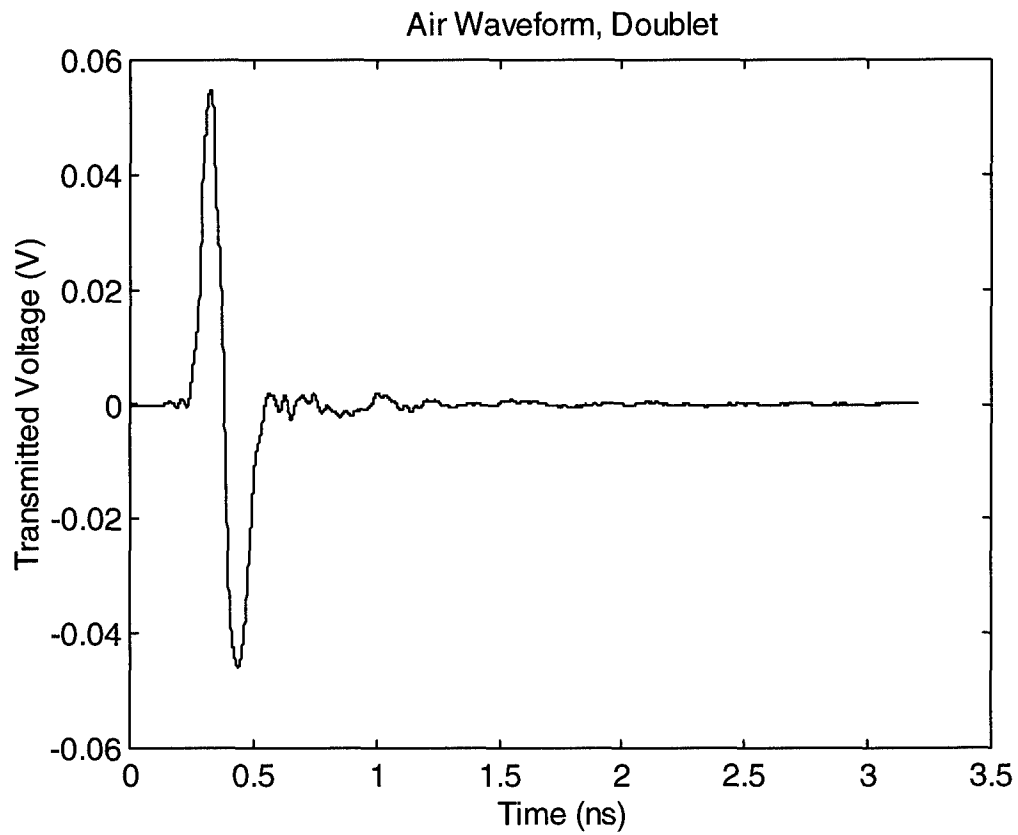


Figure 5.3. Air waveform for the doublet waveshape.

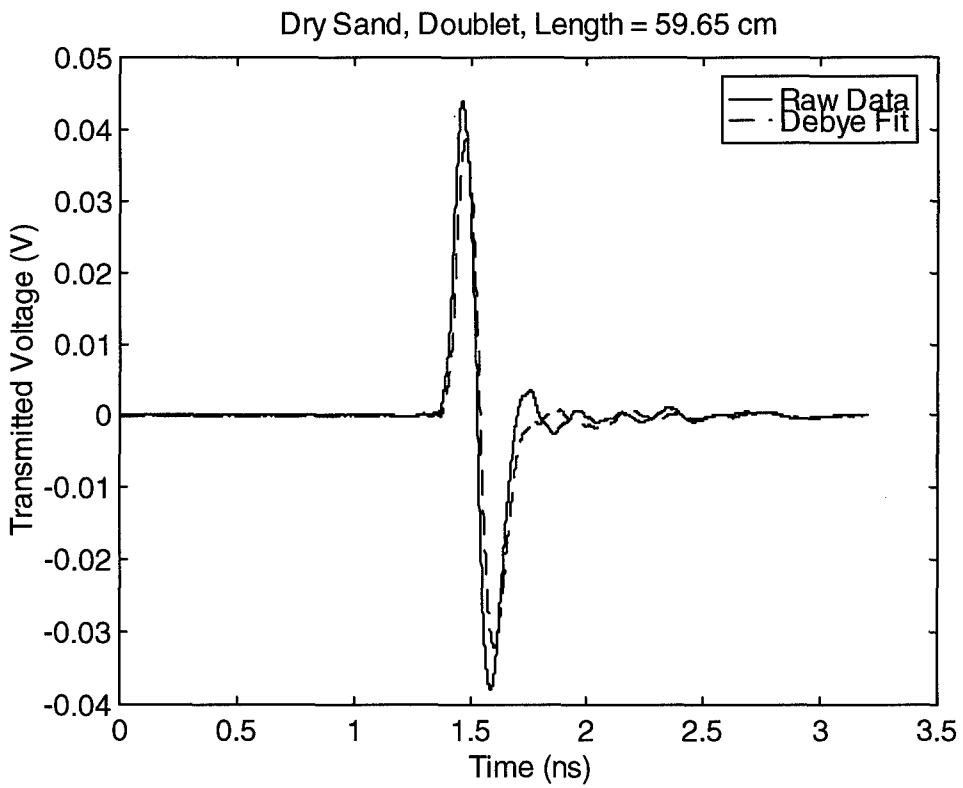
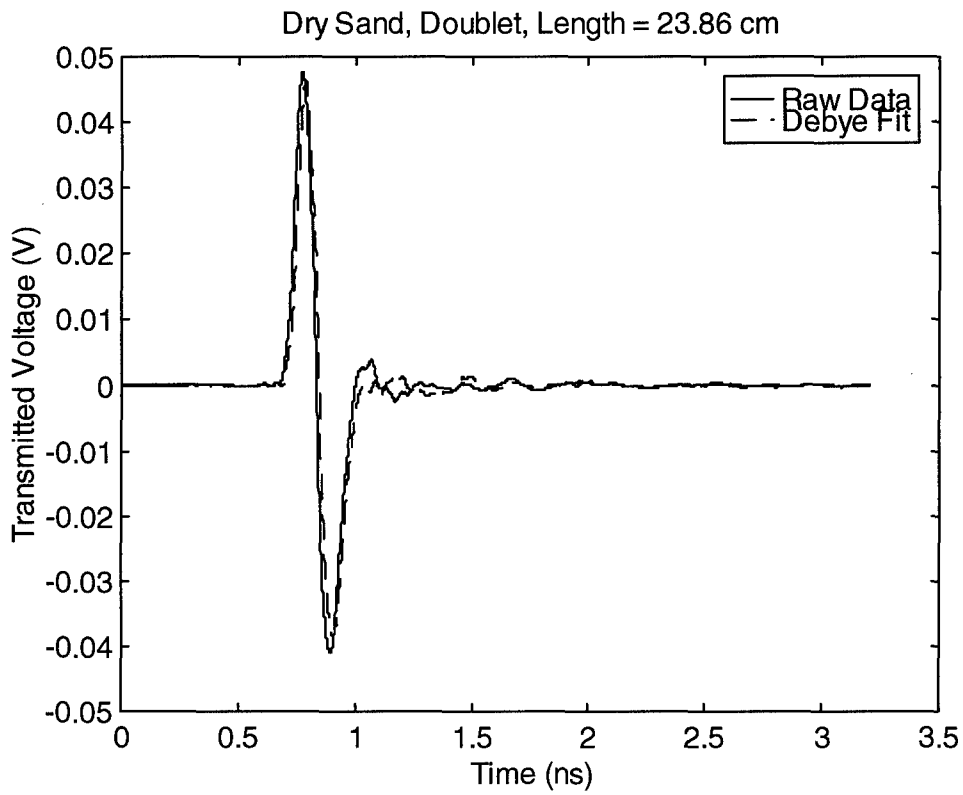


Figure 5.4. Propagation through 23.86 cm and 59.65 cm of dry sand, raw data and prediction with Debye model.

VI. Dry Sand: Propagation Waveshapes and Data Compilation

Having determined the Debye model for dry sand, we now show how this material propagates a Gaussian pulse of various widths out to a variety of distances. In doing so, we attempt to provide some insight for system studies. We consider Gaussian pulses with FWHM of 30, 100, and 300 ps, and propagation distances of 0.1, 1, and 10 meters.

A diagram of the input Gaussian pulses is shown in Figure 6.1. The transmitted pulses are calculated by convolving the input Gaussian pulses with the model transfer function for the three distances. Examples of the transmitted pulses are shown in Figures 6.2 through 6.4. The time delays of the waveforms have been adjusted arbitrarily to enhance clarity. From these graphs, we can clearly see the attenuation and pulse spreading of the pulses as they propagate.

Next, we compile the data in Figures 6.2-6.4, by plotting various characteristics on log-log scales. This will prove to be a useful representation of impulse propagation for use in system studies. First, we plot the peak magnitude for the three waveforms, at various distances (Figure 6.5). Next, we plot the FWHM of the waveforms, normalized to the FWHM of the input Gaussian (Figure 6.6). Finally, we plot the energy density of the waveforms (Figure 6.7), and the energy density normalized to the energy density of the input waveform (Figure 6.8). The energy density of a waveform is calculated as

$$\text{Energy Density} = \int_0^{\infty} E(t) H(t) dt \quad (6.1)$$

where $H(t)$ is calculated from $E(t)$ using the Debye model dielectric constant.

As we expect, the magnitude decreases and the FWHM increases with propagation distance. It is a bit unexpected, however, that the 30 ps pulse loses only a factor of ten in energy, after propagating ten meters. This may well be a tolerable loss in an actual system.

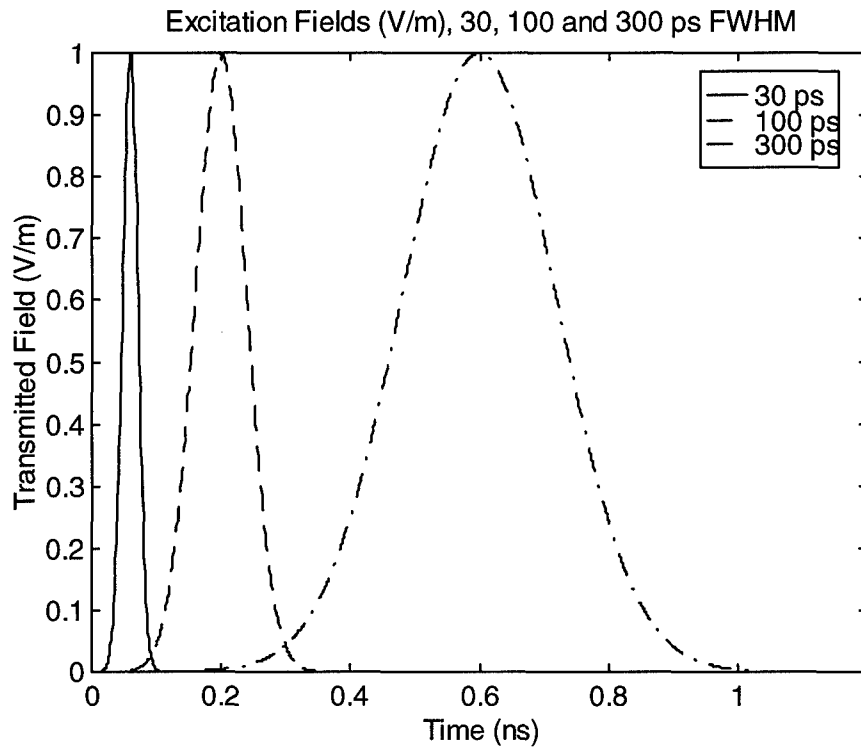


Figure 6.1. The input Gaussians for this study, FWHM = 30, 100, and 300 ps.

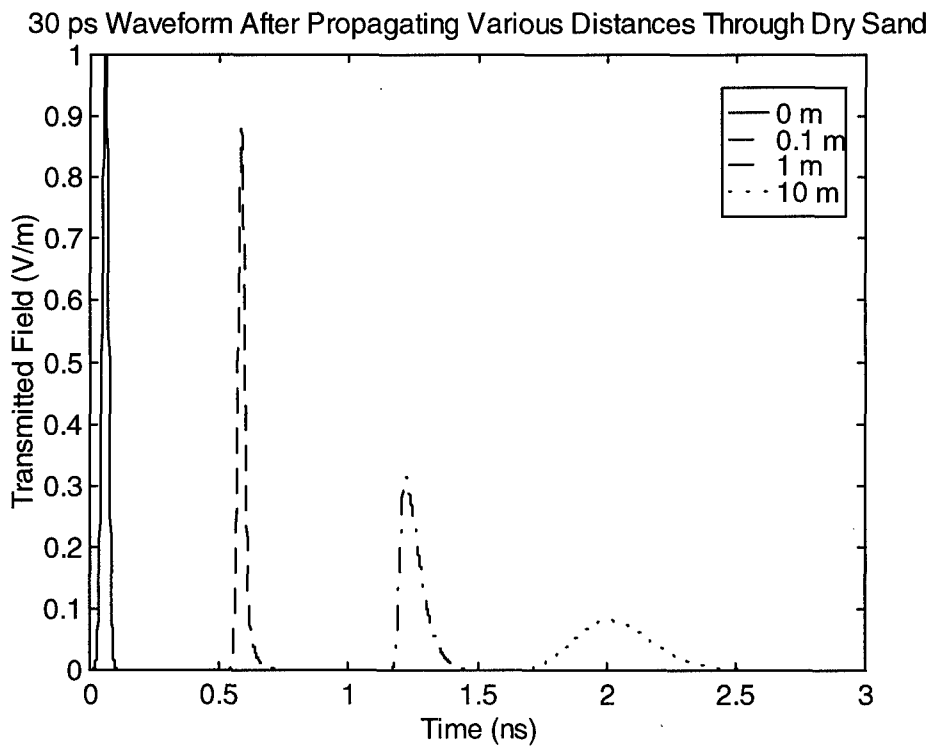


Figure 6.2. The propagated field of the 30 ps pulse at 0, 0.1, 1, and 10 meters. (Starting times shifted for clarity.)

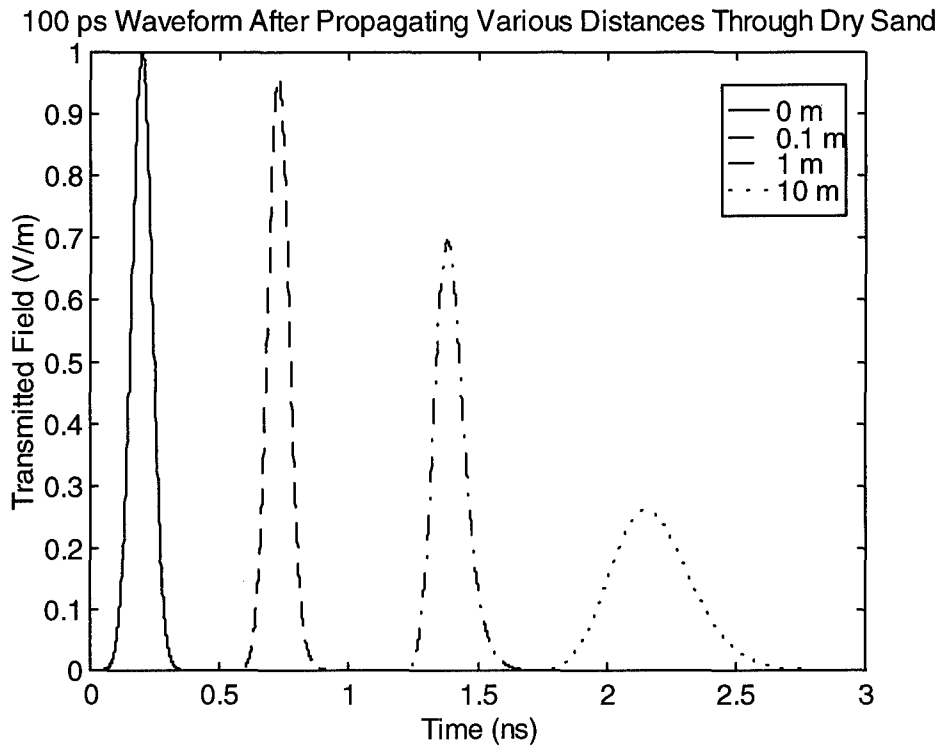


Figure 6.3. The propagated field of the 100 ps pulse at 0, 0.1, 1, and 10 meters. (Starting times shifted for clarity.)

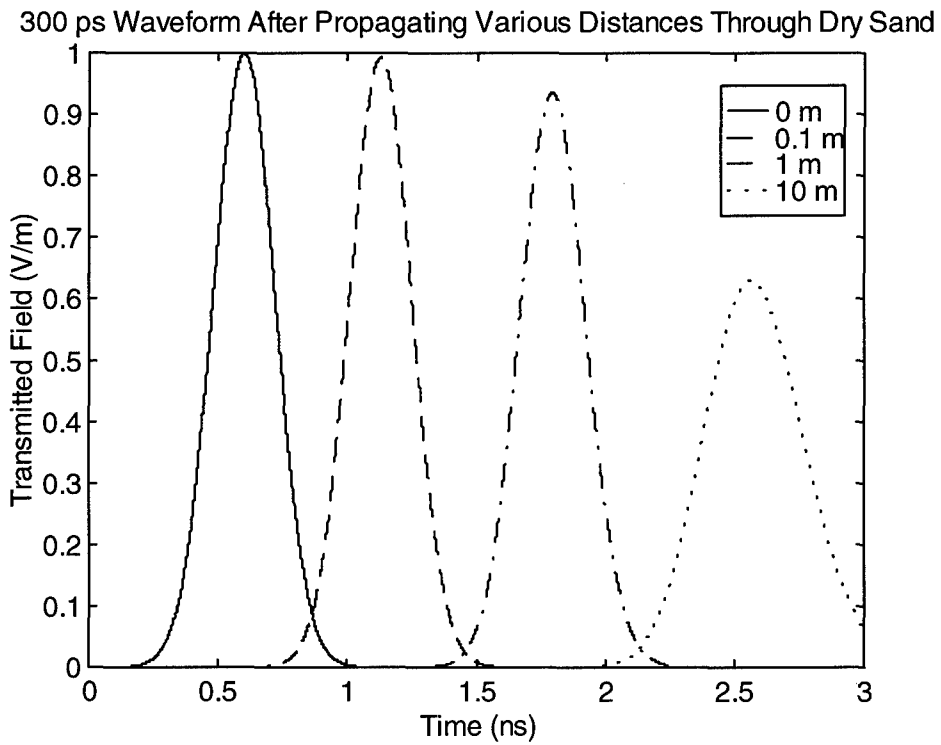


Figure 6.4. The propagated field of the 300 ps pulse at 0, 0.1, 1, and 10 meters. (Starting times shifted for clarity.)

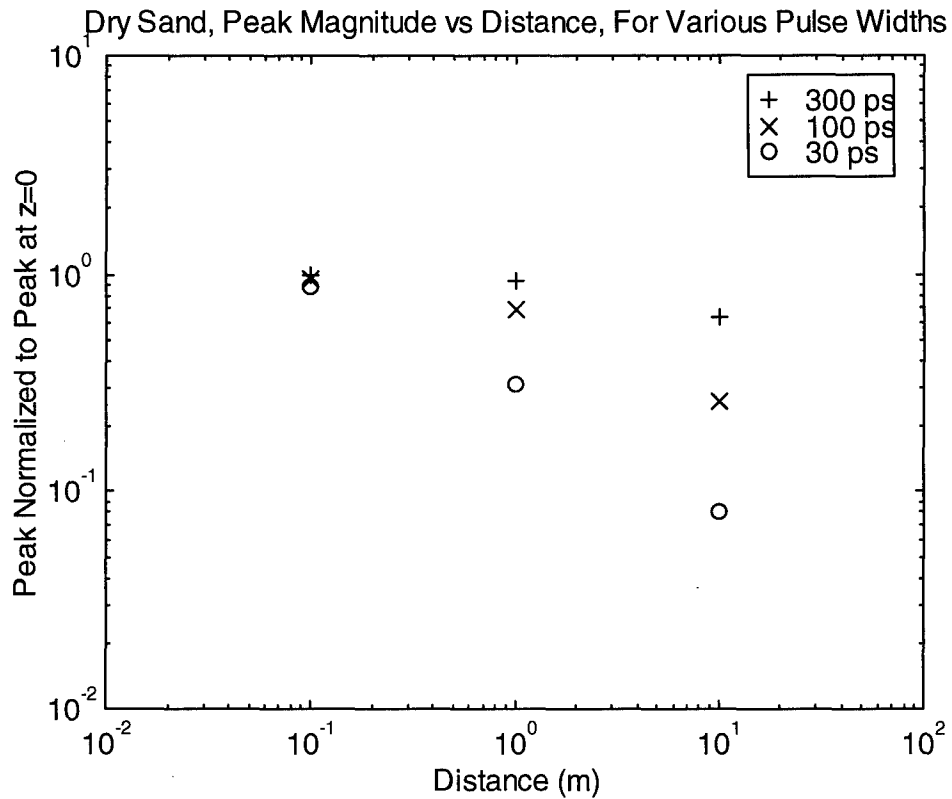


Figure 6.5. Peak waveform magnitude as a function of FWHM and propagation distance.

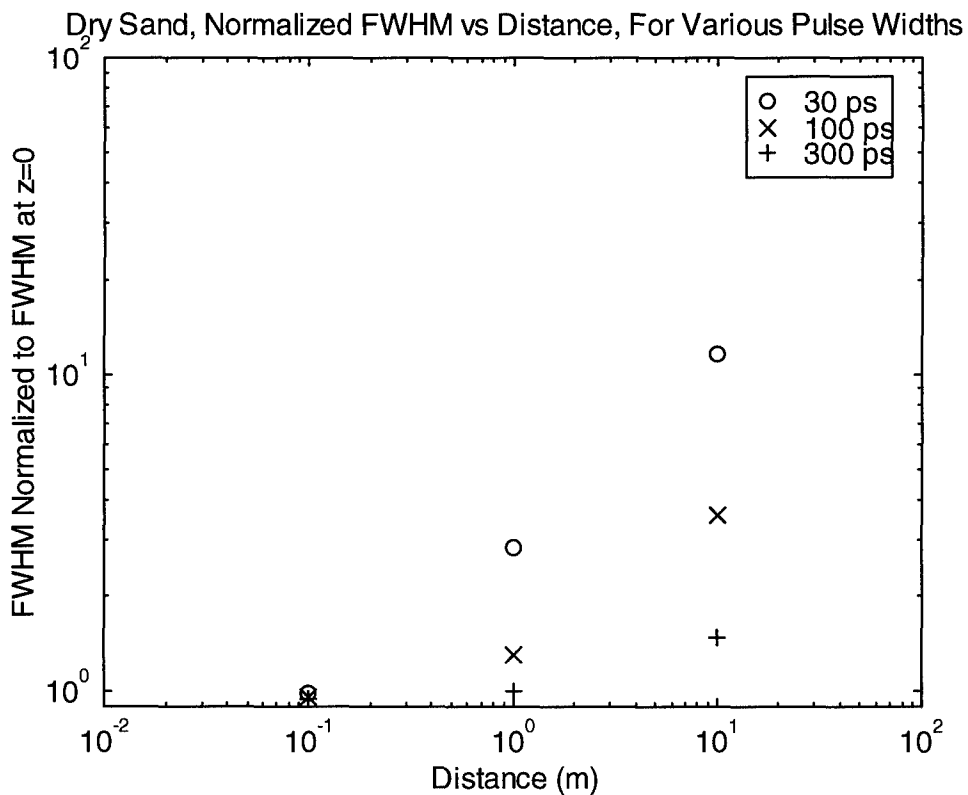


Figure 6.6. Normalized FWHM as a function of input FWHM and propagation distance.

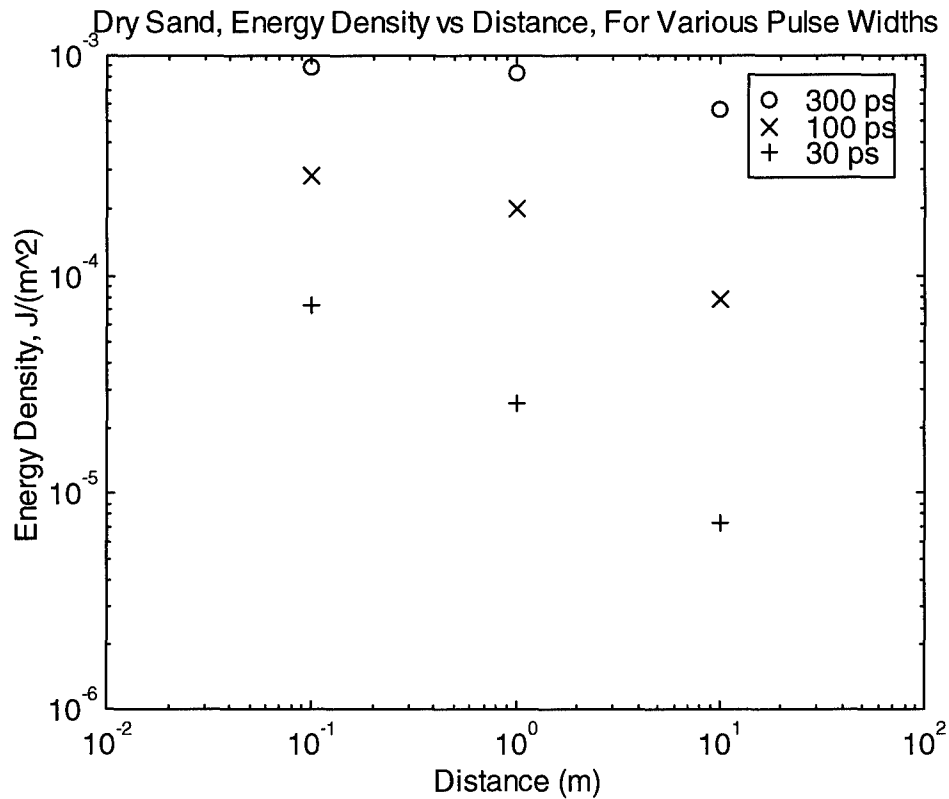


Figure 6.7. Energy density as a function of input FWHM and propagation distance.

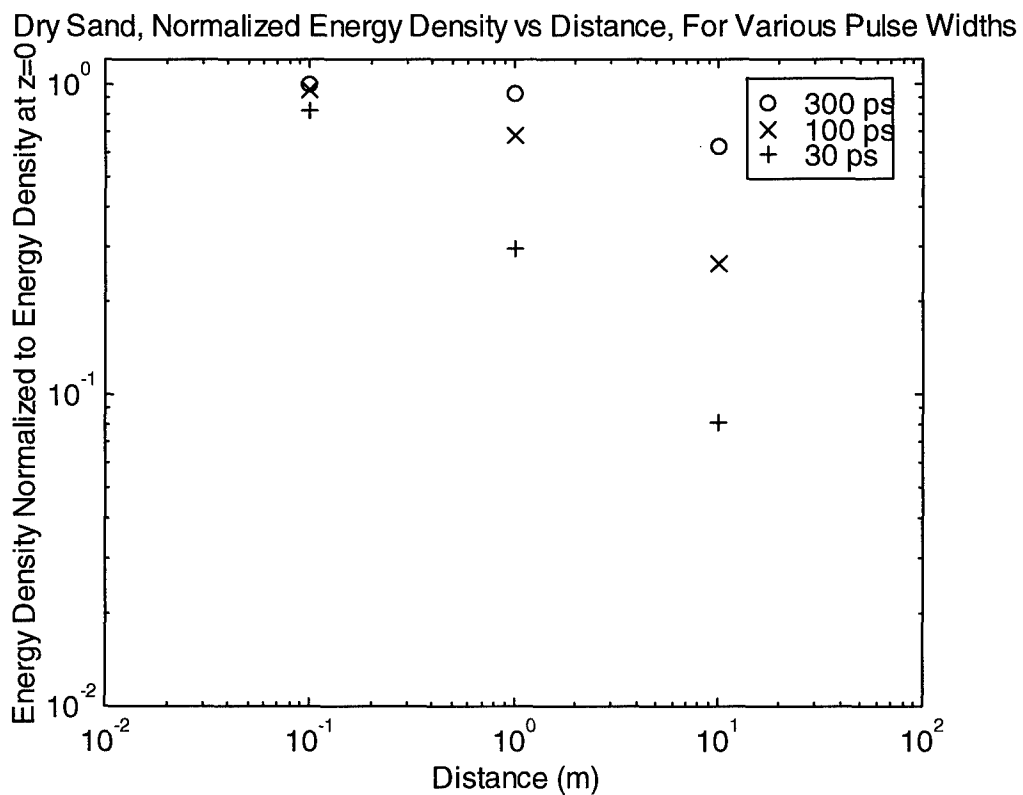


Figure 6.8. Normalized Energy density as a function of input FWHM and propagation distance.

VII. Concrete: Measurements

We consider now the measurement of the dielectric constant of concrete, using same technique as in [1].

Careful sample preparation of the concrete was essential, since attenuation values vary with the age and water content of the concrete sample. Seven uniform annular concrete samples were cast by pouring wet concrete mixture into a flexible silicone mold. The annular samples were inserted into the coaxial transmission line apparatus for the propagation measurements.

A three-step process was employed to form the samples. First, an aluminum master (positive) was made by computer numerical controlled machining. The master was fabricated to an accuracy of .00254 cm (0.001 inch). A slight taper was included in the master to aid removal of the mold. Next, the silicone mold (negative) was made from the aluminum master using a two-part RTV silicone rubber compound. The mold was heated two hours at 65° C and then removed from the aluminum master. The resulting flexible silicone mold was ideal for casting concrete or any other castable material into annular slugs for measurement in the coaxial line apparatus.

The concrete mixture was prepared from commercial ready-mix concrete which is a 3-to-1 mixture of sand-to-Portland cement. The ready-mix was sifted to remove larger aggregate (pea gravel), and mixed with water in the ratio of 28 cc water to 100 cc sifted ready-mix. The wet mixture was poured into the silicone mold and leveled to a 3 cm height.

The annular concrete samples were removed from the mold after 12 hours. The samples were cured 10 days at room temperature. Next, the samples were baked in an oven at 200° F for 24 hours to drive off excess moisture. Finally, the samples were cured for an additional two days. The curing sequence was intended to simulate the natural drying action, which would occur over a much longer period in the ambient environment.

Seven annular concrete samples were prepared by the above procedure for use in the experiment. The samples were weighed with a precision digital laboratory scale which was calibrated with a calibration mass. The outside diameter (OD), inside diameter (ID), and length (L) were next measured with precision dial calipers. Each of the seven samples was uniquely numbered. The mean parameters for the samples were a mass of 41.72 grams, an OD of 3.475 cm, an ID of 1.594 cm, and a length of 2.896 cm. These numbers were used to calculate a mass density of 1.92 grams/cc for the cured concrete which was used in the propagation measurements.

The experimental setup for the ultra-wideband impulse propagation measurements through concrete is shown in Figure 7.1. The setup was virtually identical to that described in [1] for measurements of distilled water. A 24-inch Goretex cable was used between the coax line fixture and the sampling head in place of the 9-inch semi-flex cable which had been used for the water measurement.

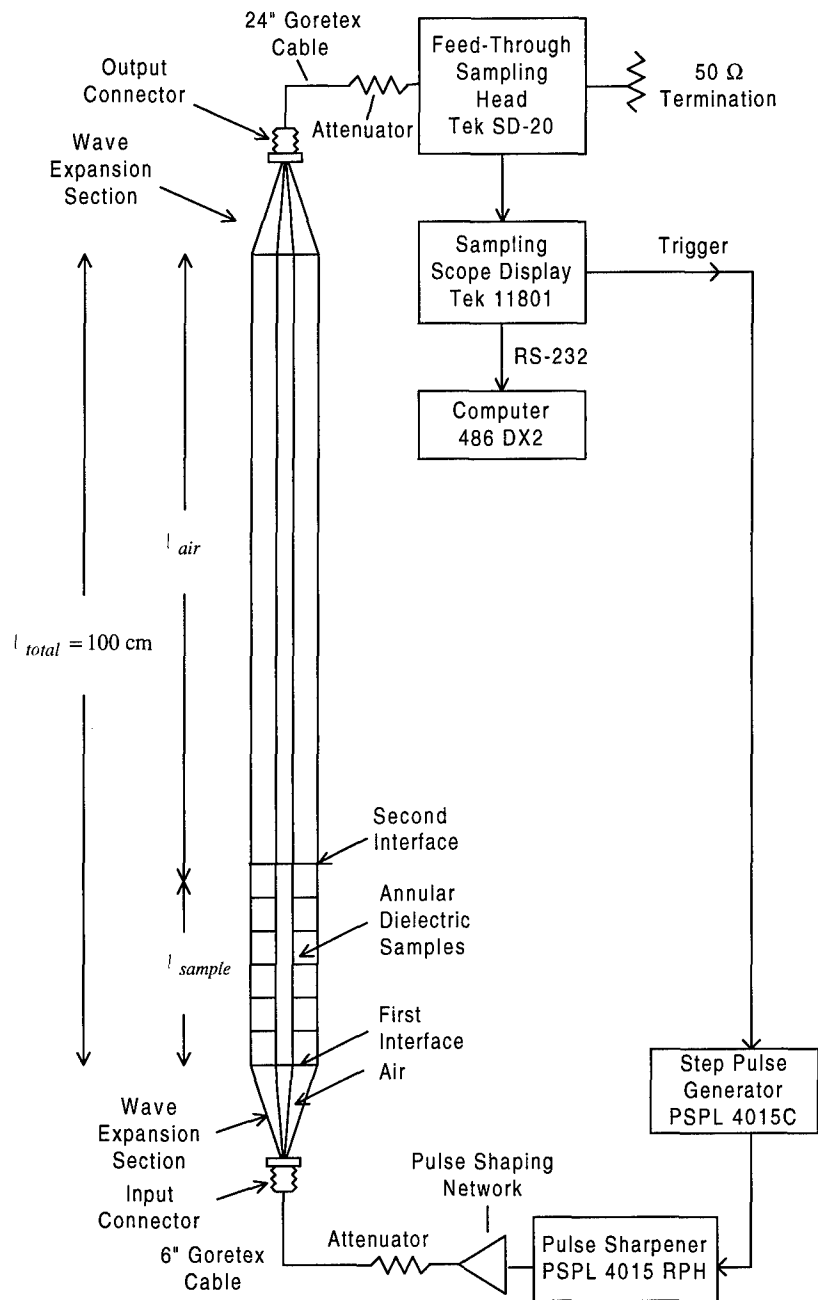


Figure 7.1. Instrumentation setup for measurements in transmission mode with various waveshapes.

Three different waveforms were used. The Picosecond Pulse Lab model 4015C step generator was used with various pulse shaping networks to produce impulse, step, and doublet waveforms. These waveforms were propagated through the coaxial transmission line apparatus to the Tektronix model 11801 sampling digitizer using type SD20 sampling head. Precision 3.5 mm attenuators were used to reduce the signal level and to absorb multiple reflections. For the step waveform, a 10 dB attenuation value was used at both the input and the output to the coax

line apparatus, while a 3 dB attenuation value was used for the impulse and doublet measurements.

For the impulse waveform, the pulse shaping was accomplished with a single impulse former (differentiating network) attached directly to the source output. For the doublet waveform, two impulse formers were used along with a 100 ps risetime standard. For the step waveform, no pulse shaping was employed. Other details of this test setup are as given in [1].

Measurements were taken with three different temporal waveshapes (impulse, doublet, and step) to compare propagation to theoretical predictions. The material dielectric response, determined using the impulse waveshape, was then used to predict the pulse evolution with propagation distance for the doublet and step waveshapes. For each waveshape, a reference waveform ($\ell = 0$ cm) was taken with only air in the coaxial fixture. Then, the annular concrete slugs were added one at a time, and data waveforms were recorded for each propagation distance. It must be noted that as material samples are inserted into the coaxial line, the length of the air path is reduced by the sample length. This reduction of air path must be considered in data analysis.

Table 8.1 lists raw data and waveform file names for a narrow impulse propagating through concrete. The pulse width and amplitude were read directly from the digitizer using the measurement mode. The pulse width refers to the FWHM and amplitude to the 0% to 100% amplitude calculation with the built-in IEEE algorithm. The raw data shows that the pulsewidth broadens and that the amplitude decreases as the propagation distance increases. This effect can be seen graphically in Figure 8.1, which shows an overlay of all eight pulses.

The pulse is shifted to a later time as the length of material is increased. The time increment is almost identical for each sample. The approximate index of refraction, $n = c/v$, can be calculated from this data using the formula $n = (c \Delta t / \Delta \ell) + 1$, where Δt and $\Delta \ell$ are the differential time and length computed from any pair of waveforms. The times are measured to 10% of peak amplitude rather than 50% in order to minimize the effect of the finite pulse risetime. Comparison of any pair of waveforms gives an index of approximately 1.8. In other words, the wave speed in concrete is approximately half of the free space velocity. The dielectric constant, which is the square of the index ($\epsilon_r = n^2$), is 3.2. This is an approximate calculation because we are calculating the group velocity for the impulse and the calculation ignores the frequency dependent propagation speed.

The data for propagation of the doublet and step waveforms is listed in Table 9.1. It can be seen that the amplitude of the doublet decreases with increasing propagation distance, while the risetime of the step waveform is degraded with propagation distance. This is the expected behavior for propagation through a dispersive medium. The measured ratio of the step waveform amplitude for a wave passing through the concrete to the step amplitude for the air path is 0.92 (ratio of 371 mV to 402 mV in Table 9.1). The Fresnel equations (Eqn. 5.1) also predict a transmission coefficient of 0.92 for $\epsilon_r = 3.2$. The agreement with the expected transmission coefficient gives a self-consistency check to the raw data.

VIII. Concrete: Data Processing and Fit to Dielectric Constant Model

We provide here a complete set of data for concrete, as described in the previous section. This data is very similar to that provided earlier for distilled water in [1]. The measurement technique is the same, and the processing is almost exactly the same, with minor exceptions as noted below.

First, we provide all eight raw waveforms which were taken with the impulse, in Figure 8.1. The raw data are summarized in Table 8.1. Examination of the data shows that concrete is a reasonably good medium for propagating narrow impulses.

The air waveform of the impulse (FWHM = 41.3 ps) through the coaxial test fixture is shown in Figure 8.2. This is simply the waveform after it has passed through the coax test fixture when no material is present. The waveform is shown in both the time and frequency domains, in order to show the effective bandwidth of the measurement system. The frequency domain plot shows an effective bandwidth in the system of around 20 GHz

Next, we show the transmitted voltage waveform after propagating through 11.53 cm and 20.27 cm of concrete (Figure 8.3). This is the raw data upon which the dielectric constant calculation is based. The ratio of these two waveforms in the frequency domain represents the impulse response for the difference of the two lengths, or 8.74 cm. The ratio was taken by limiting the smallest value of the denominator to 1% of its peak in the frequency domain, and by applying a 10th-order modified Butterworth filter at 25 GHz. The resulting ratio is shown in Figure 8.4, and the corresponding time domain impulse response and its integral are shown in Figure 8.5.

An interesting feature of the data is the overshoot in the transmitted voltage waveform after propagating through concrete. This is seen both in the transmitted waveform through 20.27 cm of concrete (Figure 8.3), and in the resulting impulse response (Figure 8.5). We originally thought this overshoot might be an error in the measurement, but after checking our setup we found the overshoot is a real physical effect. This overshoot is not present in our measurements of water or dry sand.

With the above data, we can now calculate the dielectric constant, using the techniques of [1]. The real and imaginary parts of the dielectric constant are shown in Figure 8.6. The corresponding attenuation is shown in Figure 8.7. Note that although these curves were generated from a single pair of waveforms, similar results were obtained with other waveform pairs, so our results are self-consistent.

A Lorentz model fit was generated for the above dielectric constant data. We had to use a Lorentz model instead of the Debye model used previously with water and dry sand, because of the overshoot in the impulse response. A Lorentz model is simply a fit of the dielectric constant to a constant plus a damped sine [2, pp. 139-144]. This is expressed in the frequency and time domains as

$$\begin{aligned}\epsilon_r(\omega) &= \epsilon_\infty + (\epsilon_s - \epsilon_\infty) \frac{(\alpha^2 + \beta^2)}{(\alpha^2 + \beta^2) + j2\omega\alpha - \omega^2} \\ \epsilon_r(t) &= \epsilon_\infty \delta(t) + (\epsilon_s - \epsilon_\infty) \frac{\alpha^2 + \beta^2}{\beta} e^{-\alpha t} \sin(\beta t)\end{aligned}\tag{8.1}$$

where ϵ_∞ is the relative dielectric constant at high frequencies, ϵ_s is the relative dielectric constant at low (static) frequencies, α is the decay constant, and β is the radian frequency. The Lorentz model fit was implemented using a least mean square fit to the dielectric constant data between 1 and 15 GHz. A plot of the resulting Lorentz model fit is shown in Figure 8.6, and the corresponding attenuation is shown in Figure 8.7. A table of our fitted values for these parameters is shown in Table 8.2. The fit to the real part of the dielectric constant is quite good at midband. The fit to the imaginary part of the dielectric constant is somewhat low at the low frequencies. In certain circumstances this can lead to an underprediction of the attenuation.

Before proceeding, let us consider the meaning of the Lorentz model. Since it generates a negative dielectric constant at very high frequencies, we ascribe no particular physical meaning to the model. It's main usefulness is as a compact description of the dielectric constant as a function of frequency in terms of four parameters. This model has a very interesting behavior at very high frequencies. However, it is not valid above 20 GHz, since that is the frequency range of our measurements. It would be incorrect to apply the model beyond the frequency range of our measurements.

Finally, we consider what happens if we convolve the Lorentz model of the material with the air waveform. We do this as a check on whether we have successfully modeled the measured waveforms in Figure 8.3, which were used to generate the model. The results for propagation through 11.53 cm and 20.27 cm of concrete are shown in Figure 8.8. We see that there is quite good agreement between the model predictions and the actual measurements.

We hypothesize now that the above Lorentz parameters will be sufficient to predict the transmitted voltage through other lengths of concrete, and using other wave shapes. This is demonstrated in the section that follows.

Table 8.1. Experimental Data For Transmission Through Concrete In Coax Line With a Narrow Impulse.

Sample Length (cm)	Pulsewidth FWHM (ps)	Amplitude (mV)	File #
00.00	41.3	652.8	F7010601
02.87	48.8	537.6	F7010602
05.77	53.6	508.8	F7010603
08.66	60.4	467.2	F7010604
11.53	70.8	419.2	F7010605
14.45	75.3	384.0	F7010606
17.34	82.2	358.4	F7010607
20.27	88.4	336.0	F7010608

(NOTE: Air Length for all data = 100.00 cm – Sample Length)
Scope Delay = (84.12 + 0.2) ns for all data.

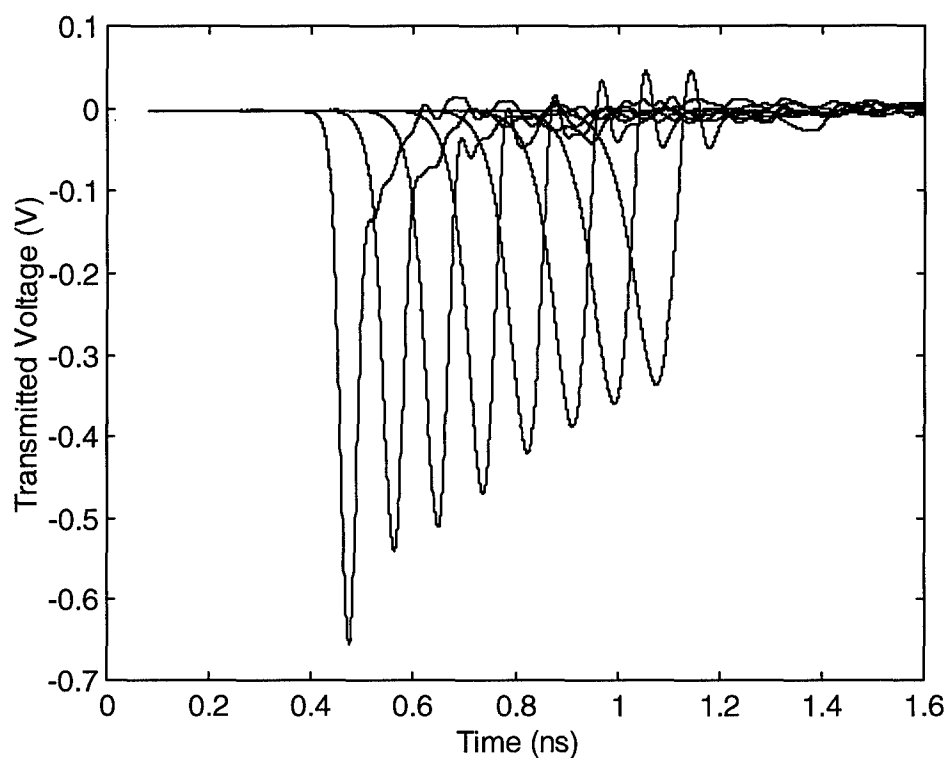


Figure 8.1. Propagation through concrete, with thicknesses of 0, 2.87, 5.77, 8.66, 11.53, 14.45, 17.34, and 20.27 cm.

Table 8.2. Lorentz Model Parameters for Concrete.

Parameter	Lorentz Model Fit for Concrete
ϵ_s	3.4369
ϵ_∞	-69.1625
α	13.94 ns ⁻¹
$f_{res} = \beta/(2\pi)$	224.45 GHz

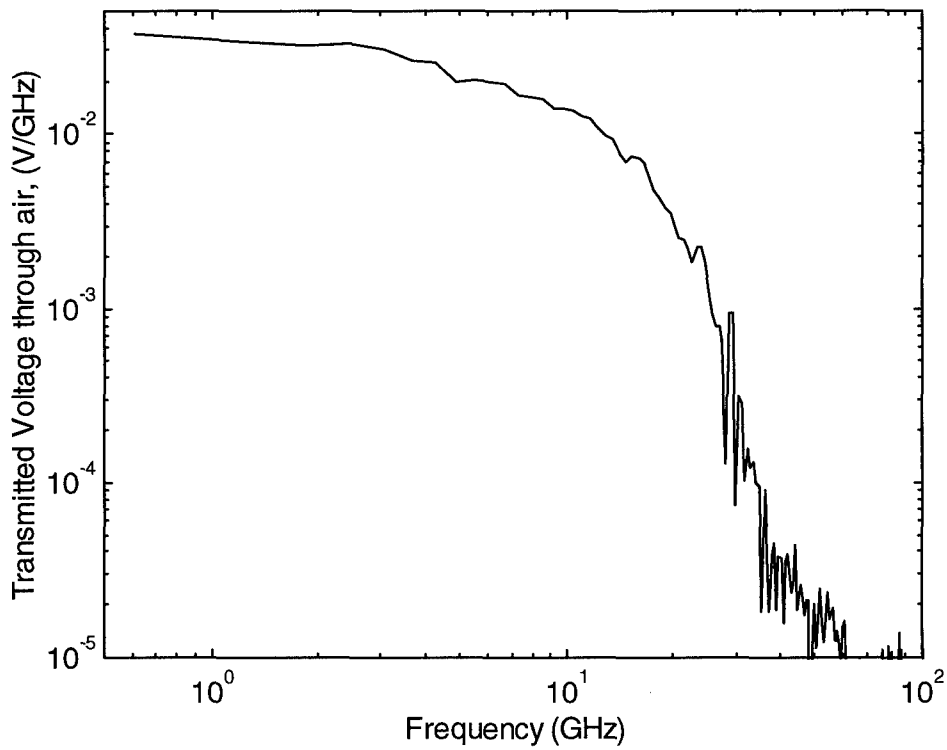
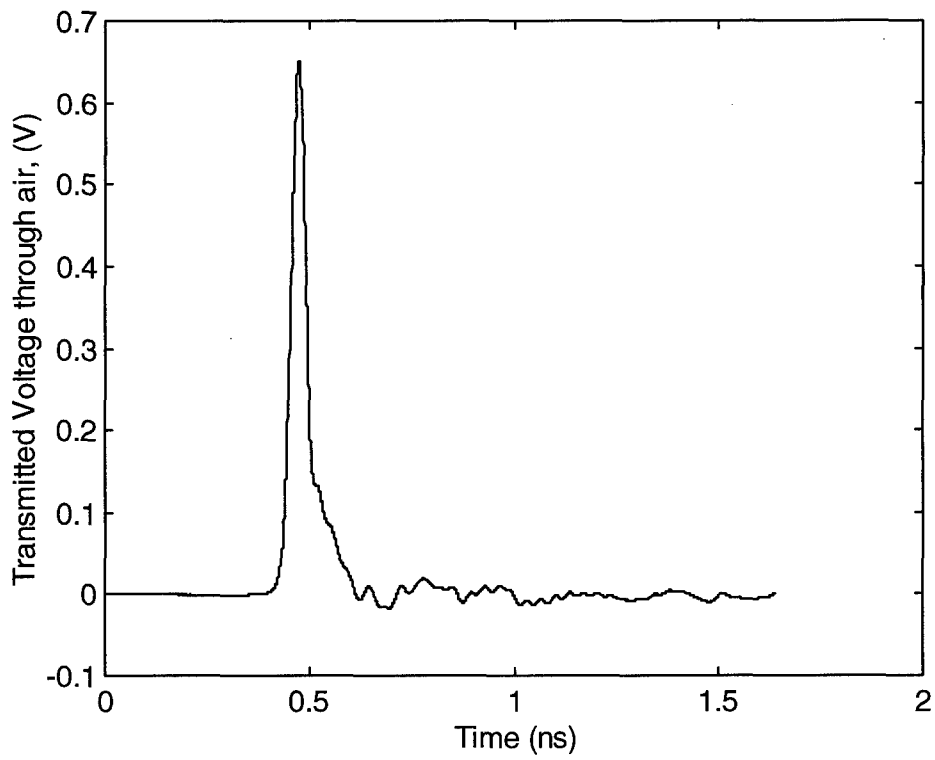


Figure 8.2. Air waveform for the concrete measurements, time domain (top) and frequency domain (bottom).

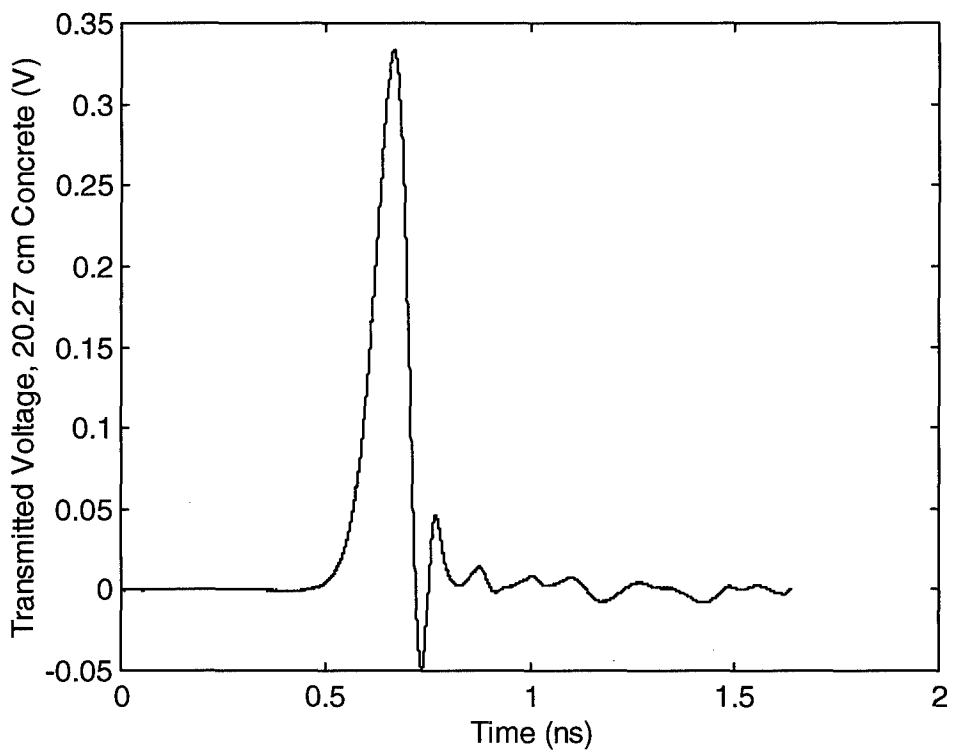
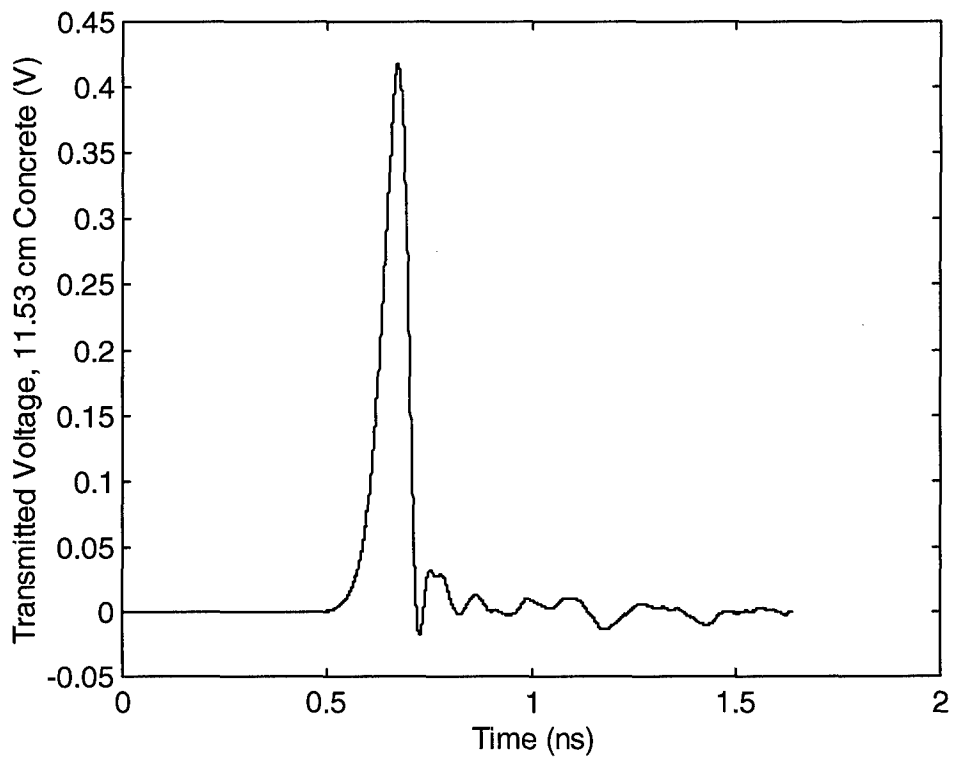


Figure 8.3. Transmitted signals through 11.53 cm and 20.27 cm of concrete.

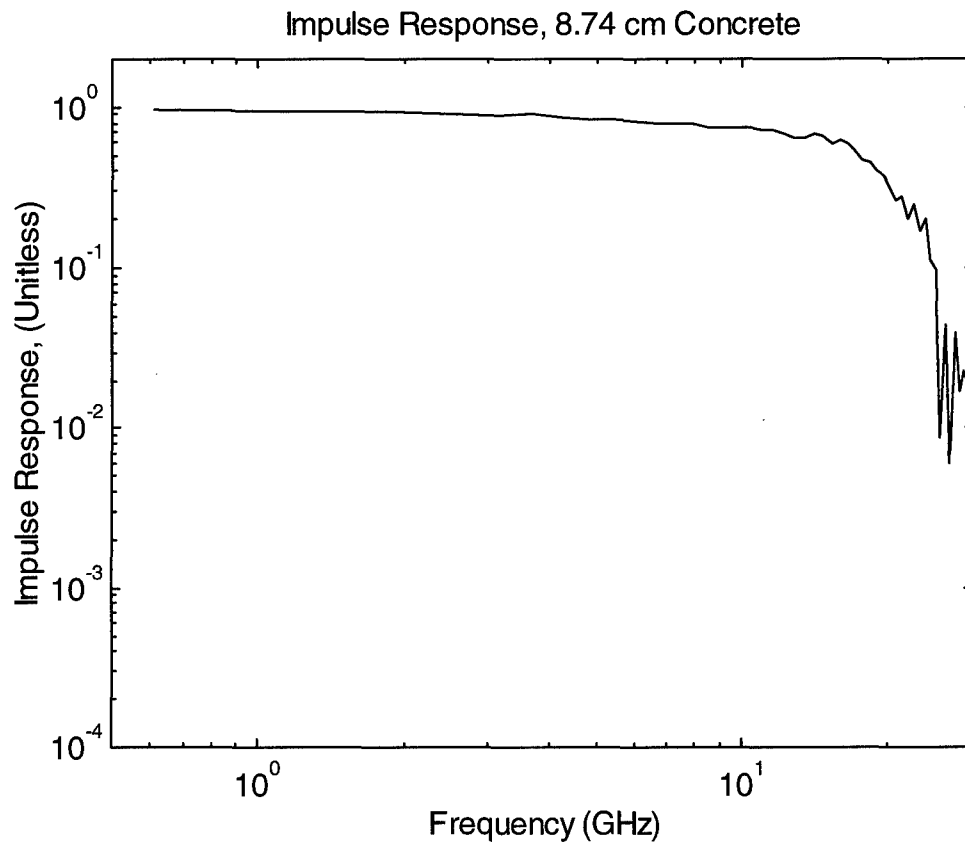


Figure 8.4. The impulse response of 8.74 cm of concrete.

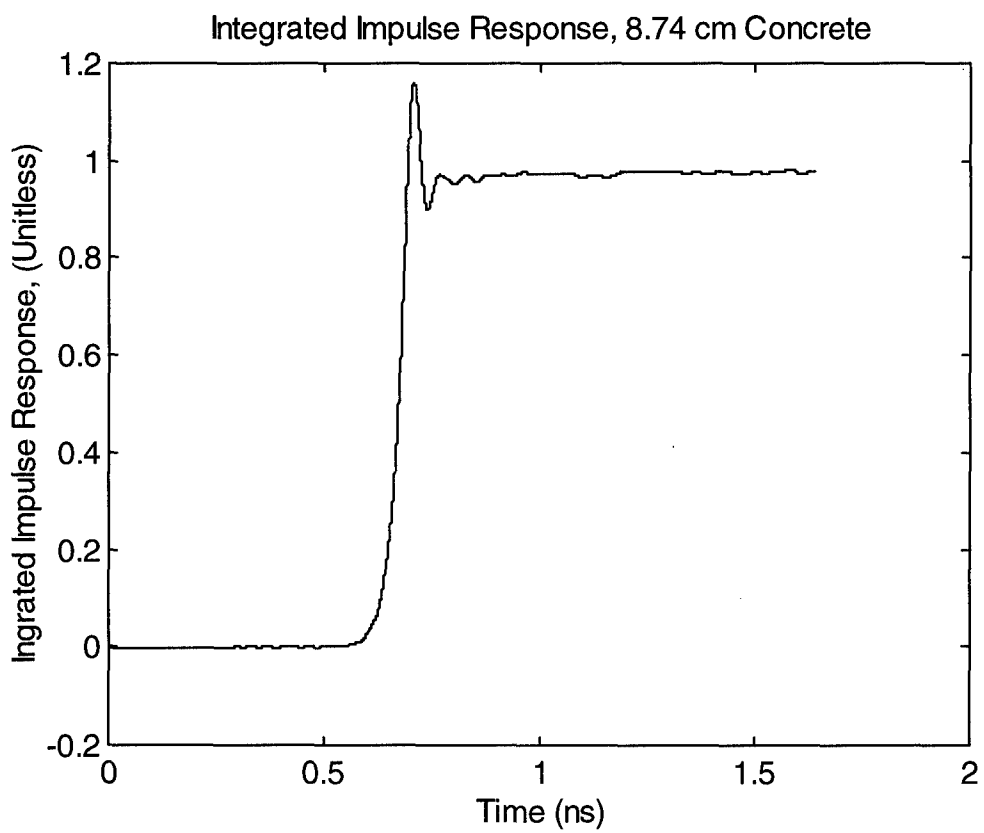
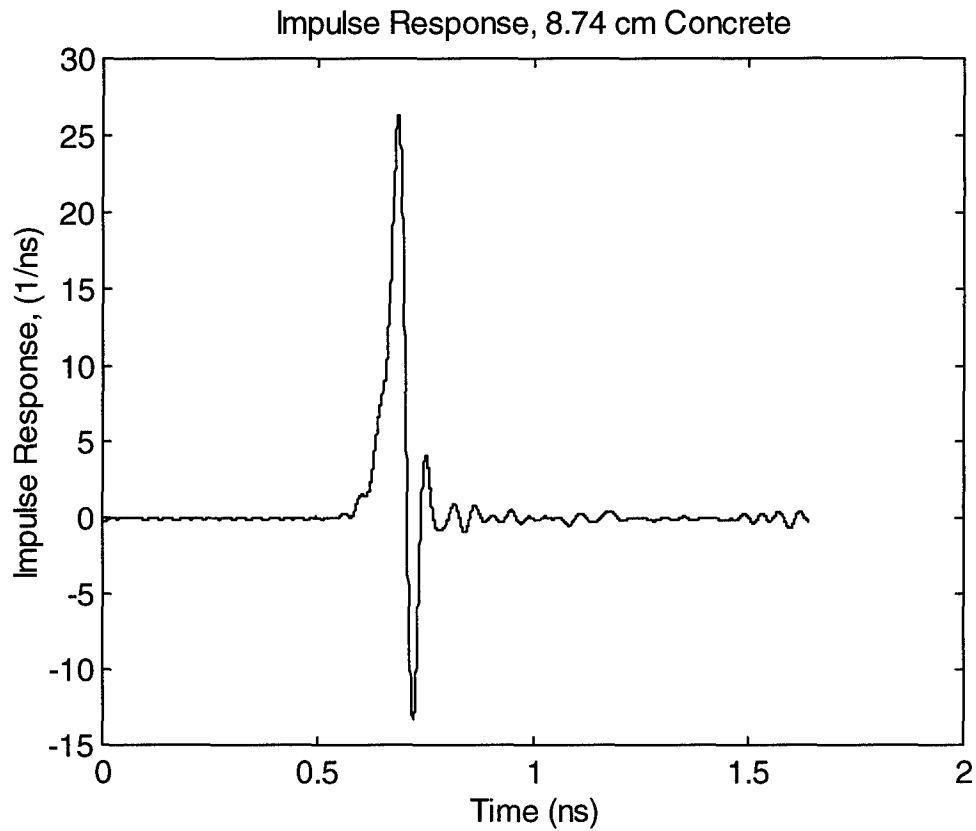


Figure 8.5. The impulse response (top) and its integral (bottom) of 8.74cm concrete.

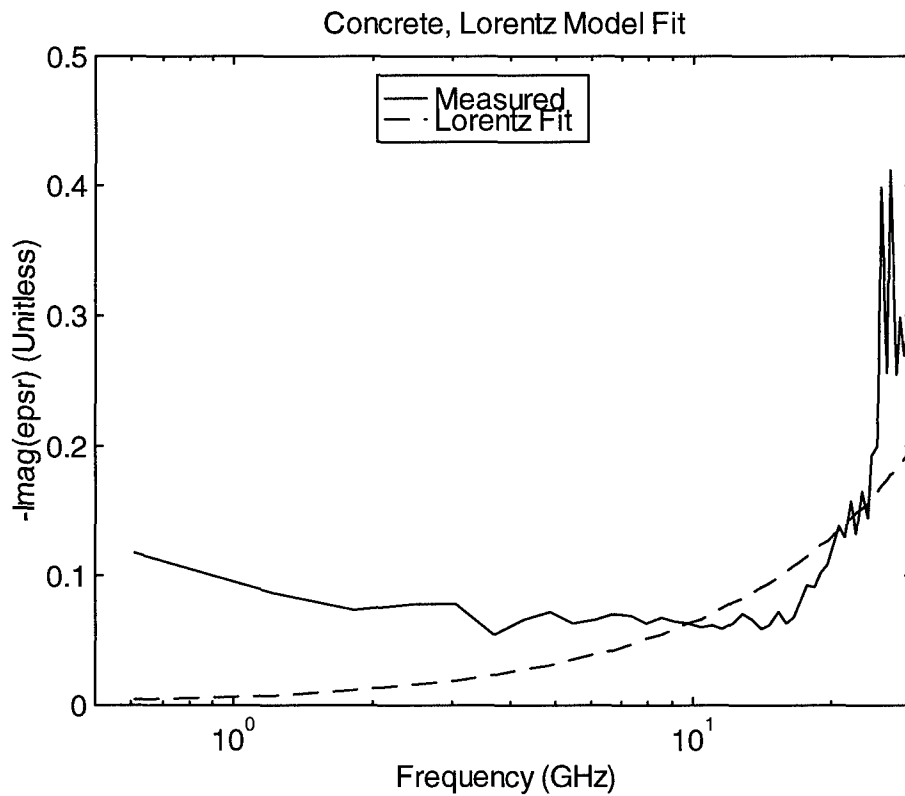
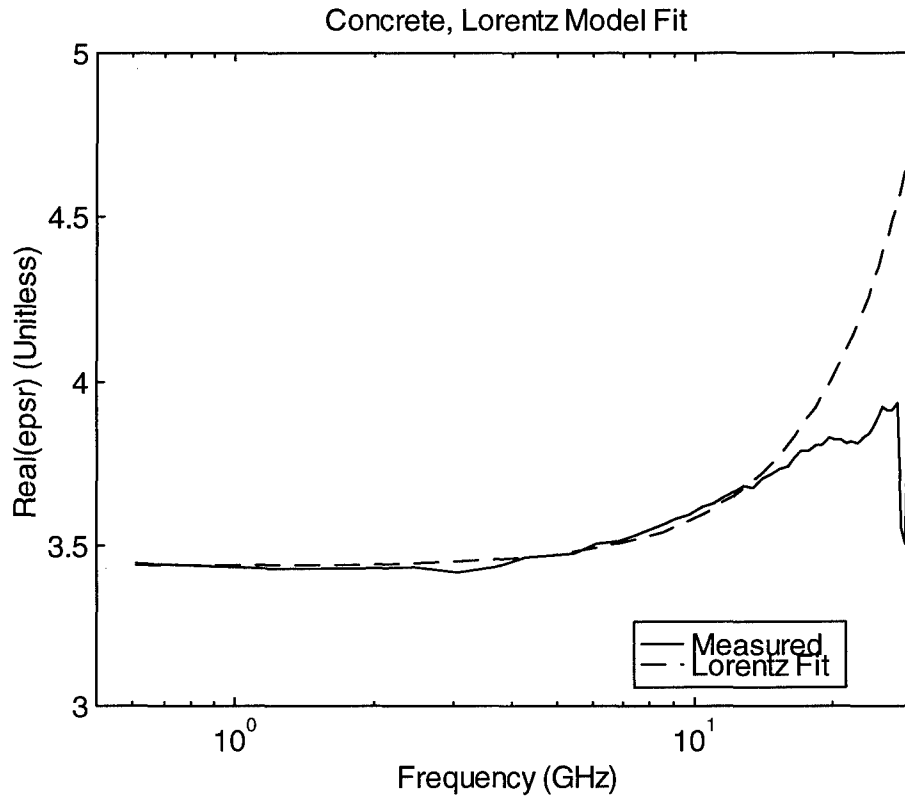


Figure 8.6. Measured dielectric constant of concrete, and the Lorentz model fit, real and imaginary parts.

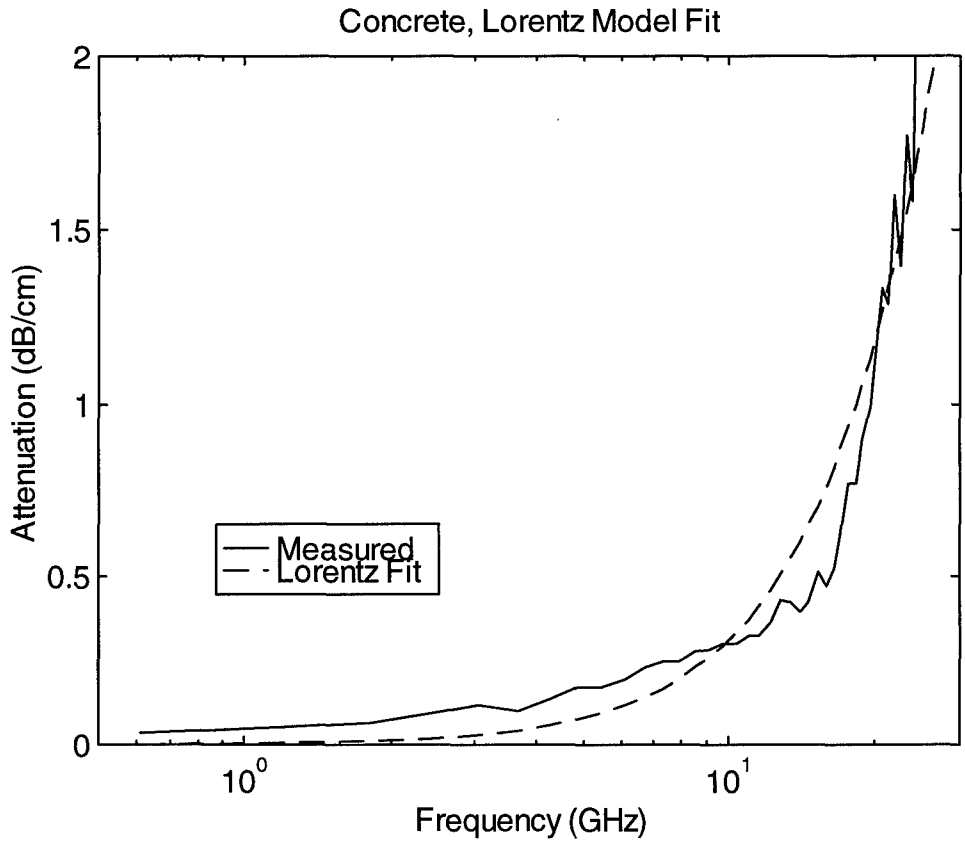


Figure 8.7. Attenuation constant of concrete, measured and Lorentz model fit.

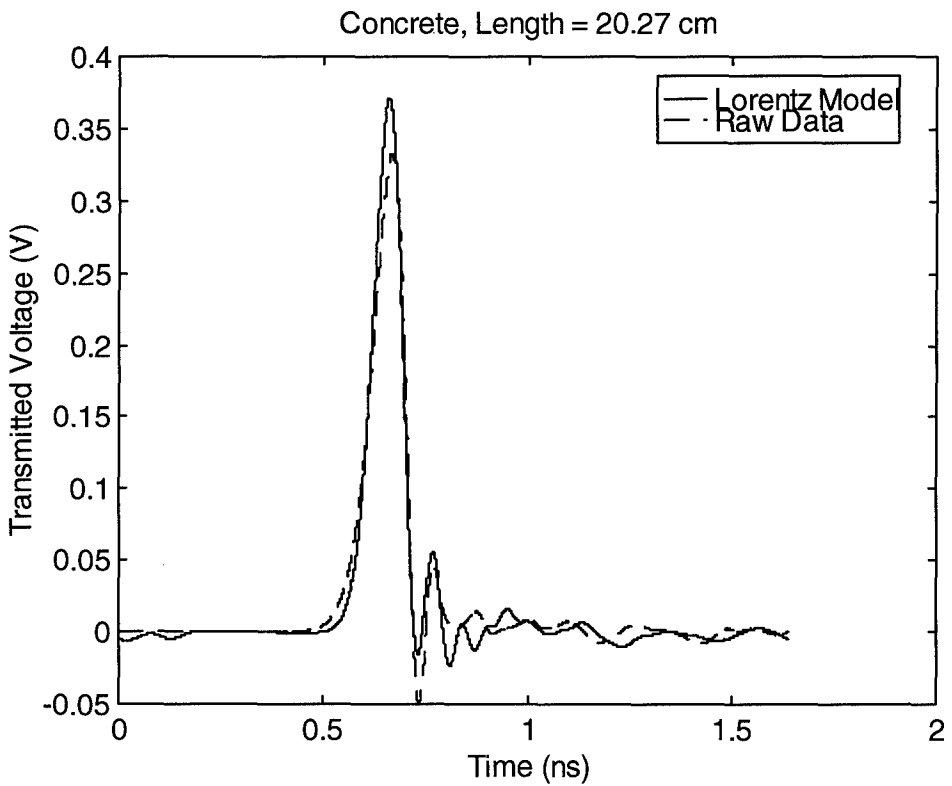
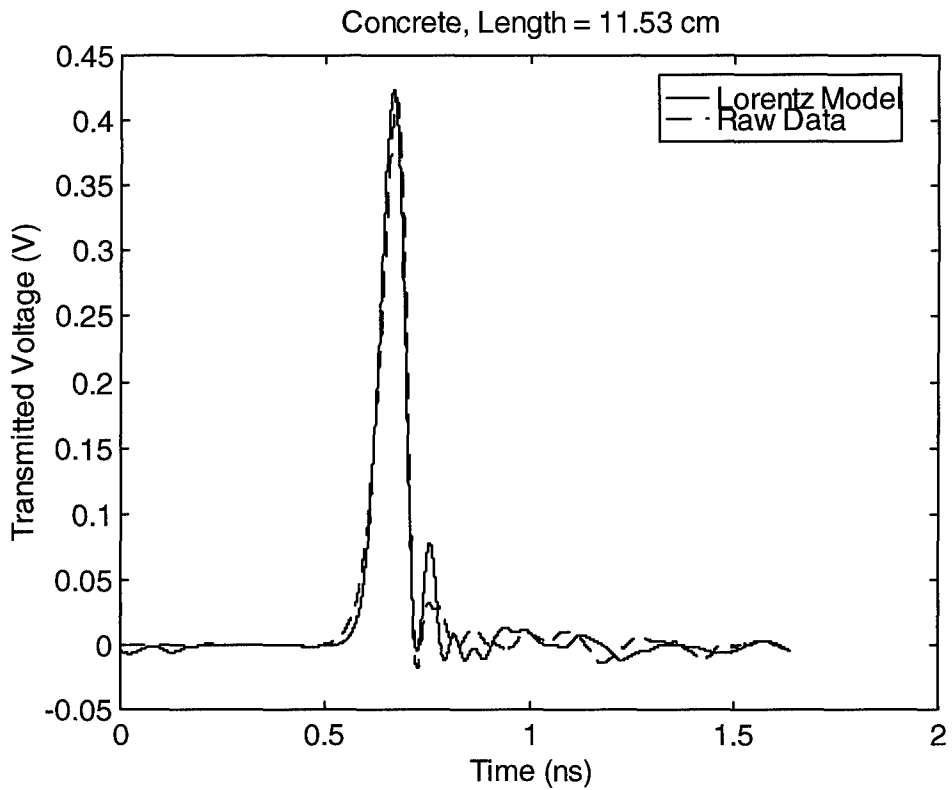


Figure 8.8. Propagation of the impulse through 11.53 cm and 20.27 cm of concrete, raw data and prediction with Lorentz model convolved with the air waveform.

IX. Concrete: Model Validation

Now that we have determined the dielectric constant of concrete, we validate our model by predicting the transmitted voltage for other waveshapes. These predictions are then compared to the raw measured time domain waveforms. Various pulse shapes were produced by using waveshaping modules to tailor the output from the PSPL 4015C pulser, as described in Section VII. A table of the data provided in this section is shown in Table 9.1. In order to predict the voltage transmitted through the concrete, we need only the air waveform and the four Lorentz parameters from the previous section. The method of calculation is described in detail in Section V of this report.

Let us first consider the propagation of a doublet through the air-filled coax, as shown in Figure 9.1. We predict the transmitted voltage through 11.53 cm and 20.27 cm of concrete using our Lorentz parameters from the last section, and the air waveform. The calculations follow the basic method described in Section V. The results are shown in Figure 9.2, and are overlaid with raw data taken for the same case. We find excellent agreement between our predictions and the measurement.

Finally, we repeat the process for a step-function waveform, with concrete lengths of 11.53 cm and 20.27 cm. The air waveform ($\ell = 0$ cm) for the step-function is shown in Figure 9.3, and the predictions and measurements for the voltages transmitted through the samples are shown in Figure 9.4. Note that in order to carry out the convolution on the step-function, we had to first take its derivative, then implement the convolution, and finally integrate the result. Once again, we have found excellent agreement between our predictions and the measurements.

By now, we have justified the Lorentz model of concrete in several different ways. We have also shown that this model allows us to predict the evolution of arbitrary temporal waveshapes as they propagate through concrete. In the section that follows we consider how a selection of canonical Gaussian pulses propagate through concrete when it is described by the Lorentz medium.

Table 9.1. Experimental Data For Transmission Through Concrete In Coax Line Using Various Pulse Shapes.

DOUBLET WAVEFORM		
Sample Length (cm)	Amplitude Pk - Pk (mV)	File #
00.00	95.3	F7010613
11.53	78.9	F7010614
20.27	71.0	F7010615

STEP WAVEFORM			
Sample Length (cm)	Risetime 10% - 90% (ps)	Amplitude 0 - 100 (mV)	File #
00.00	68.2	402	F7010609
11.53	79.1	371	F7010611
20.27	101.3	371	F7010612

(NOTE: Air Length for all data = 100.00 cm - Sample Length.)

(Scope Delay = 84.12 ns for all data.)

(The waveforms shown have an additional portion time-gated out of the beginning of the waveforms. These times are 0, 150, and 410 ps for the lengths of 0, 11.53 and 20.27 cm, respectively.)

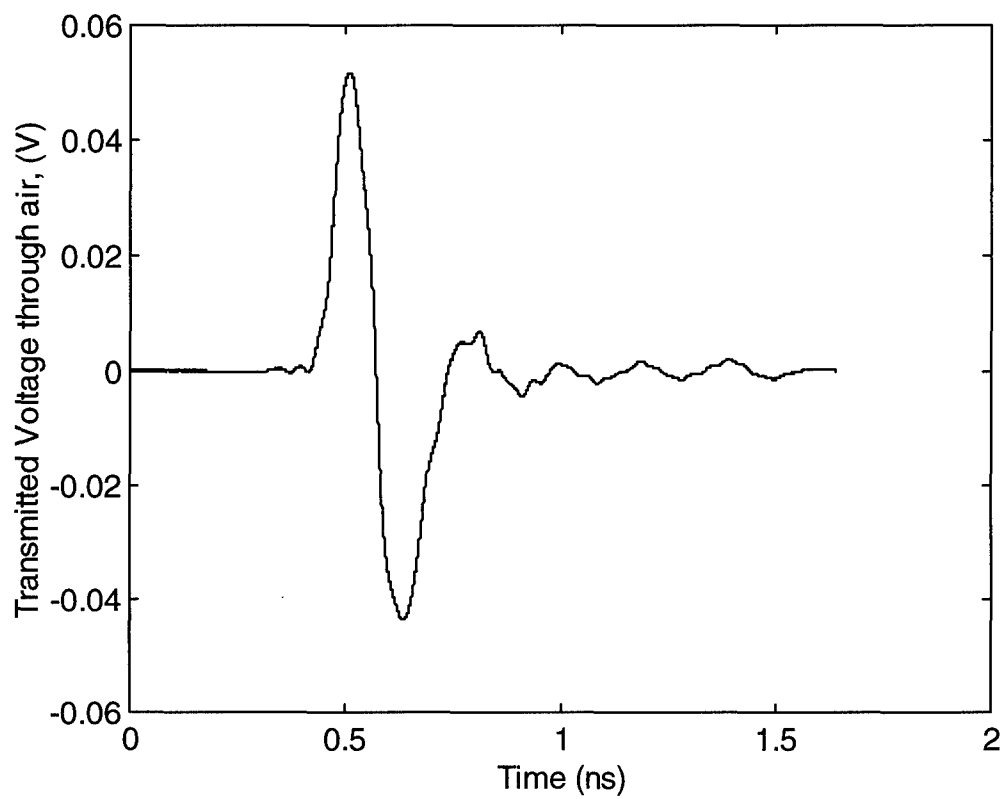


Figure 9.1. Air waveform for the doublet.

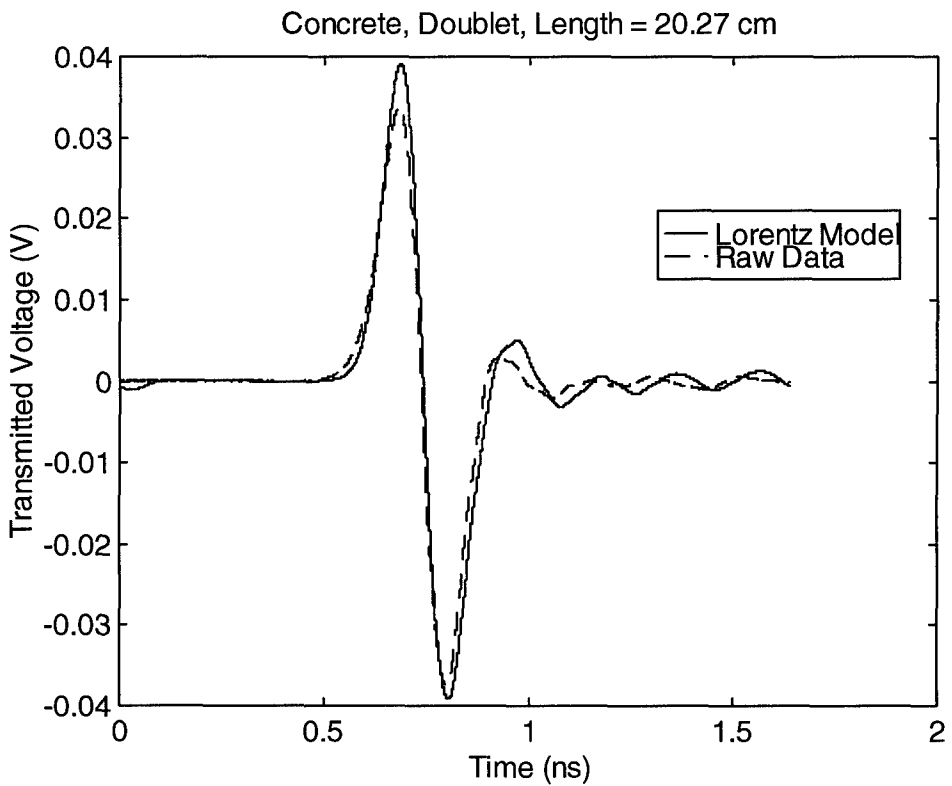
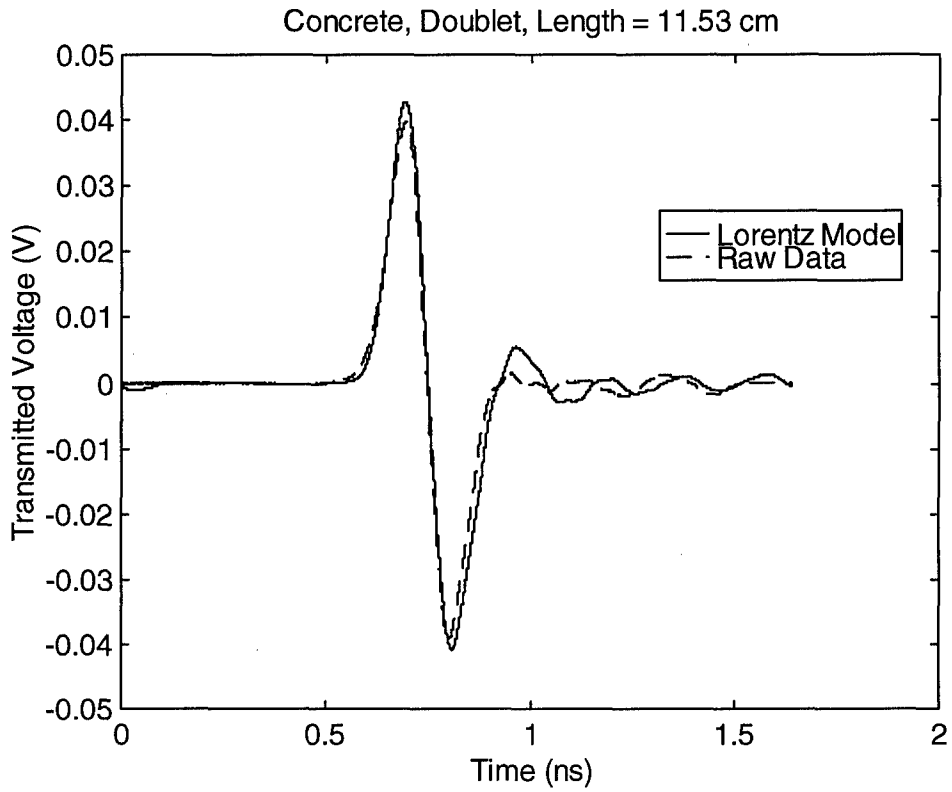


Figure 9.2. Propagation of the doublet through 11.53 cm and 20.27 cm of concrete, raw data and prediction with Lorentz model.

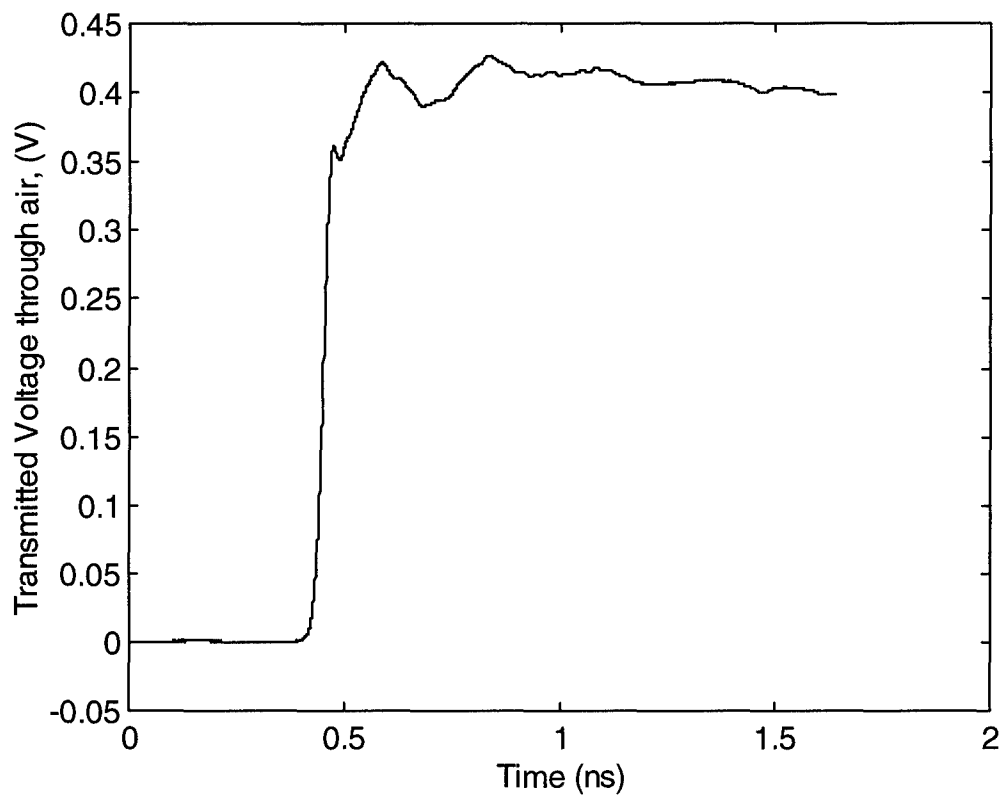


Figure 9.3. Air waveform ($\ell = 0$) for the step-function waveshape.

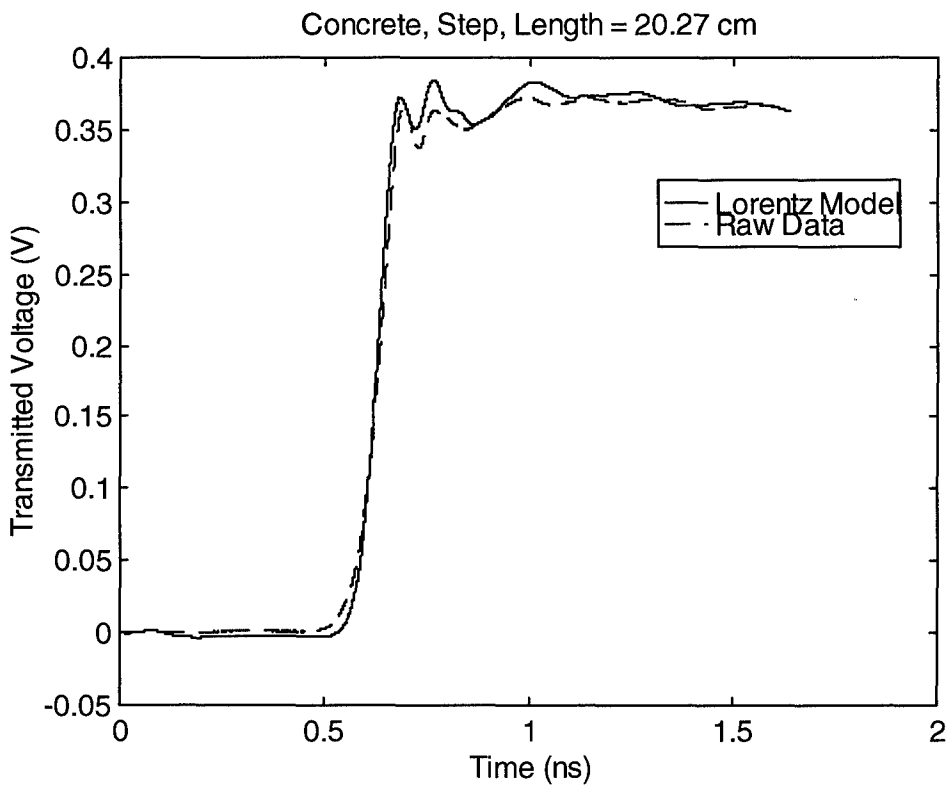
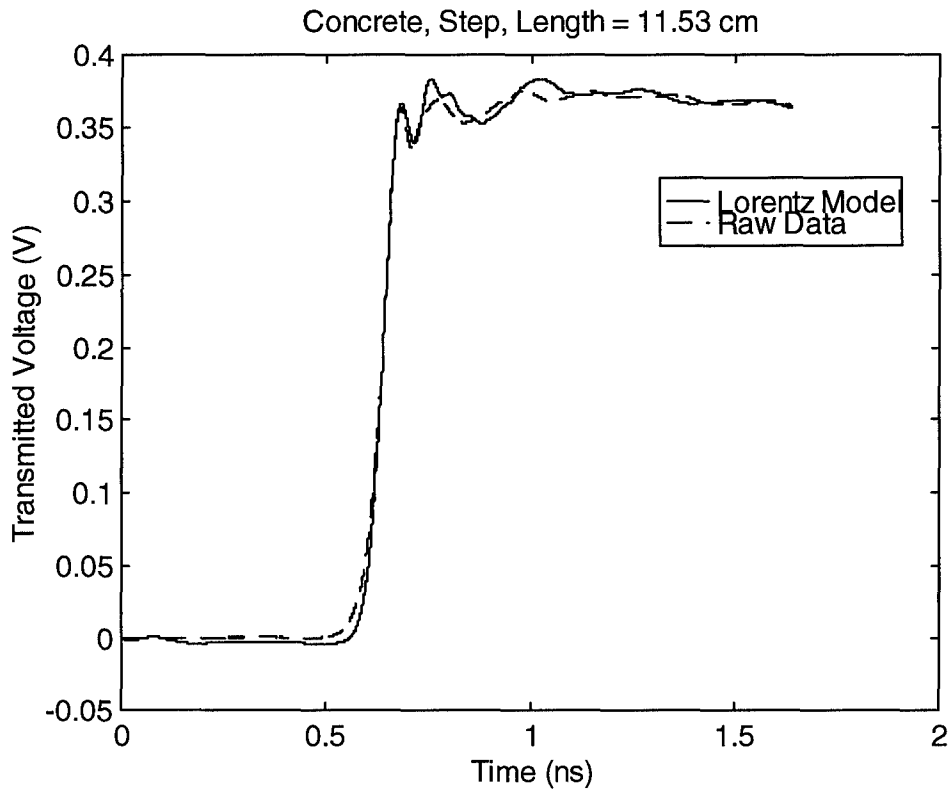


Figure 9.4. Propagation of the step-function through 11.53 cm and 20.27 cm of concrete, raw data and prediction with Lorentz model.

X. Concrete: Propagation Waveshapes and Data Compilation

Having shown the validity of the Lorentz model for our range of frequencies, we now consider how impulses with various pulse widths propagate out to various distances using this model. Thus, we consider FWHM pulse widths of 30, 100, and 300 ps, and propagation distances of 0.1, 1, and 10 meters.

A diagram of the input Gaussian pulses was shown previously in Figure 6.1. The transmitted pulses are shown in Figures 10.1 through 10.3. The time delays of the waveforms have been adjusted arbitrarily to enhance clarity. From these graphs, we can clearly see the attenuation and pulse spreading of the waveform as they propagate.

Next, we compile the data in Figures 10.1-10.3, by plotting various waveform characteristics on log-log scales. This is a useful representation for system studies. First, we plot the peak magnitude for the three waveforms, at various distances (Figure 10.4). Next, we plot the FWHM of the waveforms, normalized to the FWHM of the input Gaussian (Figure 10.5). Finally, we plot the energy density of the waveforms (Figure 10.6), and the energy density normalized to the energy density of the input waveform (Figure 10.7). The energy density of a waveform is calculated as shown previously in Section VI.

As we expect, the magnitude decreases and the FWHM increases with propagation distance. As shown previously for sand, the 30 ps pulse loses only a factor of ten (10 dB) in energy, after propagating 10 meters. This may be a tolerable loss in an actual impulse radar system. Note that this prediction is based on the Lorentz model of Section VIII, which may underpredict low-frequency attenuation.

30 ps Waveform After Propagating Various Distances Through Concrete

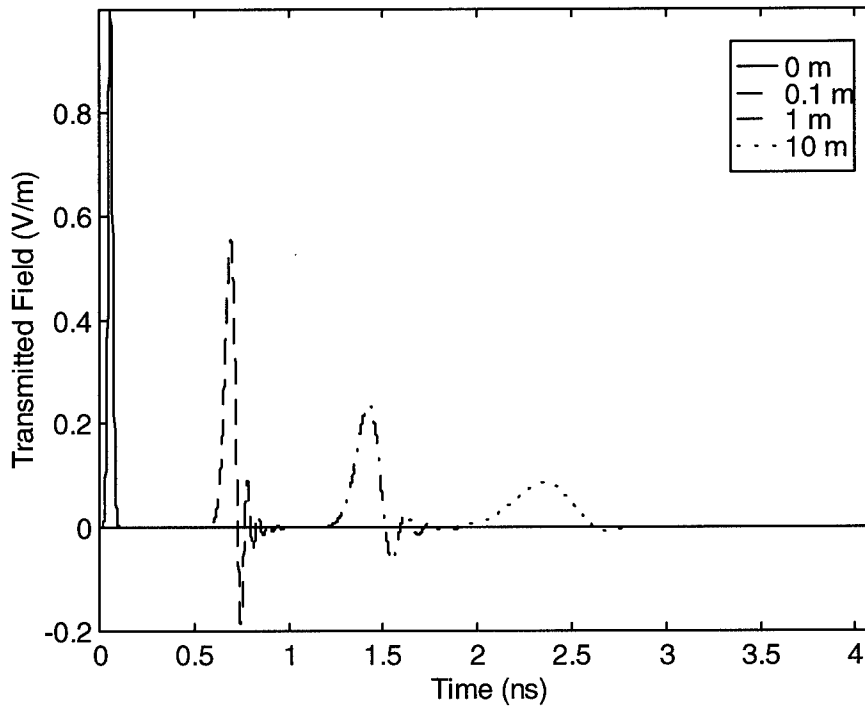


Figure 10.1. The propagated field of the 30 ps pulse at 0, 0.1, 1, and 10 meters. (Starting times shifted for clarity.)

100 ps Waveform After Propagating Various Distances Through Concrete

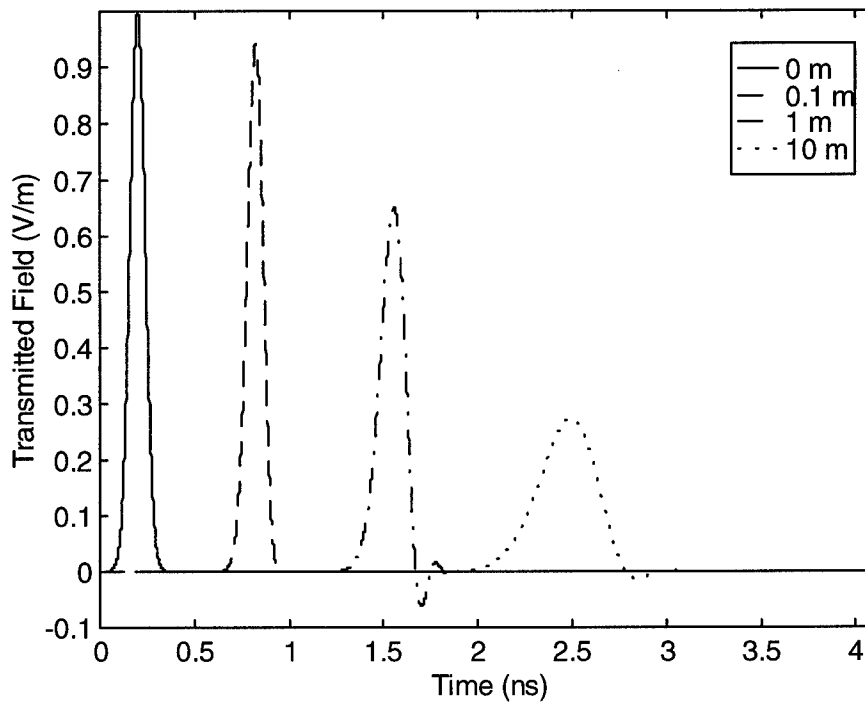


Figure 10.2. The propagated field of the 100 ps pulse at 0, 0.1, 1, and 10 meters. (Starting times shifted for clarity.)

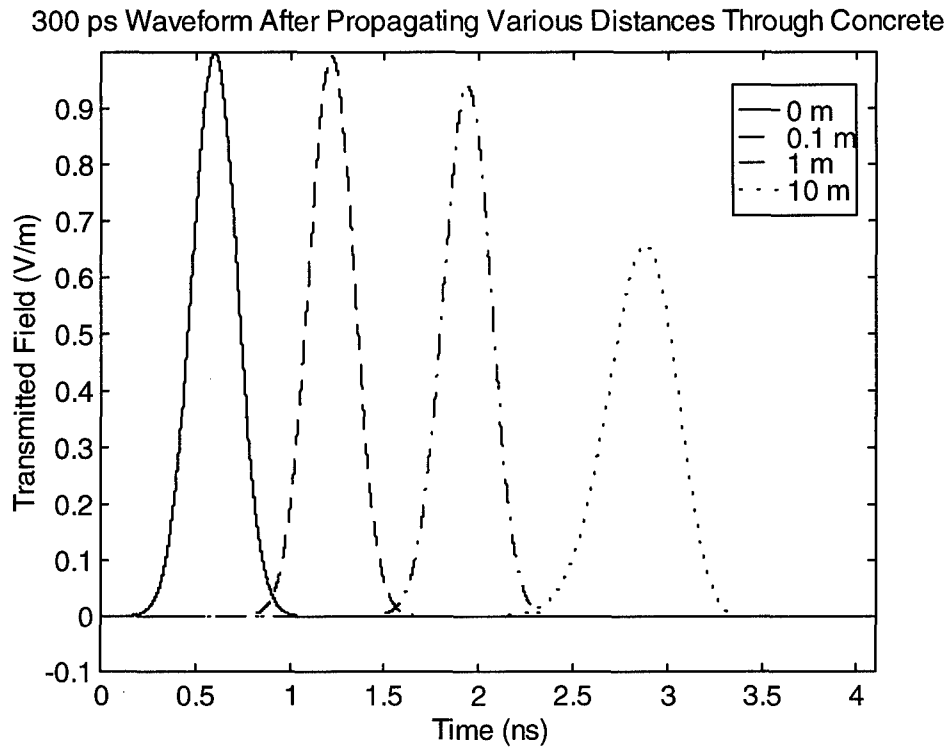


Figure 10.3. The propagated field of the 300 ps pulse at 0, 0.1, 1, and 10 meters. (Starting times shifted for clarity.)

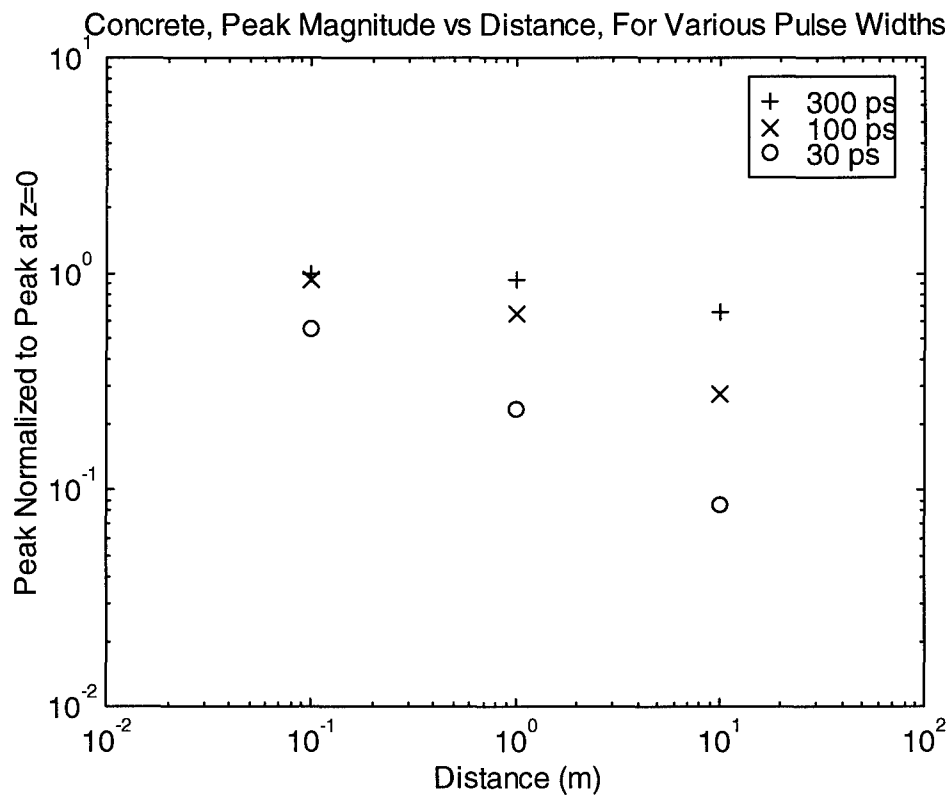


Figure 10.4. Peak waveform magnitude as a function of FWHM and propagation distance.

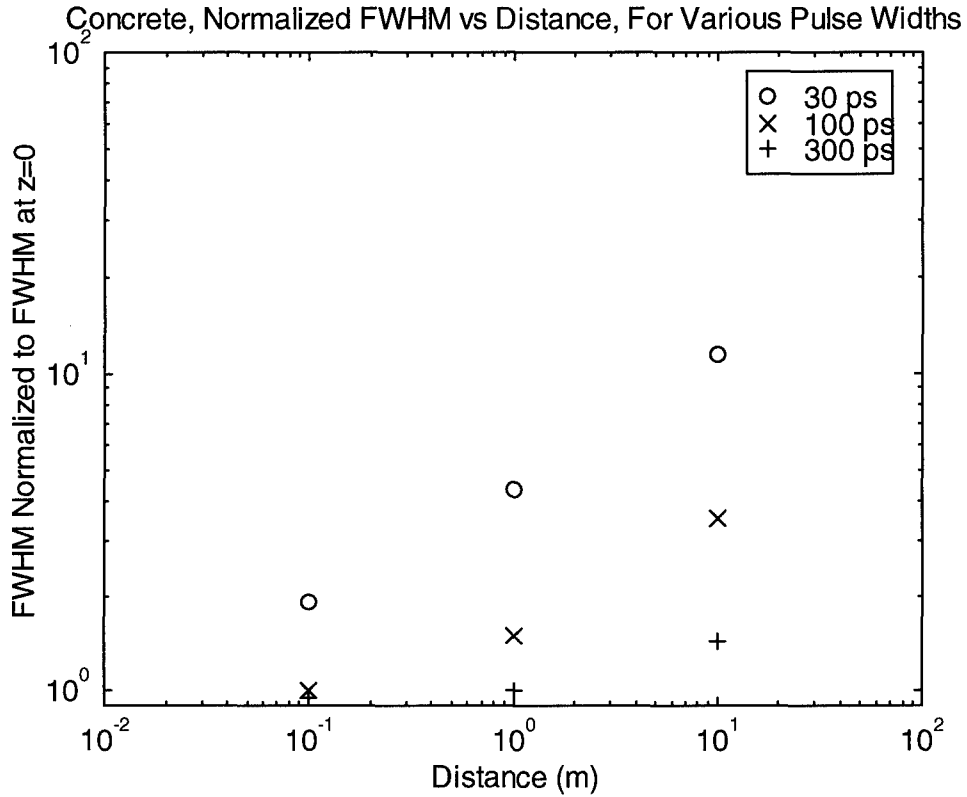


Figure 10.5. Normalized FWHM as a function of input FWHM and propagation distance.

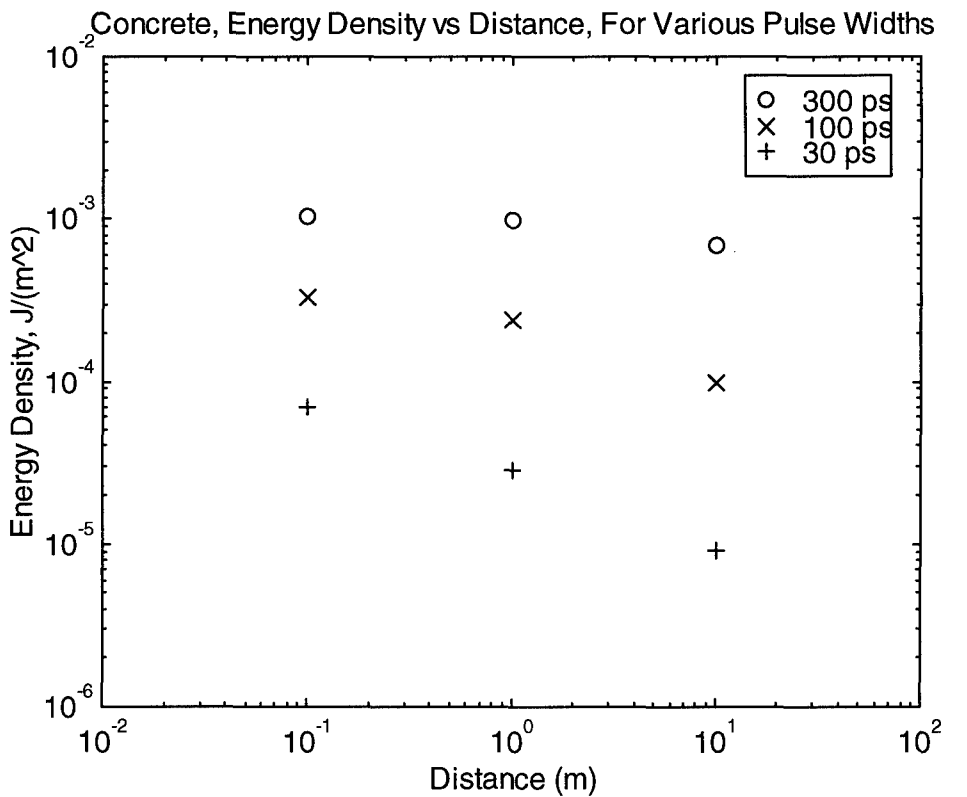


Figure 10.6. Energy density as a function of input FWHM and propagation distance.

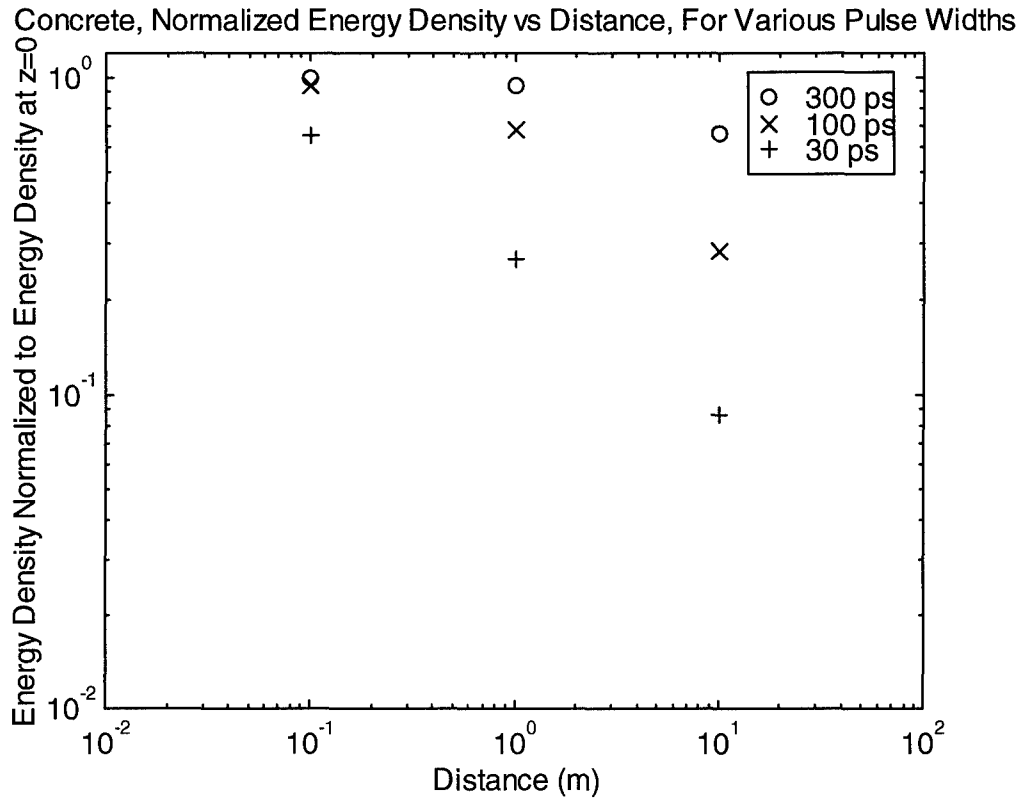


Figure 10.7. Normalized Energy density as a function of input FWHM and propagation distance.

XI. Moist Sand: Measurements

Experiments were performed to determine dielectric properties of moist sand for propagation of ultra-wideband impulses. The measurements were performed in the TEM mode coaxial transmission apparatus which has been previously described in [1]. The electronics system configuration and measurement setup was identical to that previously described for concrete measurements in Section VII of this report. The electronic setup was shown in Figure 7.1. Measurements were taken for narrow impulse propagation through three different lengths of moist sand in the coax line for two different moisture contents -- 1.58% and 3.23% distilled water by weight. Table 11.1 summarizes the measurement results.

The sand samples used for the experiments were from the same batch which was previously used for the dry sand measurements, and sample preparation was similar. This sand was obtained from the Eglin AFB sandbox facility. The sand was first sifted and oven dried at 300°F for 4 hours to drive off all water. The sand samples were then weighed to an accuracy of 0.05 grams with a digital scale. A precise (accurate to 0.05 ml) quantity of distilled water was added to each sample using a Moore's pipette, and the samples of sand and water were thoroughly mixed by stirring for 30 minutes. Two sand samples were prepared with a moisture content of $1.58 \pm 0.03\%$ and $3.23 \pm 0.03\%$ by weight. The dielectric properties of the distilled water were described in [1].

A procedure for repeatably filling the coax line apparatus with sand with loose (uncompacted) sand was developed. It was essential that the sand sample have a planar horizontal interface and uniform density. The required uniformity was achieved using a specially designed filling fixture. The sand expanded slightly upon addition of water, giving a decrease in density. The measured density was $1.39 \pm 0.06 \text{ g/cm}^2$ for the 1.58% sample and $1.31 \pm 0.05 \text{ g/cm}^2$ for the 3.23% sample. The uncertainty in density is due to variations in sample compaction. The mean values quoted are the average of 4 measurements.

Measurements were taken with three different sample lengths for two different moisture levels. In each case the length of material in the coax line was calculated from the measured sample weight and density. The material dielectric response to the impulse waveshape is shown in Figures 11.1 and 11.2. A reference waveform ($L = 0 \text{ cm}$) was taken with only air in the coaxial fixture. Then the material was added, and data waveforms were recorded for each propagation distance. It must be noted that as material is inserted into the coaxial line, the length of the air path is reduced by the sample length. This reduction of air path must be considered in data analysis.

Table 11.1 lists raw data and waveform file names for the narrow impulse propagating through moist sand for 1.58% and 3.23% moisture content. The pulse width, amplitude, and propagation delay were read directly from the digitizer using the measurement mode. The pulse width refers to the FWHM and the amplitude to the 0% to 100% amplitude calculation with the built-in IEEE algorithm. The raw data shows that the pulsewidth broadens and that the amplitude decreases as the propagation distance increases. This effect can be seen graphically in

Figure 11.1 (top) which shows an overlay of the transmitted impulse for 4 propagation distances with 1.58% moisture. Figure 11.2 shows similar data for 3.23% moisture.

The pulse is shifted to a later time as the length of material is increased. The time increment is almost identical for each sample. The approximate index of refraction, $n = c/v$, can be calculated from this data using the formula

$$n = \frac{c \Delta t}{\Delta L} + 1 \quad (11.1)$$

where Δt and ΔL are the differential time and length computed from any pair of waveforms. The times are measured to 10% of peak amplitude rather than 50% in order to minimize the effect of the finite pulse risetime. Comparison of any pair of waveforms gives an index of approximately 1.6 for 1.58% moisture and 1.7 for 3.23% moisture. The dielectric constant, which is the square of the index ($\epsilon = n^2$), is 2.6 and 3.0 respectively for 1.58% and 3.23% moisture. This is an approximate calculation because we are calculating the group velocity for the impulse and the calculation ignores the frequency dependent propagation speed.

Table 11.1. EXPERIMENTAL DATA FOR NARROW IMPULSE TRANSMISSION THROUGH MOIST SAND.

MOIST SAND (1.58% H₂O by Weight)				
Sample Length (cm)	Pulsewidth FWHM (ps)	Amplitude (mV)	Propagation Delay (ps)	File #
00.0	43	672	0	F7022002
13.5	88	351	248	F7022003
27.0	109	282	508	F7022004
40.4	132	228	782	F7022005

MOIST SAND (3.23% H₂O by Weight)				
Sample Length (cm)	Pulsewidth FWHM (ps)	Amplitude (mV)	Propagation Delay (ps)	File #
00.0	43	681	0	F7022101
14.1	128	249	278	F7022102
28.2	147	201	613	F7022103
42.2	179	159	957	F7022104

(NOTE: Air Length for all data = 100.00 cm - Sample Length.)
Scope Delay = 84.02 ns for all data.

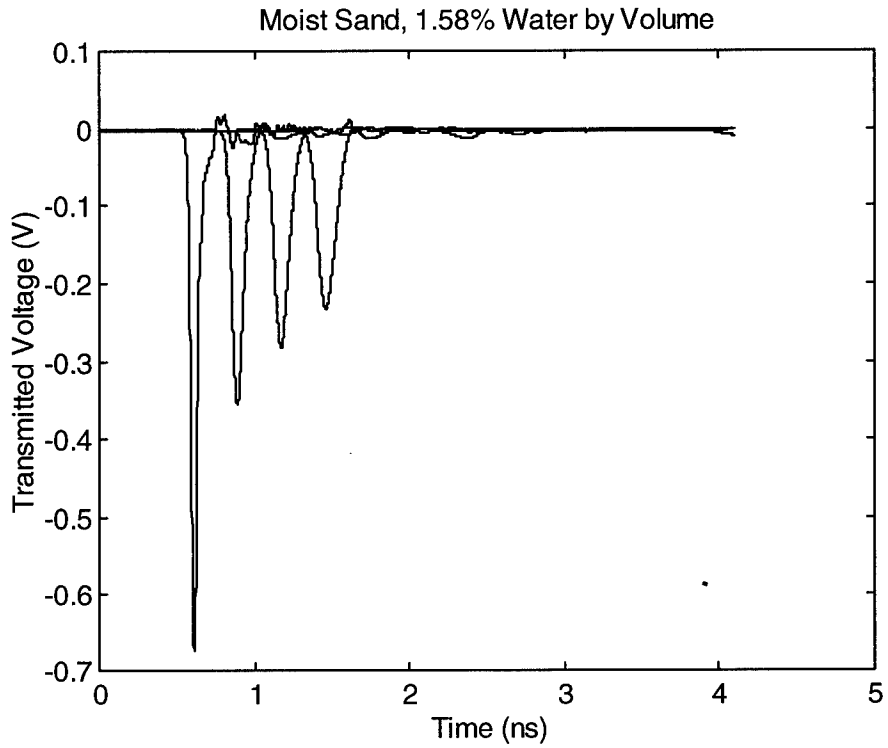


Figure 11.1. Impulse propagation through moist sand (1.58%), lengths 0, 13.5, 27.0 and 40.4 cm.

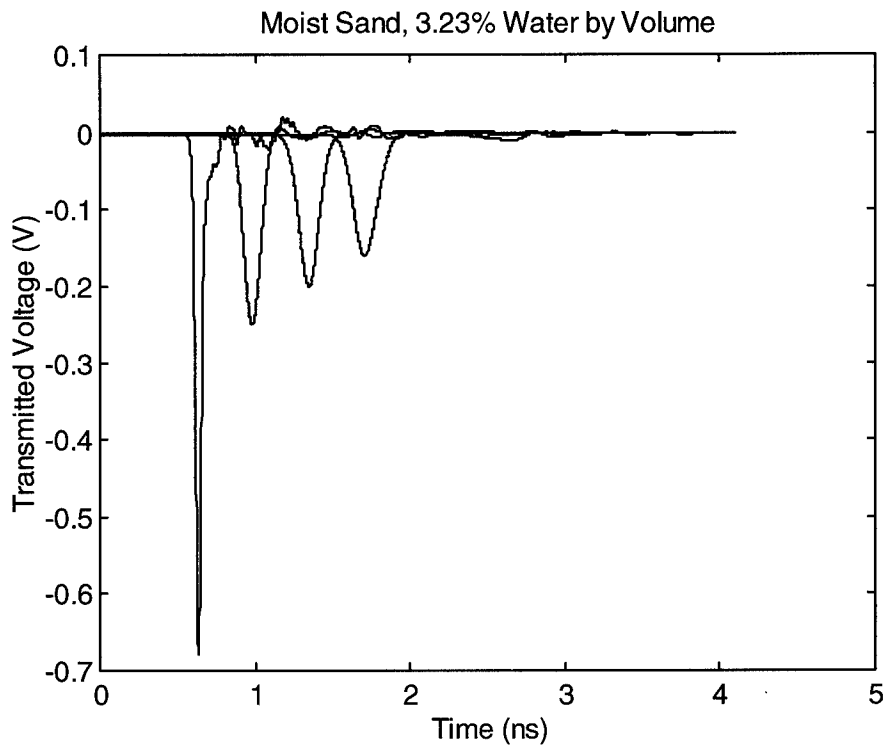


Figure 11.2. Impulse propagation through moist sand (3.23%), lengths 0, 14.1, 28.2 and 42.2 cm.

XII. Moist Sand: Data Processing and Fit to Dielectric Constant Model

We provide here a complete set of data for moist sand, with 1.58% and 3.23% concentrations of water by weight, as described in the previous section. This data is very similar to that provided earlier for distilled water in [1] and for dry sand and concrete as described earlier in this report. The measurement technique is the same, and the processing is almost exactly the same, with minor exceptions, as noted below. The raw waveforms for all the data were shown in the previous section. Details relating to the data were shown previously in Table 11.1.

First, we process the data on moist sand with 1.53% water. In Figure 12.1, we show the transmitted voltage through 13.5 cm and 40.4 cm of moist sand. This is the raw data upon which the dielectric constant calculation is based. The ratio of these two waveforms in the frequency domain represents the impulse response for the difference of the two lengths, or 26.9 cm. The ratio was taken by limiting the smallest value of the denominator to 1% of its peak in the frequency domain, and by applying a 5th-order modified Butterworth filter at 12 GHz. The resulting ratio is shown in Figure 12.2, and the corresponding time domain impulse response and its integral are shown in Figure 12.3.

With the above data, we can now calculate the dielectric constant, using the techniques of [1]. The real and imaginary parts of the dielectric constant are shown in Figure 12.4. The corresponding attenuation is shown in Figure 12.5. Note that although these curves were generated from a single pair of waveforms, similar results were obtained with other waveform pairs, so our results are self-consistent.

A Debye model fit was generated for the above dielectric constant data. Unlike earlier model fits, we included a conductivity term in the model, as derived in Section II. This was necessary in order to model accurately the low-frequency behavior of the imaginary part of the dielectric constant. Without the conductivity term, the Debye model forces the imaginary part of the dielectric constant to zero at zero frequency, and that is clearly not the case in this data. Thus, the complex dielectric constant is expressed as

$$\epsilon_r = \frac{\sigma}{j\omega\epsilon_0} + \epsilon_\infty + \frac{\epsilon_s - \epsilon_\infty}{1 + j\omega t_0} \quad (12.1)$$

where ϵ_∞ is the relative dielectric constant at high frequencies, ϵ_s is the relative dielectric constant at low (static) frequencies, t_0 is a relaxation time, ϵ_0 is the dielectric constant of free space, and σ is the conductivity. This Debye model with conductivity was implemented using a least mean square fit to the dielectric constant data between 0.6 and 6 GHz. A plot of the resulting Debye model fit is shown in Figure 12.4, and the corresponding calculated attenuation is shown in Figure 12.5. A table of our fitted values for these parameters is shown in Table 12.1. The fit to the imaginary part of the dielectric constant is quite good at low frequencies, due to the inclusion of conductivity in the model.

Next, we convolve the Debye model with the air waveform, to predict pulse shapes for various propagation distances. We do this as a check on whether we have successfully modeled the measured waveforms in Figure 12.1, which were used to generate the model. The results for propagation through 13.5 cm and 40.4 cm of moist sand are shown in Figure 12.6, and are compared to the raw data. We see that there is quite good agreement between the model predictions and the actual measurements.

Table 12.1. Debye Model Parameters for Moist Sand

Debye Parameter	Moist Sand, 1.58%	Moist Sand, 3.23%
ϵ_s	2.6825	3.1778
ϵ_∞	2.1413	2.6181
t_o (ps)	5.5 ps	11.3
σ (mho/m)	1.3828×10^{-3}	2.8577×10^{-3}

Finally, we repeat the entire process for sand with 3.23% moisture. The raw data is shown in Figure 12.7, and the frequency domain ratio is shown in Figure 12.8. To obtain the ratio, a 5th order modified Butterworth filter was applied at 7 GHz. This ratio was converted to the time domain, as shown in Figure 12.9, and integrated, also shown in Figure 12.9. The resulting complex dielectric constant is shown in Figure 12.10, and the attenuation is shown in Figure 12.11. A Debye model with conductivity was fit to the dielectric constant data between 0.5 and 5.0 GHz, and the resulting fit is also shown in Figures 12.10 and 12.11. The Debye parameters are shown in Table 12.1. Finally, we perform a check on the data by convolving the Debye model with the air waveform, and comparing the results to the raw waveforms. The results are shown in Figure 12.12, where we see excellent agreement between the two waveforms for two lengths of sample.

We may summarize the results of this section by noting that the inclusion of the conductivity term improves the fit of the model to the measured data. Without the conductivity term, the imaginary part of the dielectric constant (proportional to the attenuation) is impossible to fit at the lower frequencies.

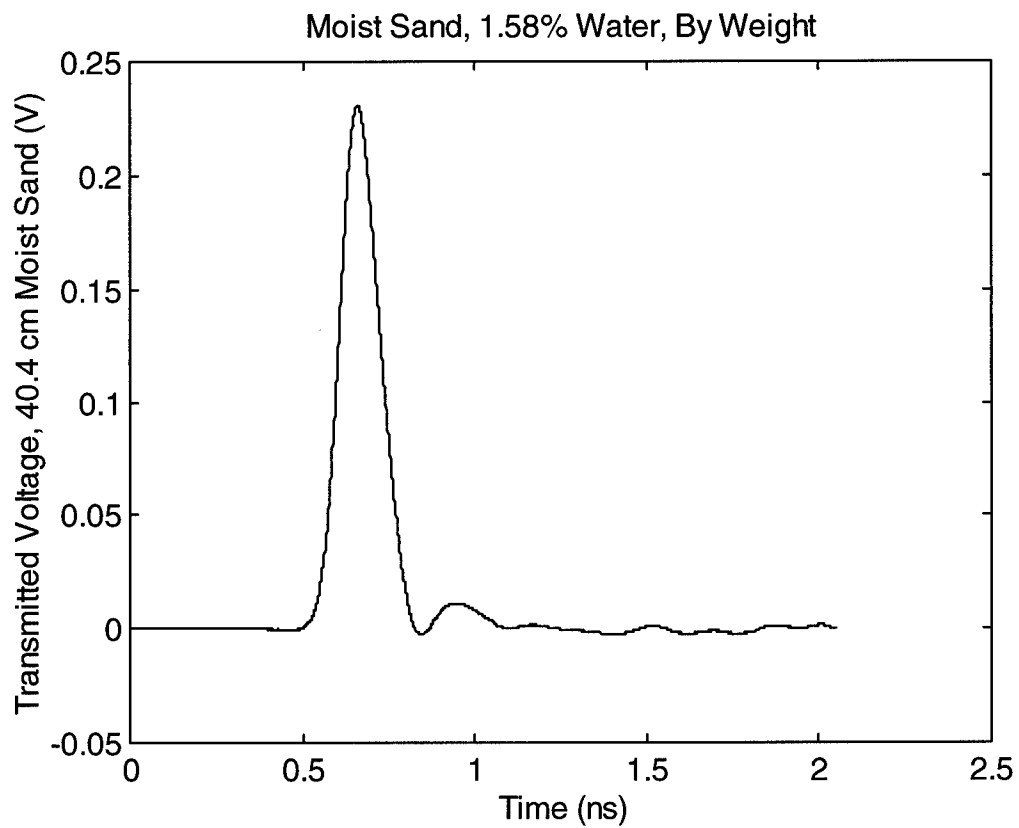
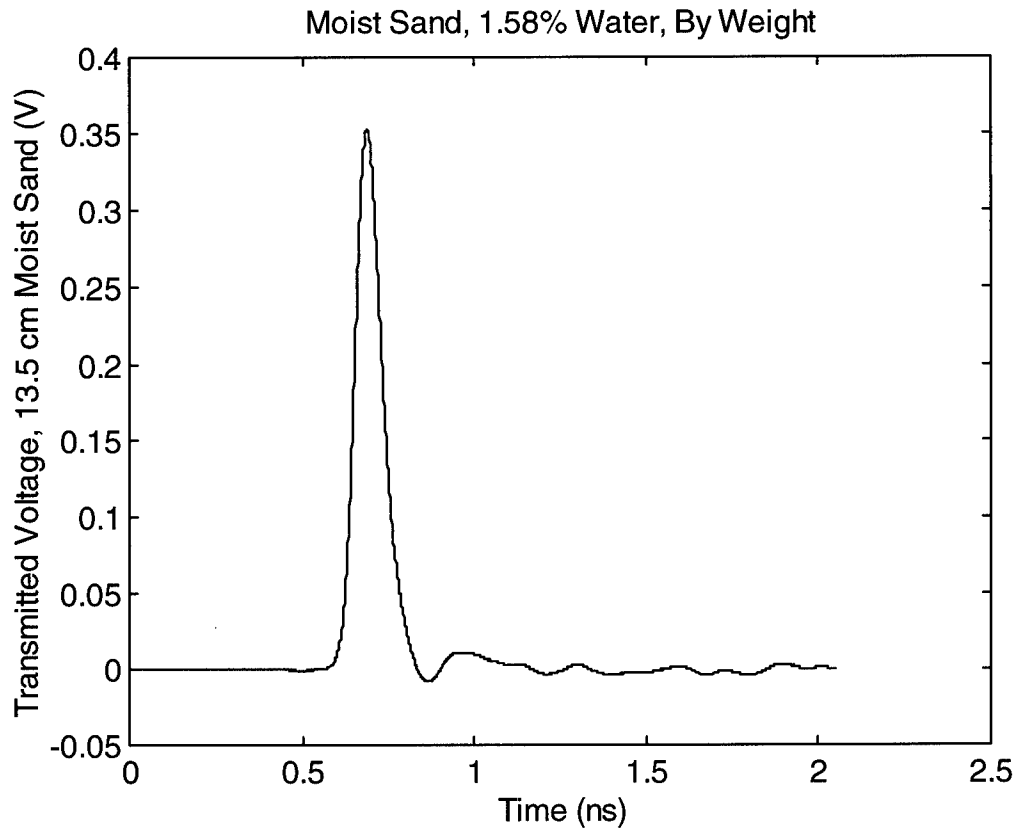


Figure 12.1. Transmitted signals through 13.5 cm and 40.4 cm of moist sand, 1.58%.

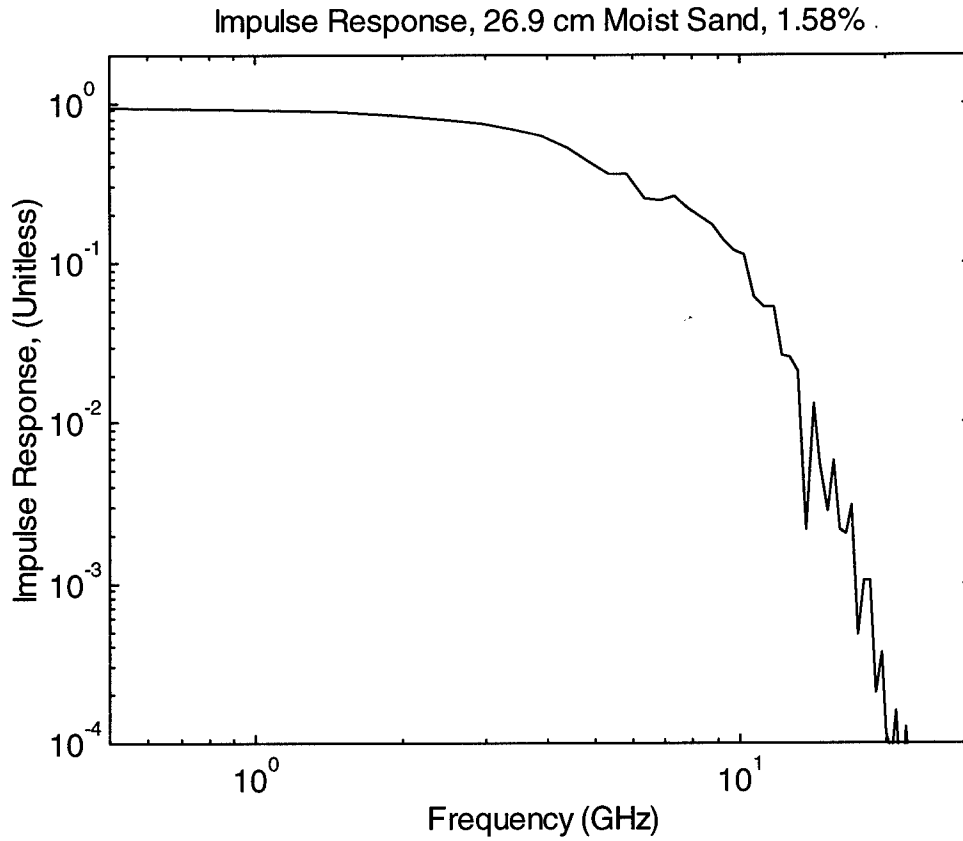


Figure 12.2. The impulse response of 26.9 cm of moist sand, 1.58%.

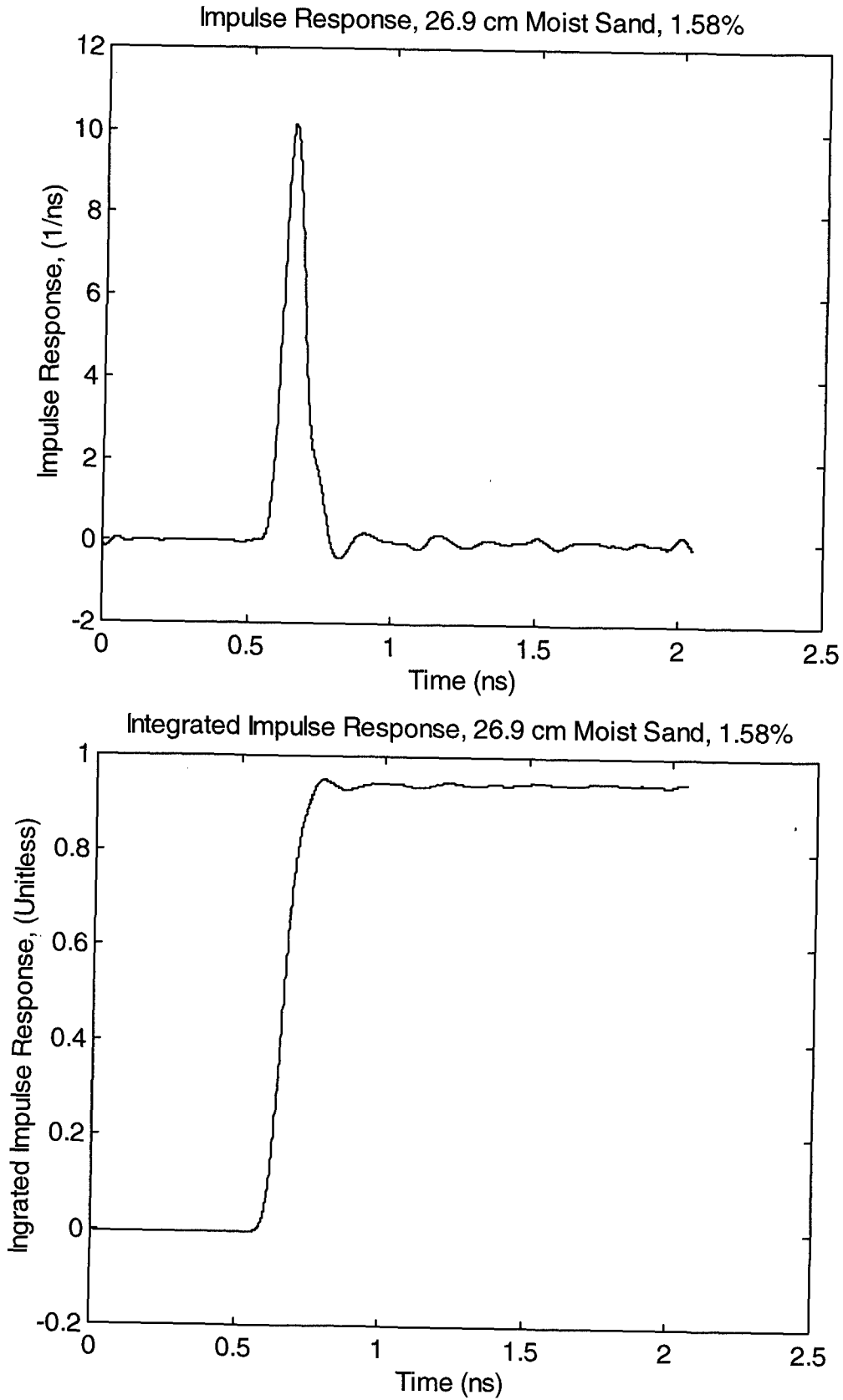


Figure 12.3. The impulse response (top) and its integral (bottom) of 26.9 cm moist sand, 1.58%.

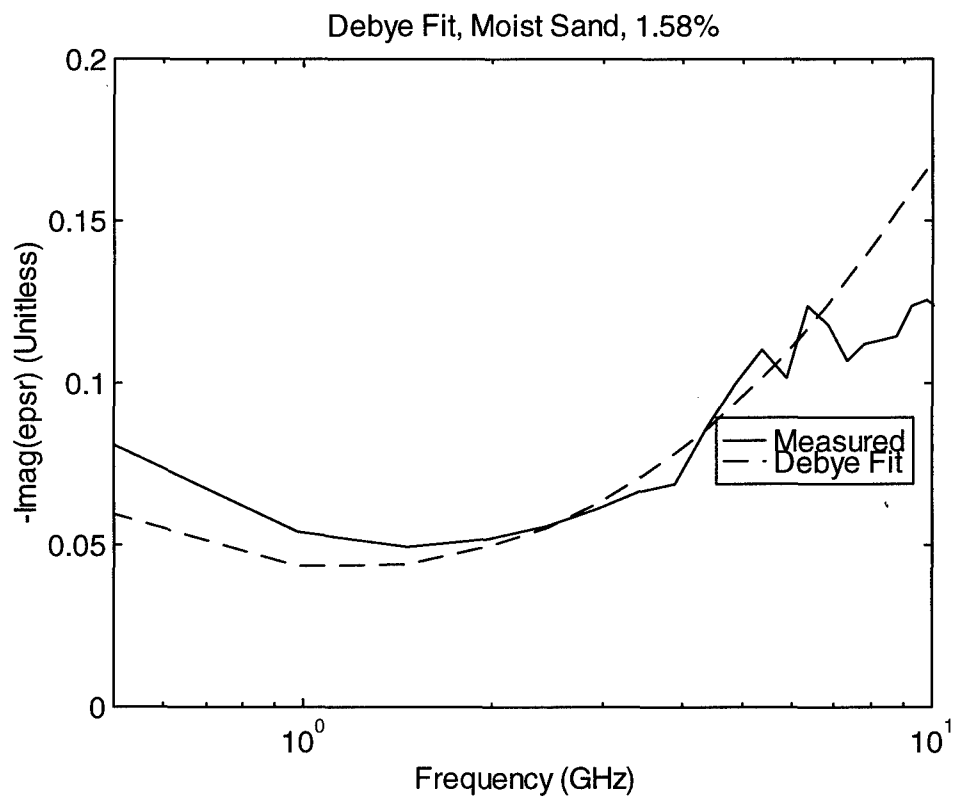
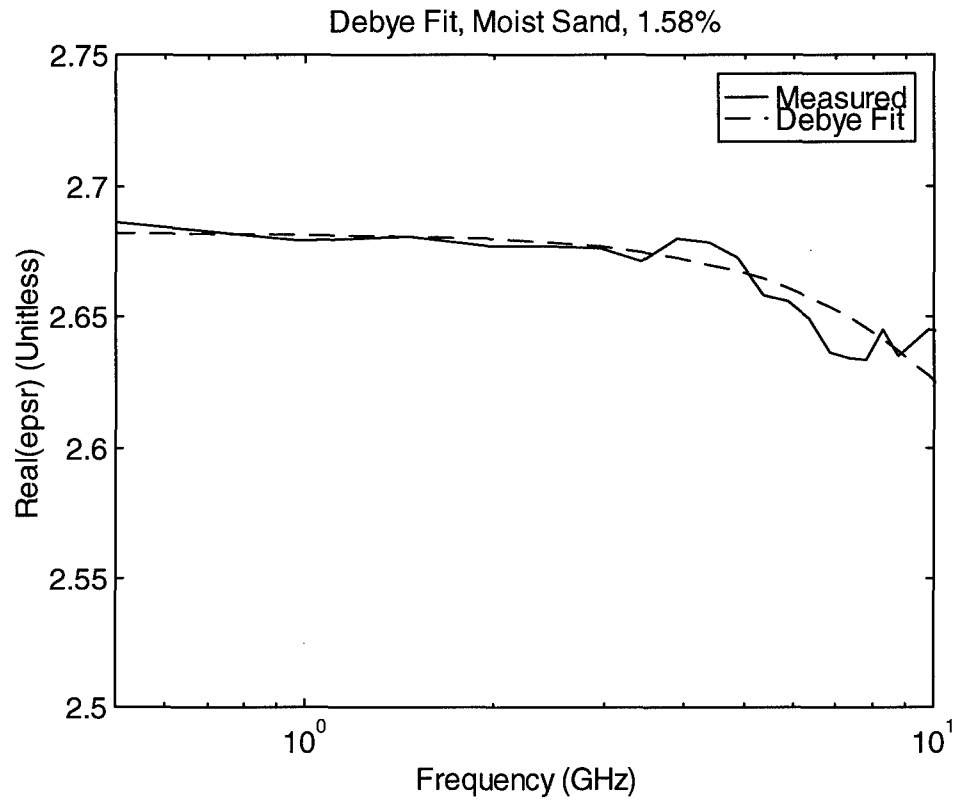


Figure 12.4. Measured dielectric constant of moist sand 1.58%, and the Debye model fit, including conductivity, real and imaginary parts.

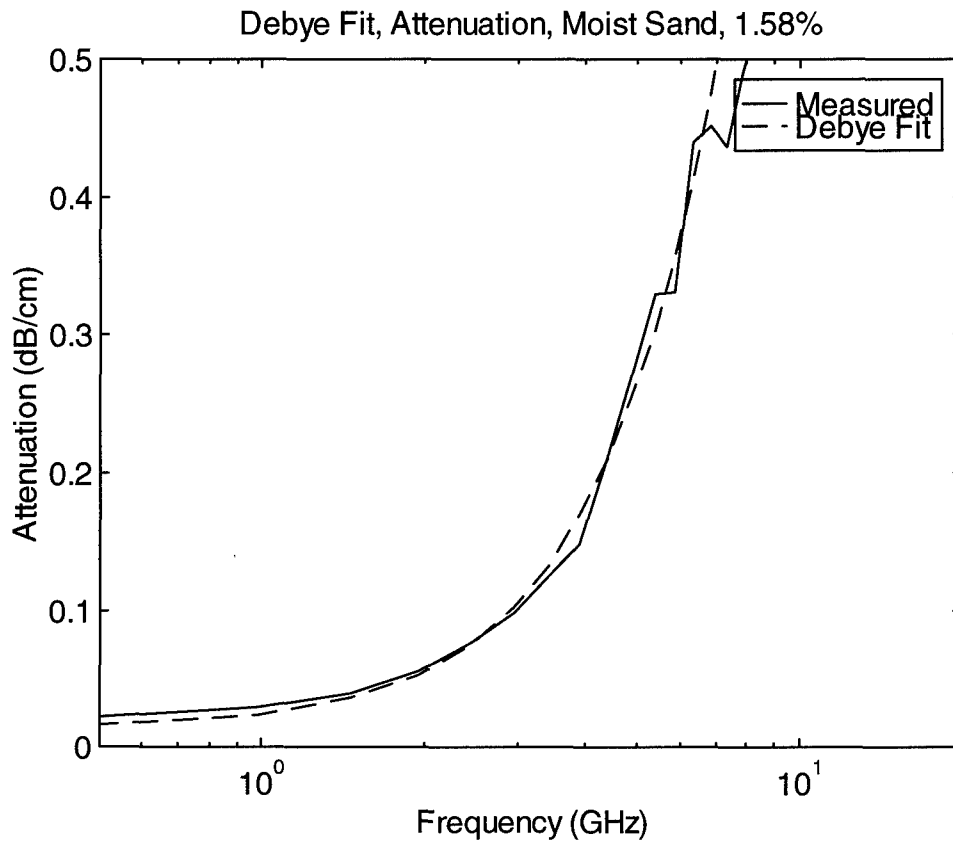


Figure 12.5. Attenuation constant of moist sand 1.58%, measured and Debye model fit, including conductivity.

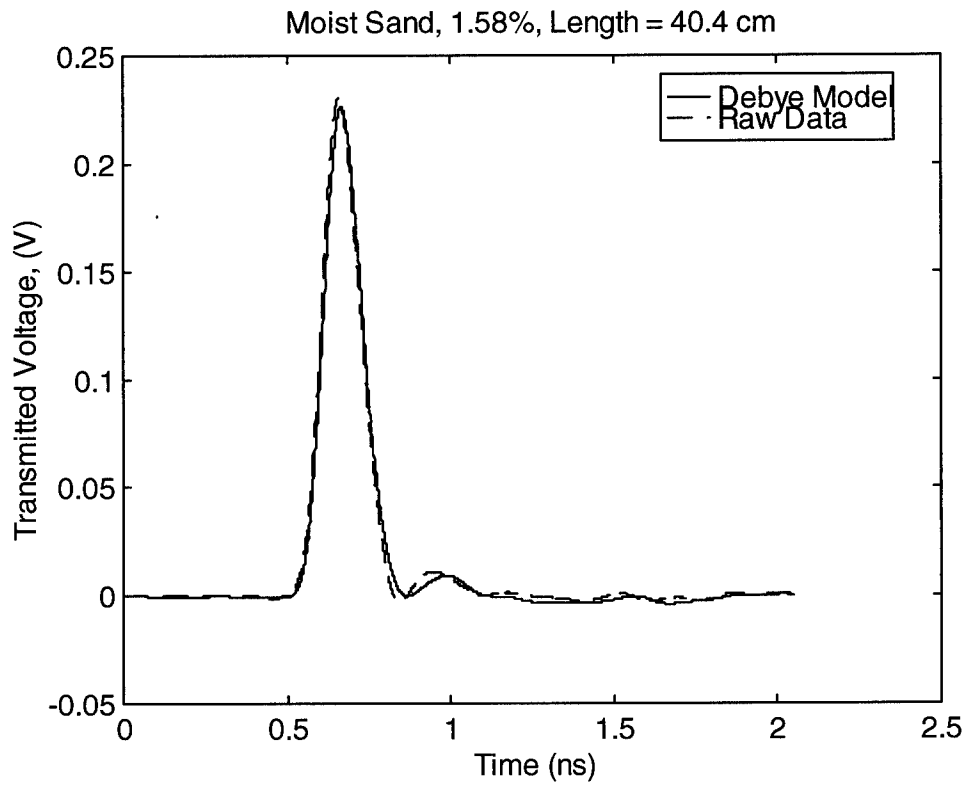
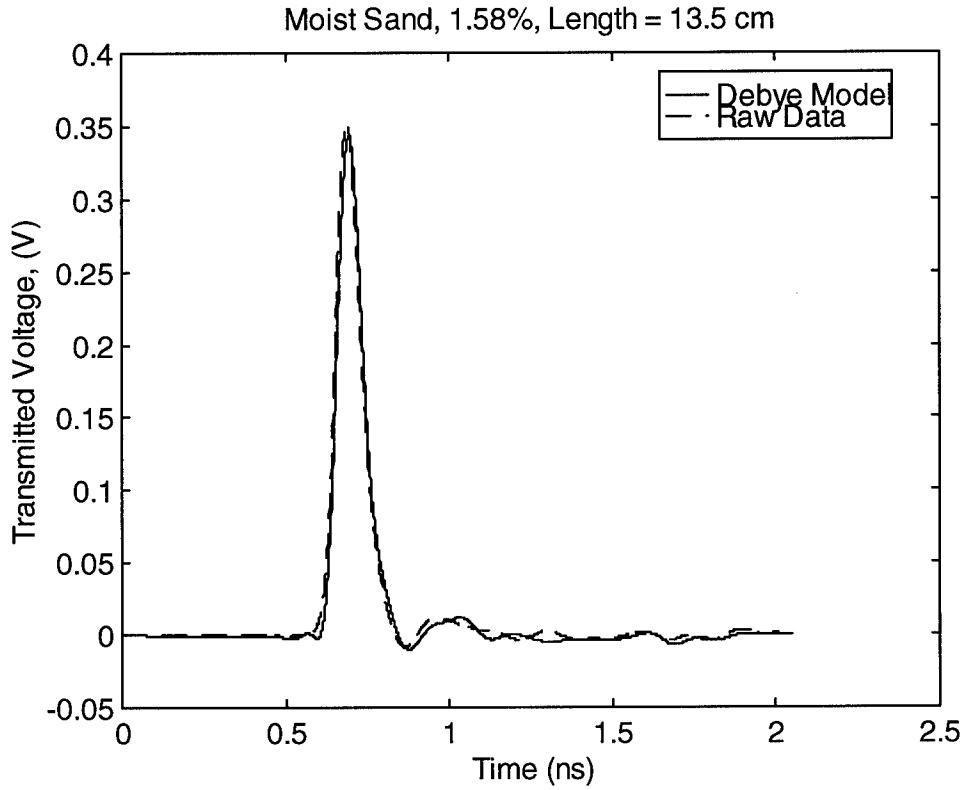


Figure 12.6. Propagation of the impulse through 13.5 cm and 40.4 cm of moist sand 1.53%, raw data and prediction with Debye model convolved with the air waveform.

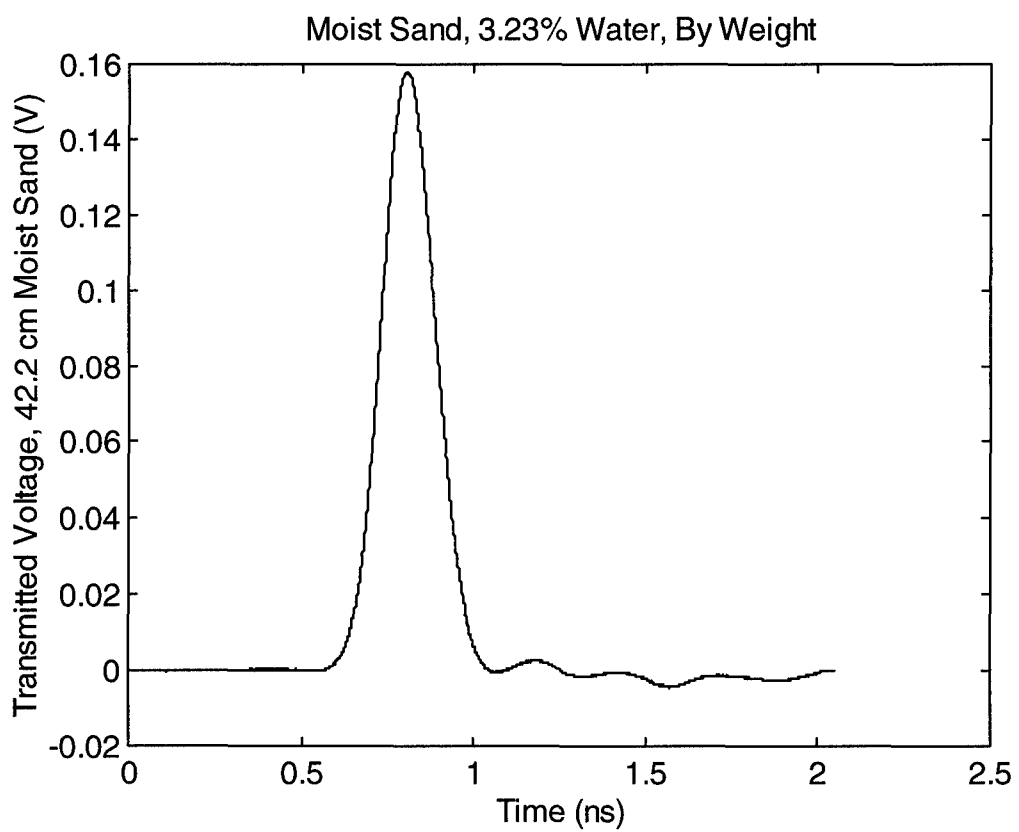
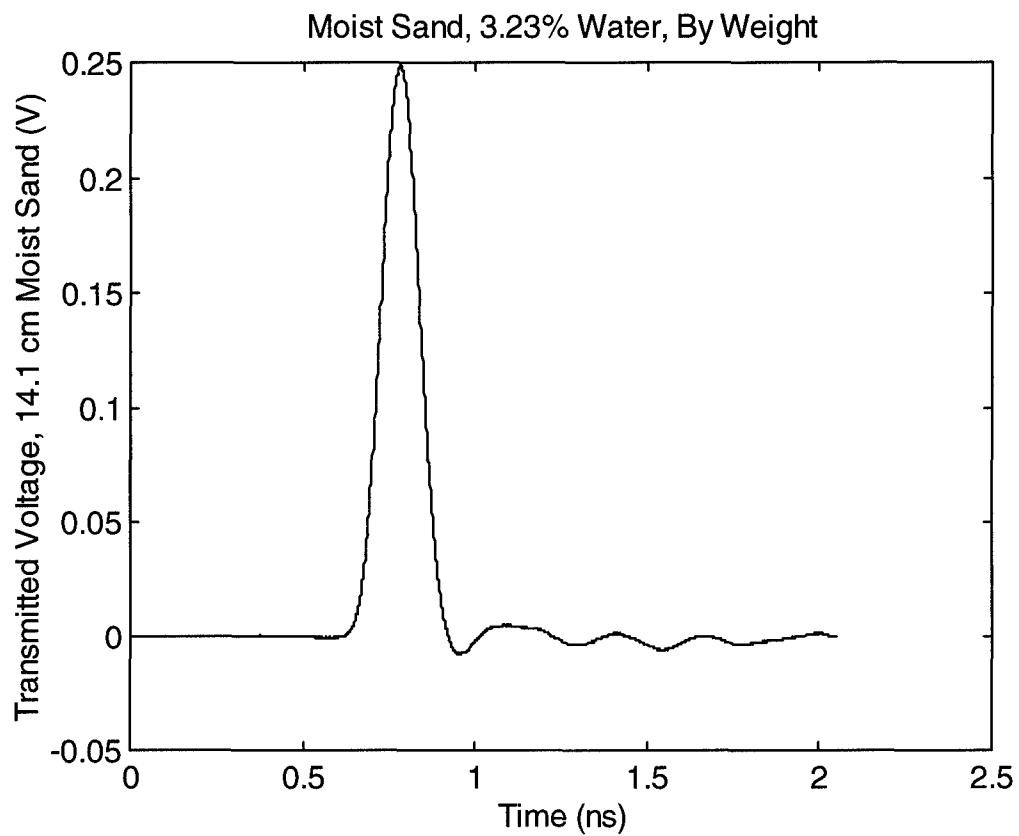


Figure 12.7. Transmitted signals through 14.1 cm and 42.2 cm of moist sand, 3.23%.

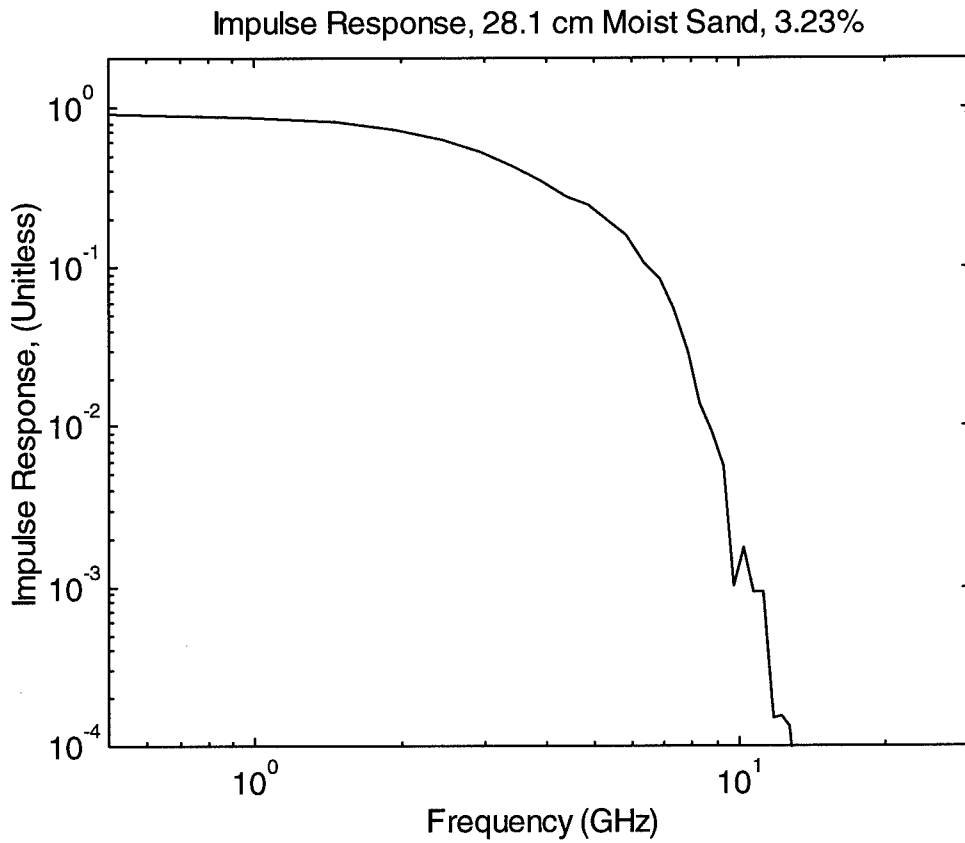


Figure 12.8. The impulse response of 28.1 cm of moist sand, 3.23%.

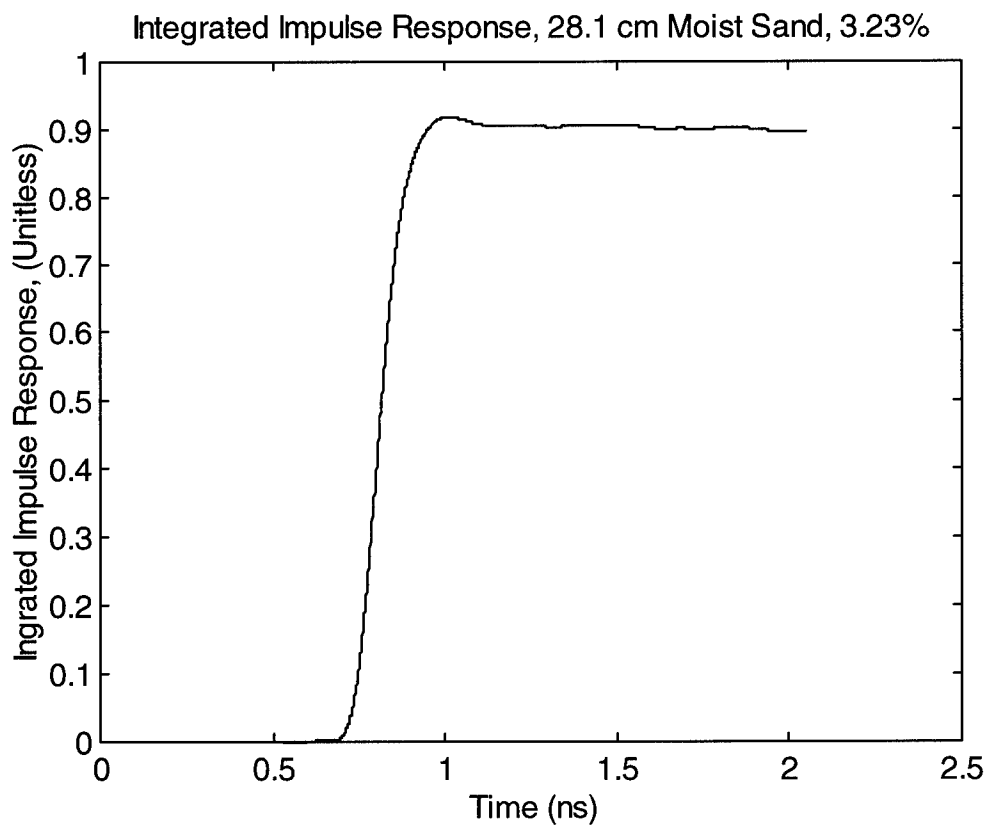
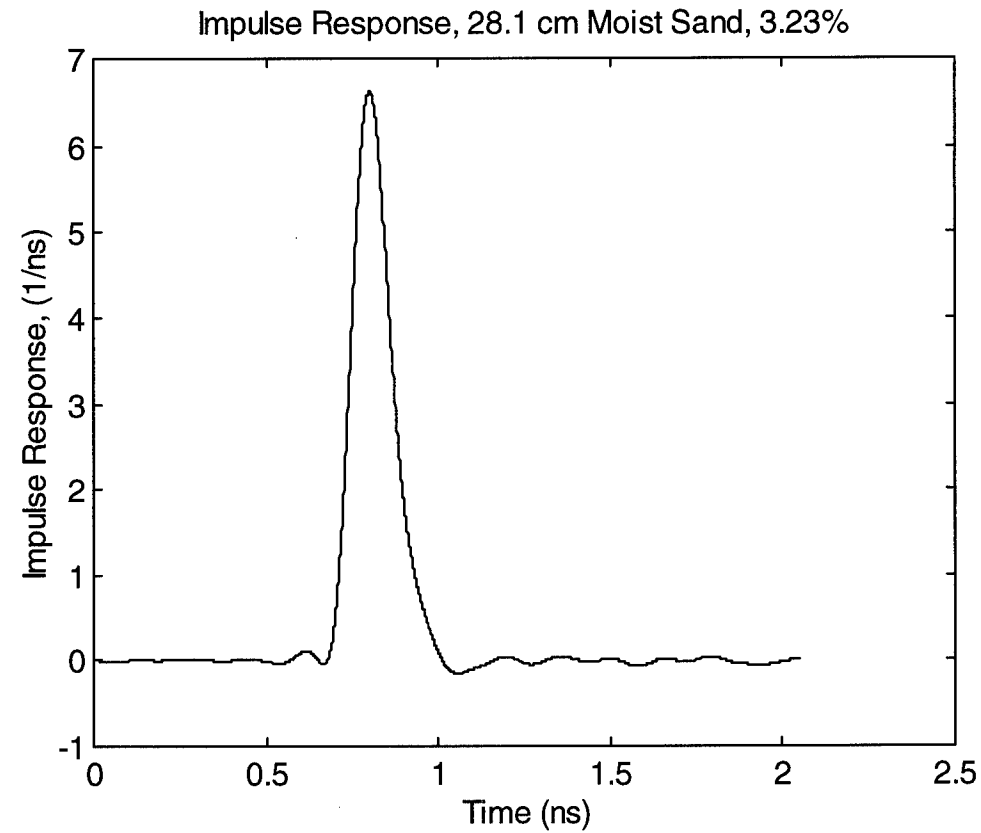


Figure 12.9. The impulse response (top) and its integral (bottom) of 28.1 cm moist sand, 3.23%.

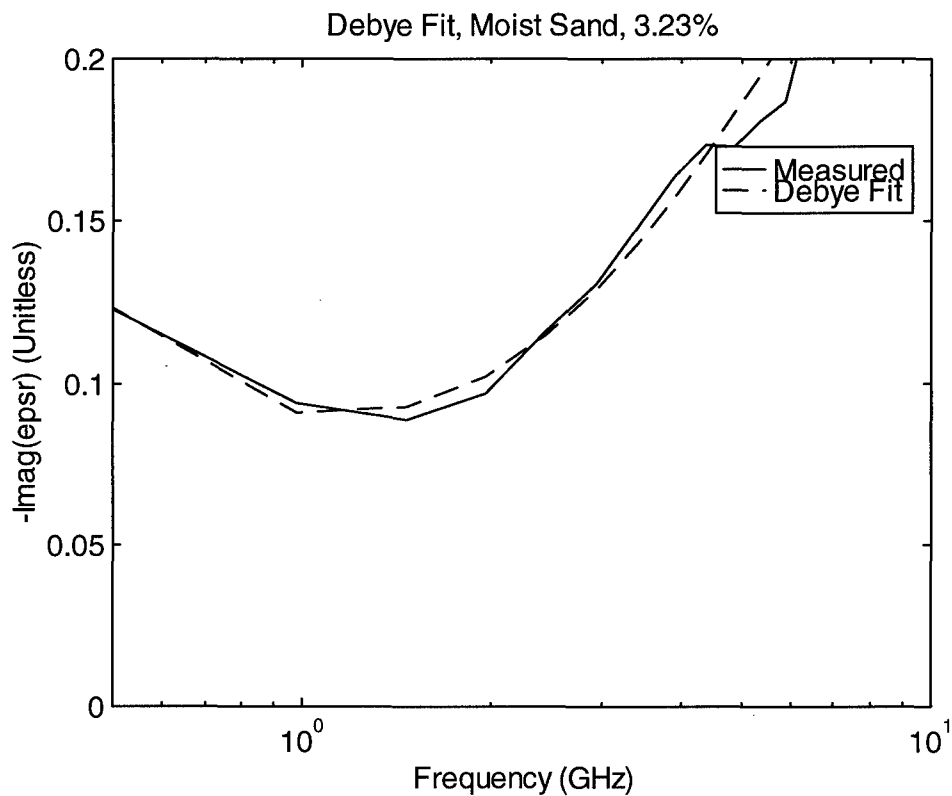
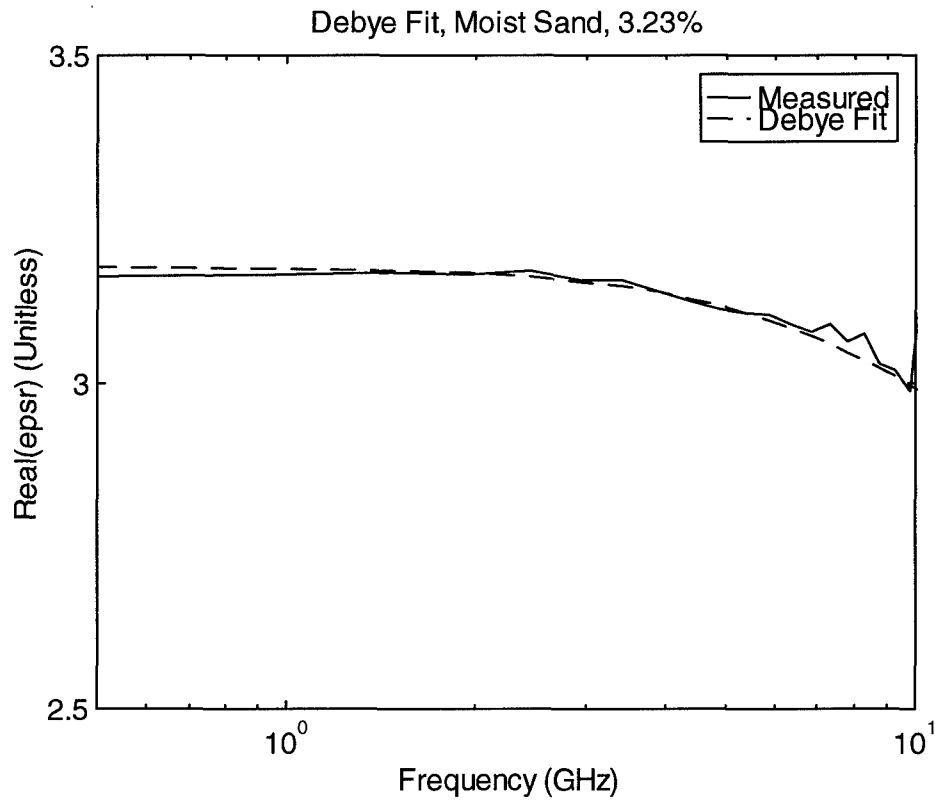


Figure 12.10. Measured dielectric constant of moist sand 3.23%, and the Debye model fit, including conductivity, real and imaginary parts.

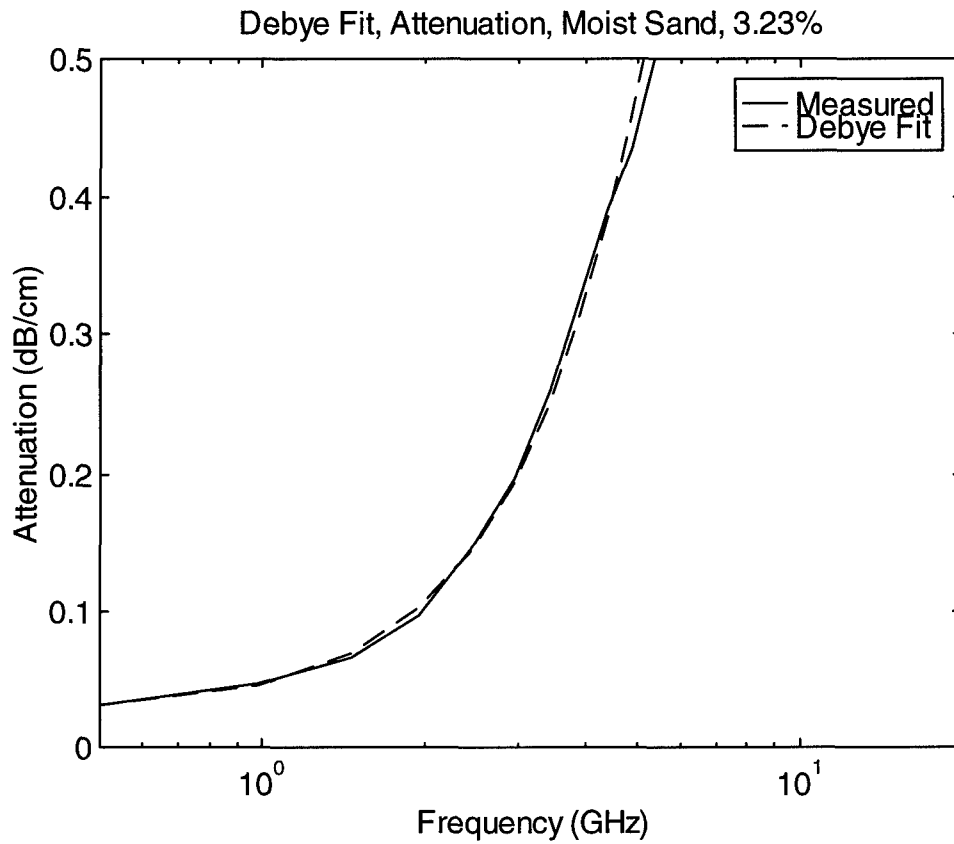


Figure 12.11. Attenuation constant of moist sand, 3.23%, measured and Debye model fit, including conductivity.

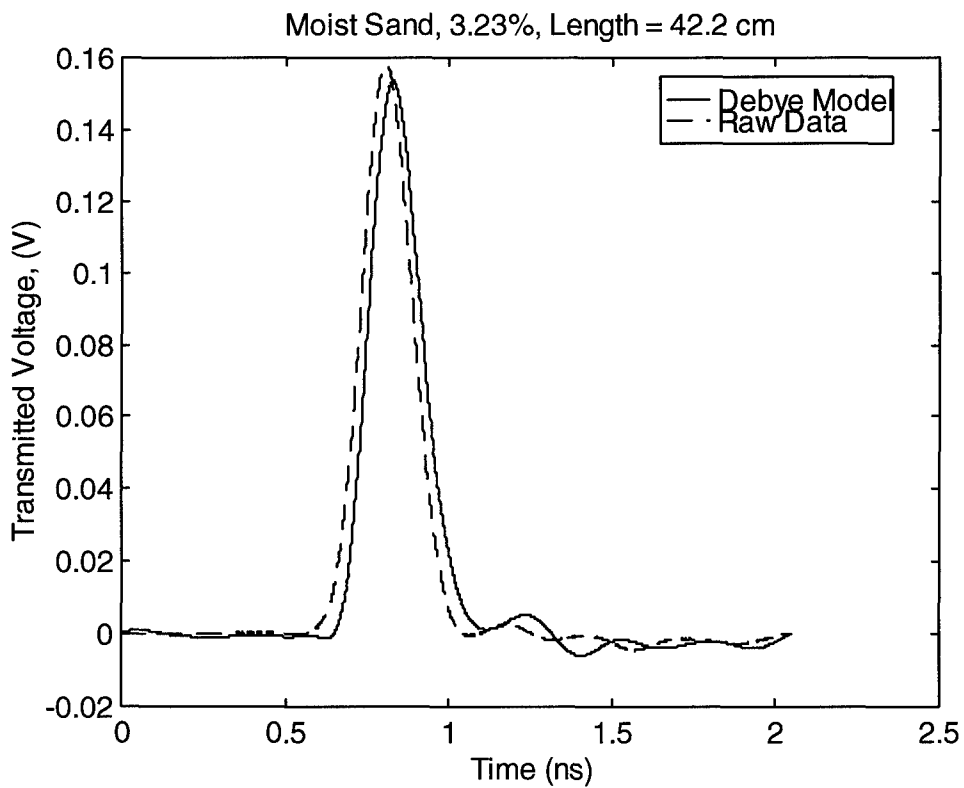
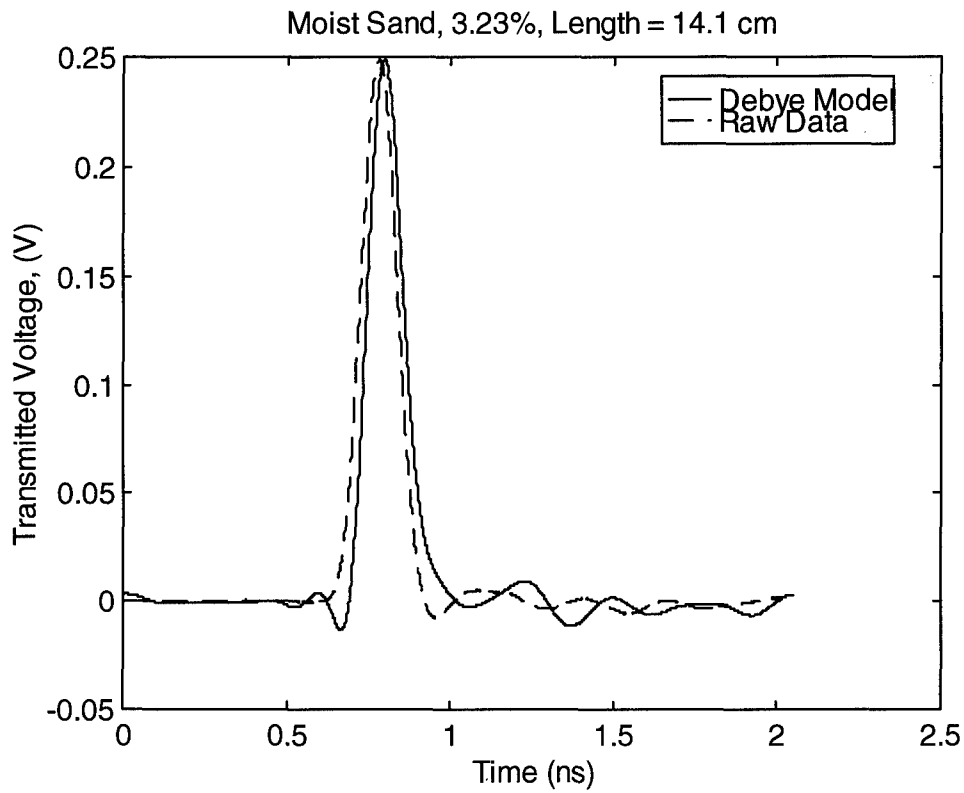


Figure 12.12. Propagation of the impulse through 14.1 cm and 42.2 cm of moist sand 3.23%, raw data and prediction with Debye model convolved with the air waveform.

XIII. Moist Sand: Propagation Waveshapes and Data Compilation

We now consider how impulses with various pulse widths propagate out to various distances using the models of moist sand derived in the last section. For moist sand with 1.58% and 3.23% water, we consider FWHM pulse widths of 30, 100, and 300 ps, and propagation distances of 0.1, 1, and 10 meters.

A diagram of the three input Gaussian pulses, with FWHM=30, 100, and 300 ps, was shown previously in Figure 6.1. The transmitted pulses are shown in Figures 13.1 through 13.3, for both moisture contents and for three different propagation lengths. From these graphs, we can clearly see the attenuation and pulse spreading of the waveform as they propagate. Note that due to high attenuation and dispersion, the propagated field at 10 meters is not quite visible on our scale.

Next, we compile the data in Figures 13.1-13.3, by plotting various waveform characteristics on log-log scales. This is a useful representation for system studies. First, we plot the peak magnitude for the six waveforms, at various distances (Figure 13.4). Next, we plot the FWHM of the waveforms, normalized to the FWHM of the input Gaussian (Figure 13.5). Finally, we plot the energy density of the waveforms (Figure 13.6), and the energy density normalized to the energy density of the input waveform (Figure 13.7). The energy density of a waveform is calculated as shown previously in Section VI.

As we expect, the magnitude decreases and the FWHM increases with propagation distance. The 30 ps pulse loses a factor of about one thousand (30 dB) in energy, after propagating 10 meters in 1.58% moist sand. The same pulse loses a factor of ten thousand, or about 40 dB, after propagating the same distance in the 3.23% moist sand. Note that these predictions are for plane-wave propagation. Since we have modeled the conductivity carefully here, we believe this provides a reasonable estimate of the actual values. A radar system would have to have an overall gain of perhaps 20 dB larger than these losses, in order to be functional. We believe that transient radar systems with gains of this order of magnitude are feasible.

These data imply that impulse radar systems, using pulses as narrow as 30 ps, can penetrate moist sand to depths larger than ten meters. While wider pulse widths have reduced attenuation, this is offset by a lower antenna gain. The necessary data are now in place to calculate the optimal pulse width for any given propagation distance.

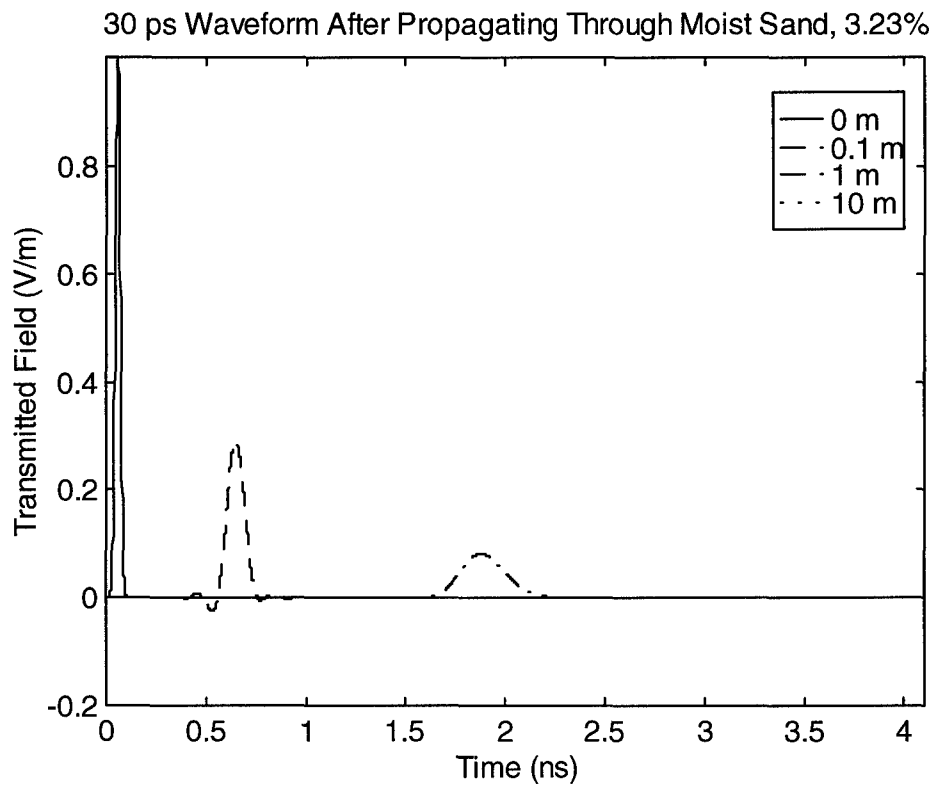
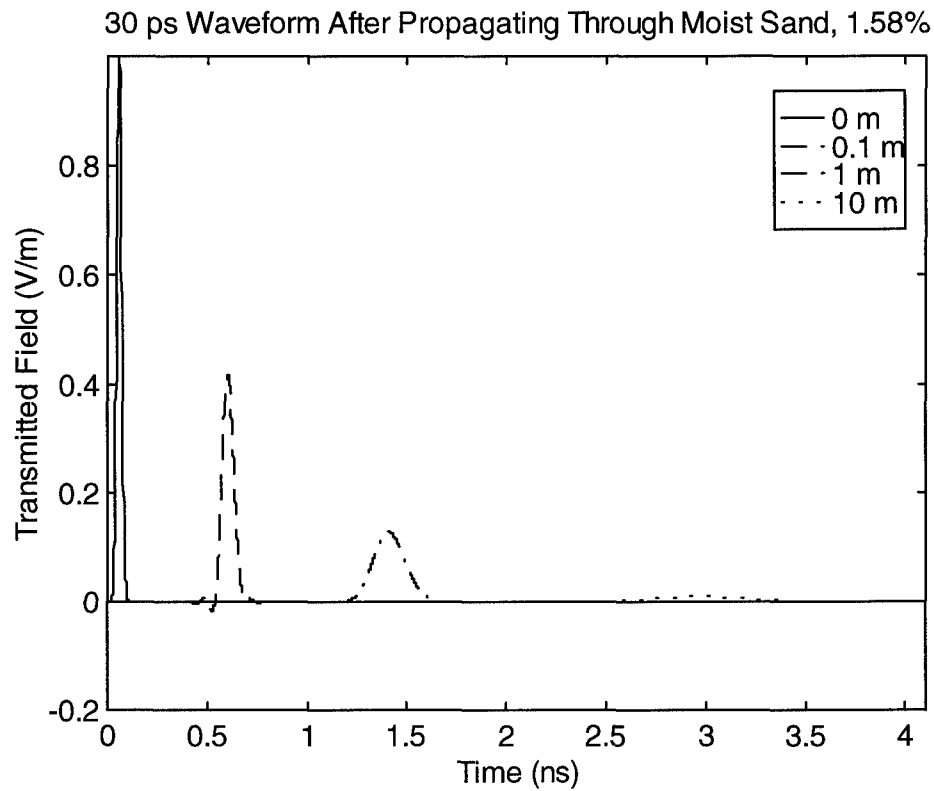


Figure 13.1. The propagated field of the 30 ps pulse at 0, 0.1, 1, and 10 meters, 1.58% top and 3.23% bottom. Note that the 10-meter pulse on the bottom is invisible. (Starting times shifted for clarity.)

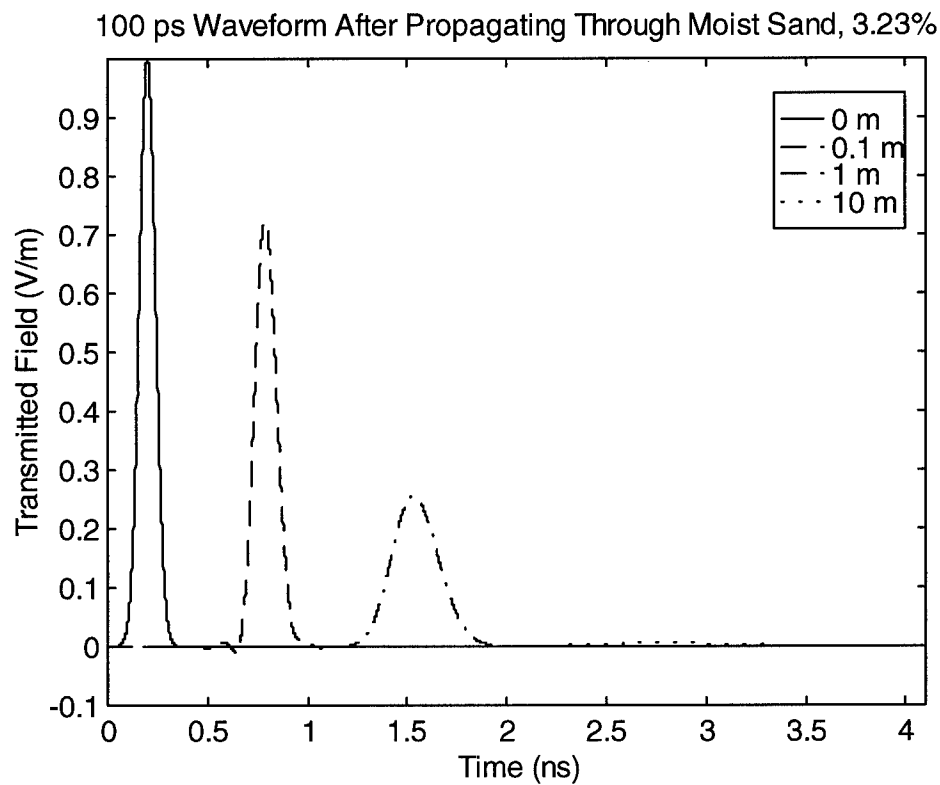
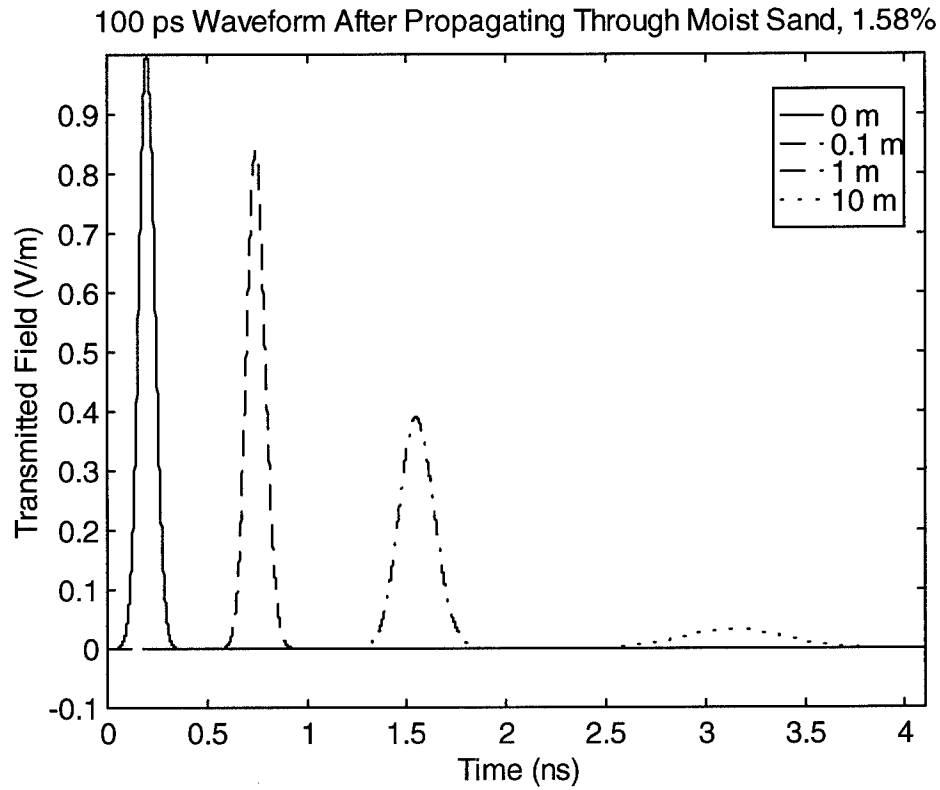


Figure 13.2. The propagated field of the 100 ps pulse at 0, 0.1, 1, and 10 meters, 1.58% top and 3.23% bottom. (Starting times shifted for clarity.)

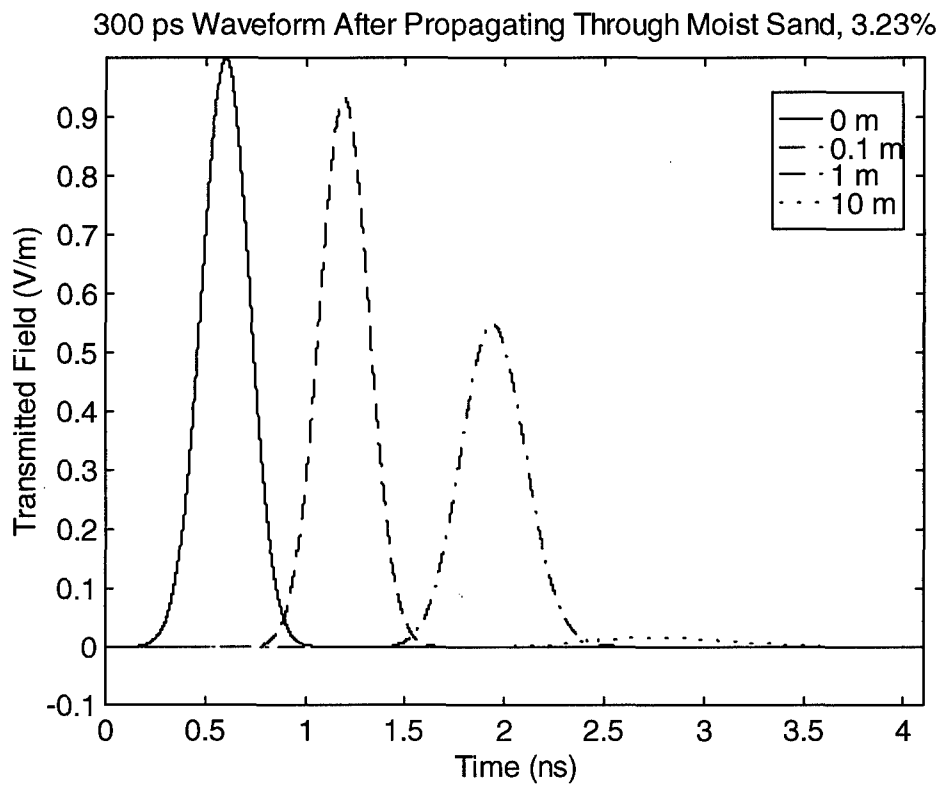
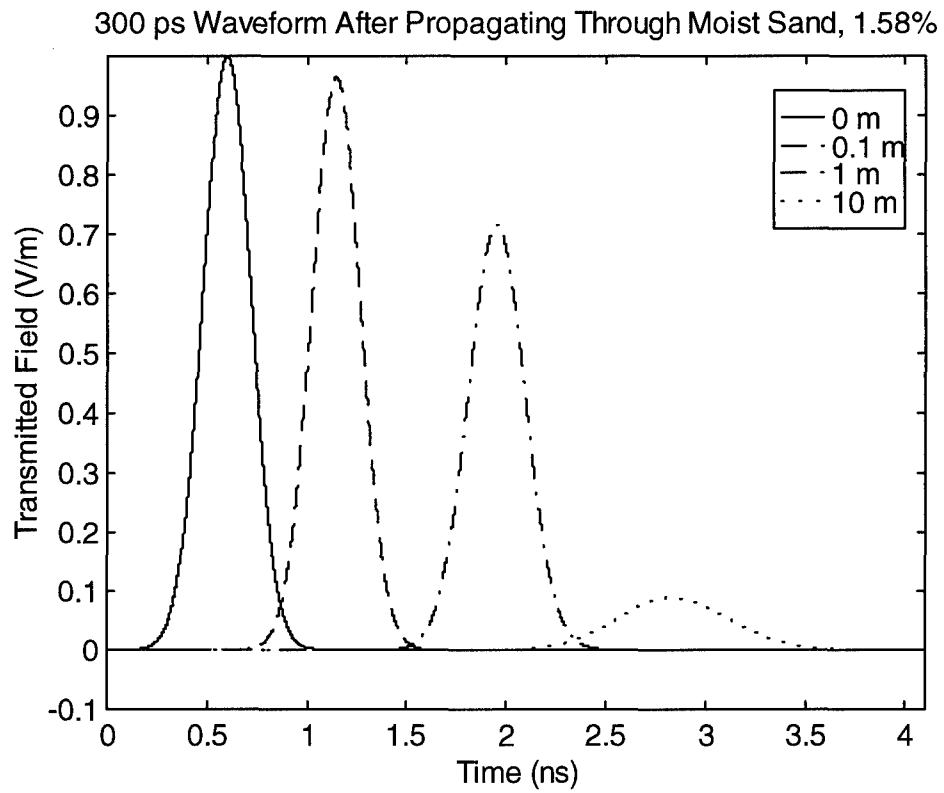


Figure 13.3. The propagated field of the 300 ps pulse at 0, 0.1, 1, and 10 meters, 1.58% top and 3.23% bottom. (Starting times shifted for clarity.)

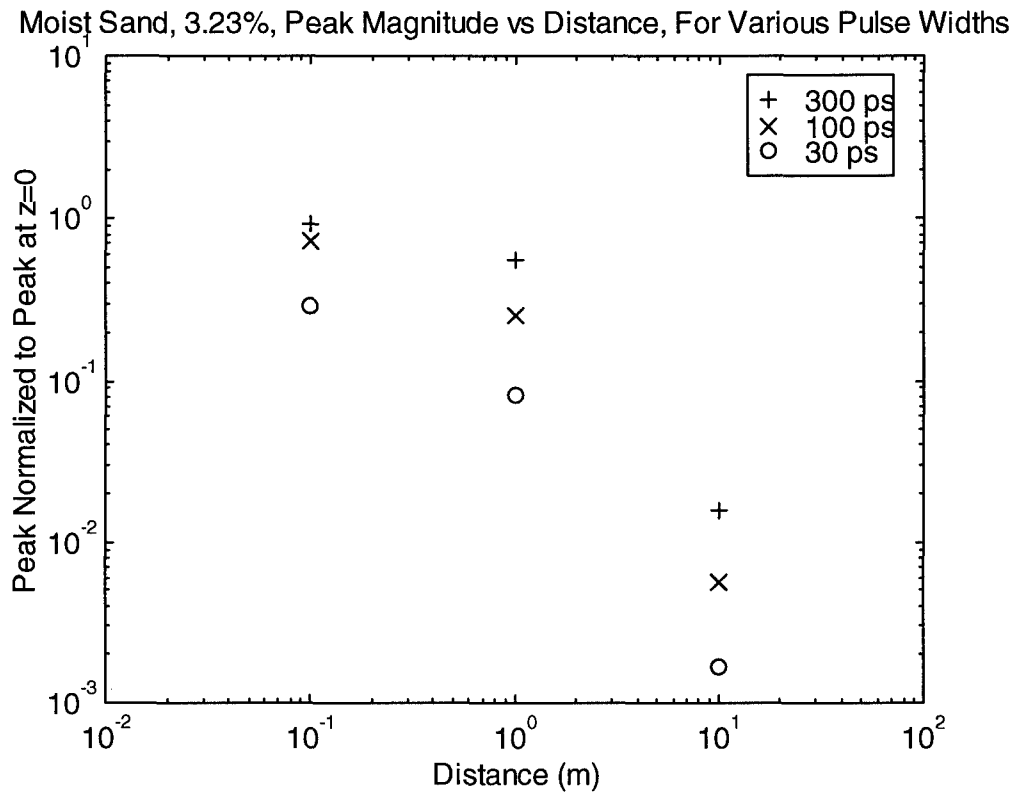
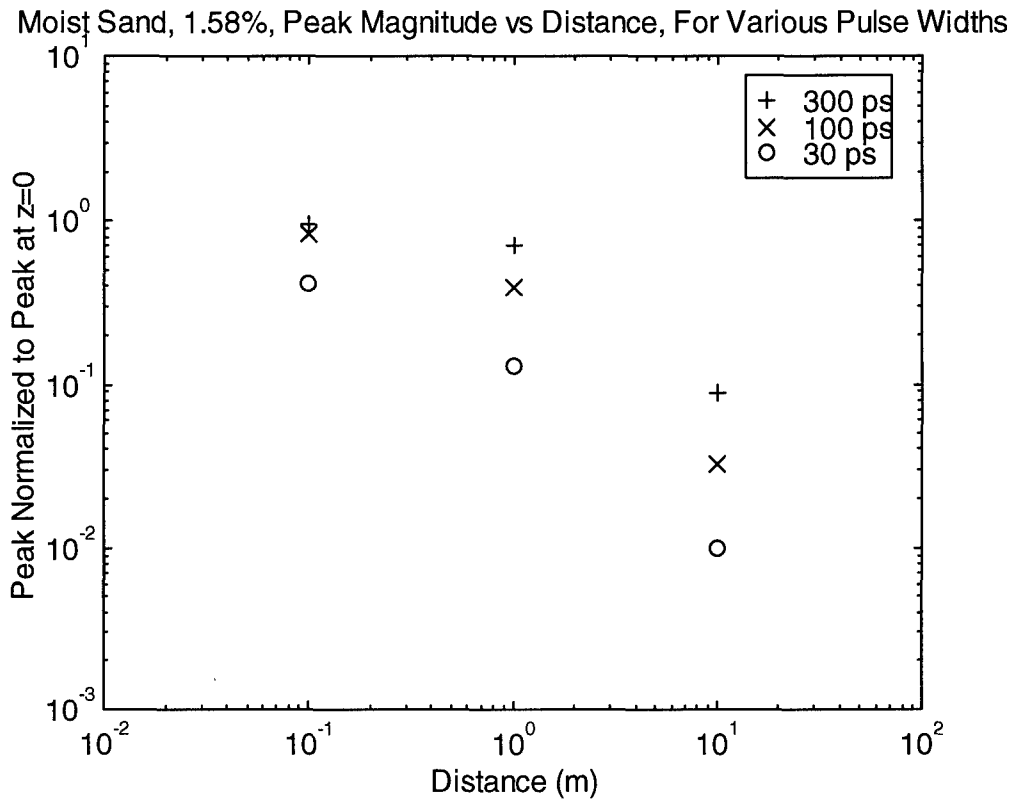
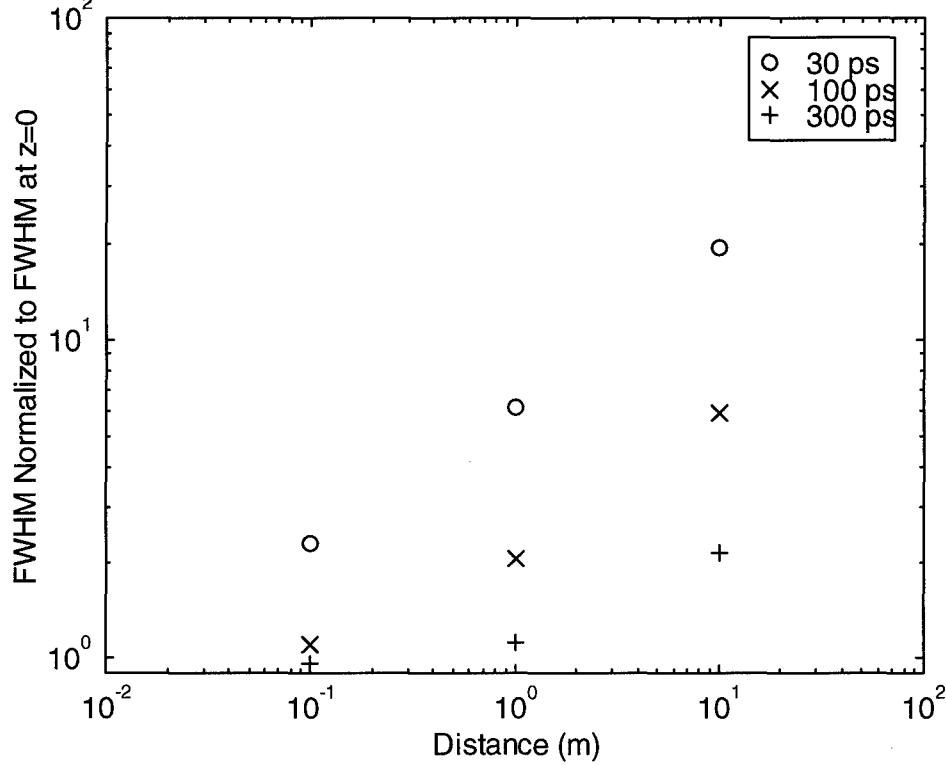


Figure 13.4. Peak waveform magnitude as a function of FWHM and propagation distance, 1.58% top and 3.23% bottom.

Moist Sand, 1.58%, Normalized FWHM vs Distance, For Various Pulse Widths



Moist Sand, 3.23%, Normalized FWHM vs Distance, For Various Pulse Widths

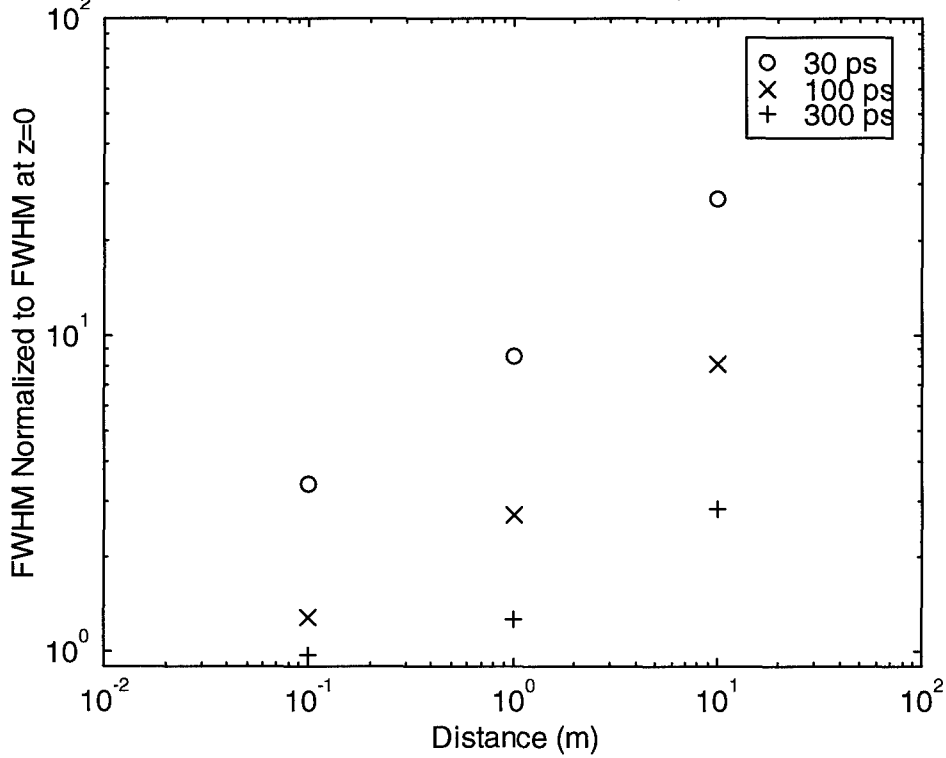


Figure 13.5. Normalized FWHM as a function of input FWHM and propagation distance, 1.58% top and 3.23% bottom.

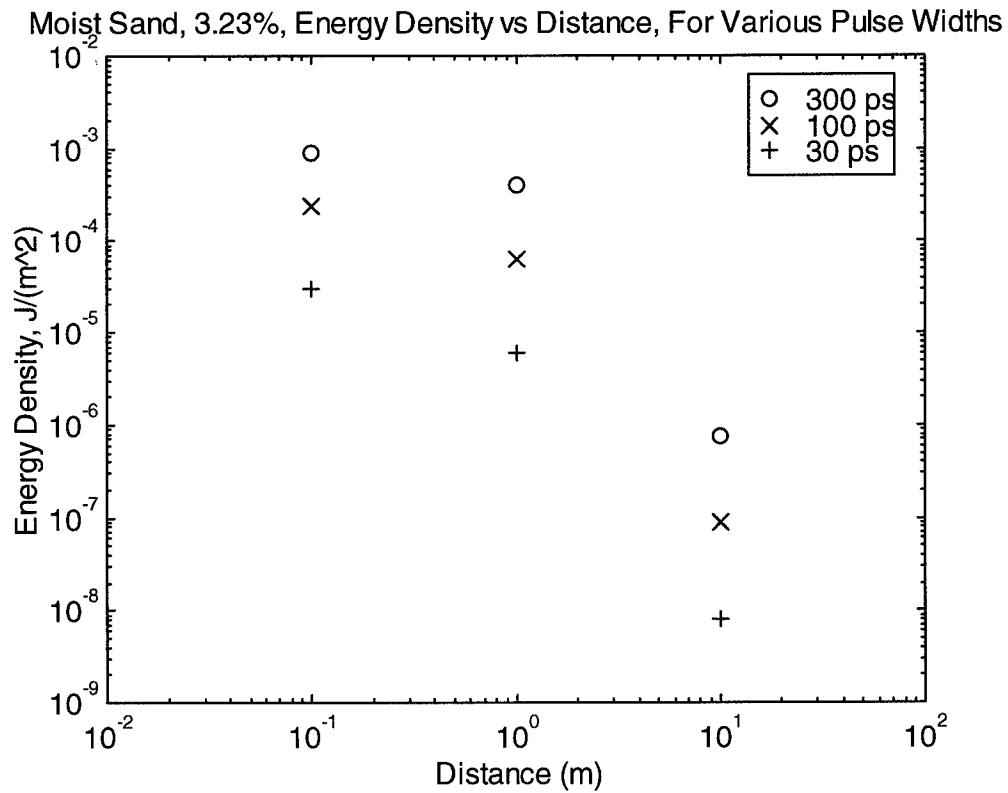
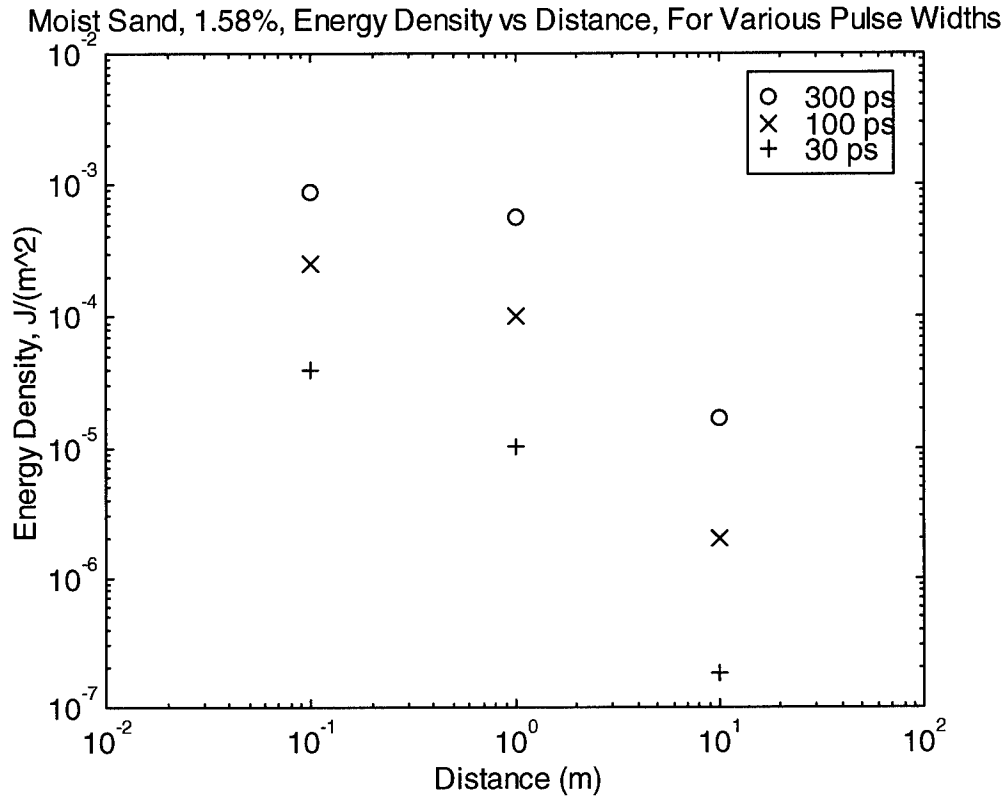


Figure 13.6. Energy density as a function of input FWHM and propagation distance, 1.58% top and 3.23% bottom.

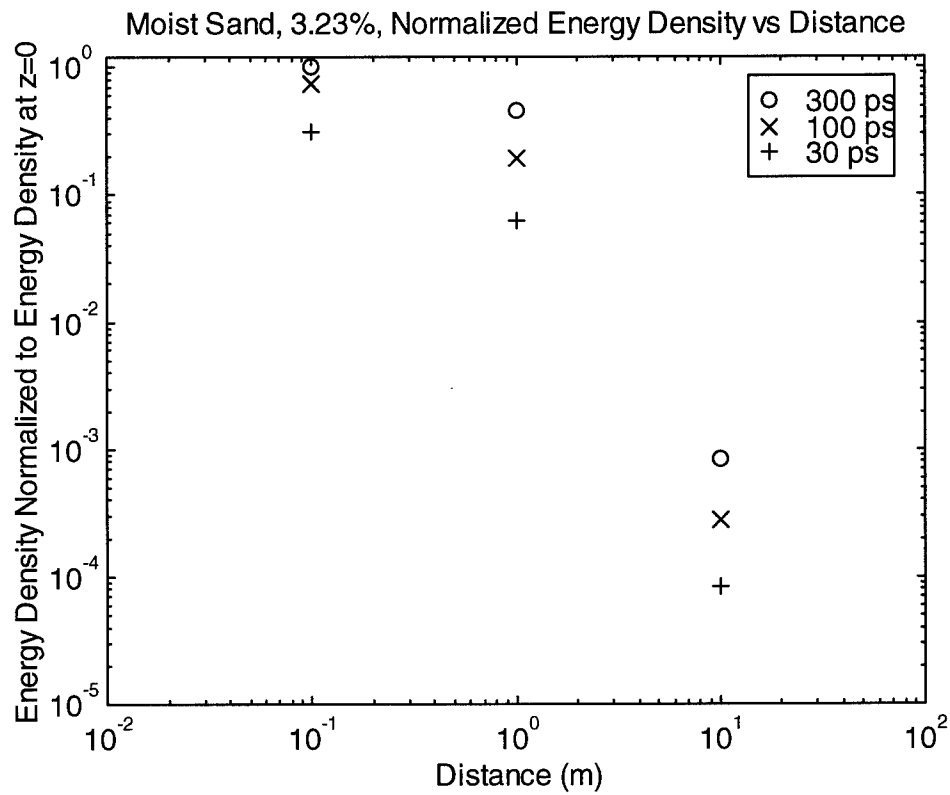
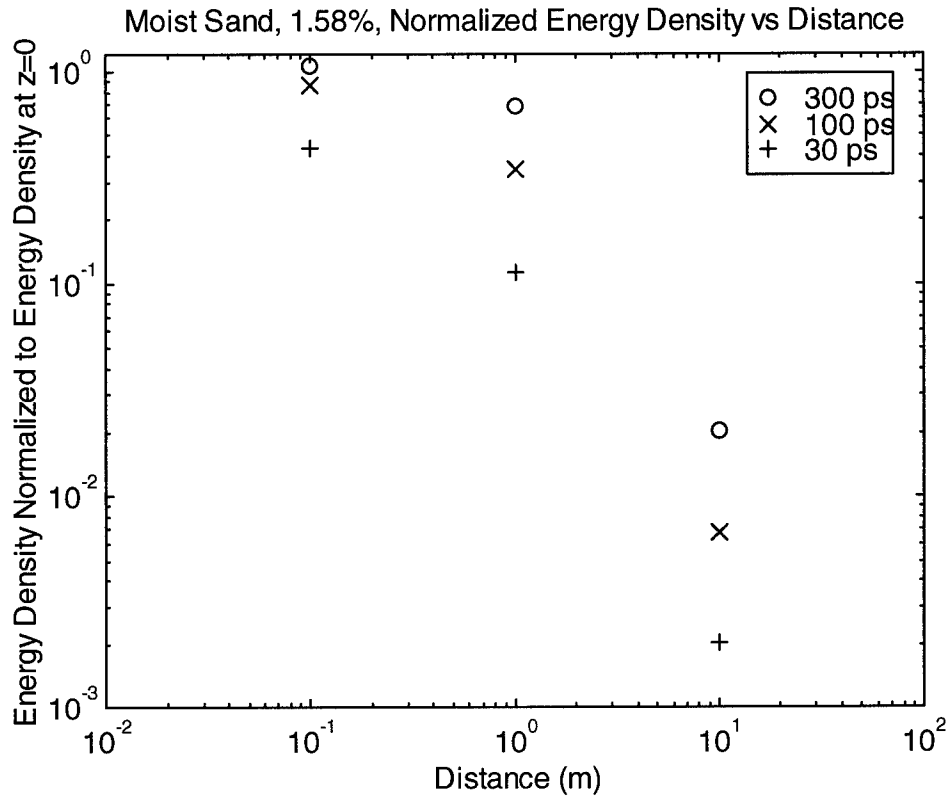


Figure 13.7. Normalized Energy density as a function of input FWHM and propagation distance, 1.58% top and 3.23% bottom.

XIV. Dry Sand and Concrete: Model Refinements to Include Conductivity

We refine here the Debye and Lorentz model parameters of dry sand and concrete. We do so because at the time we originally analyzed the data, we had not yet implemented conductivity into our Debye and Lorentz models. By including conductivity, we obtain a slightly better fit to the dielectric constant data.

First, we consider dry sand. The data for dry sand appears in Section IV of this report, and a Debye model that includes conductivity appears in equation (2.6). The new parameters for dry sand are shown in Table 14.1. Comparisons of the new model to the measured dielectric constant and attenuation are in Figures 14.1 and 14.2.

Finally, we provide a new model of concrete, by adding the conductivity term to the Lorentz model. The concrete was analyzed in Section VIII of this report.

$$\epsilon_r(\omega) = \epsilon_\infty + (\epsilon_s - \epsilon_\infty) \frac{(\alpha^2 + \beta^2)}{(\alpha^2 + \beta^2) + j2\omega\alpha - \omega^2} + \frac{\sigma}{j\omega\epsilon_0} \quad (4.1)$$

This new model for the dielectric constant is just the same as the previous Lorentz model, with the exception that we have added a conductivity term, $\sigma/j\omega\epsilon_0$, where σ is the conductivity, and ϵ_0 is the permeability of free space. Using this model, the new Lorentz parameters are shown in Table 14.2. Comparisons of the new model to the measured dielectric constant and attenuation are shown in Figures 14.3 and 14.4.

Table 14.1. Debye Parameters for Dry Sand, Including Conductivity

Parameter	Debye Fit for Dry Sand
ϵ_s	2.5160
ϵ_∞	2.4725
t_0 (ps)	17.3
σ (mho/m)	1.5526×10^{-3}

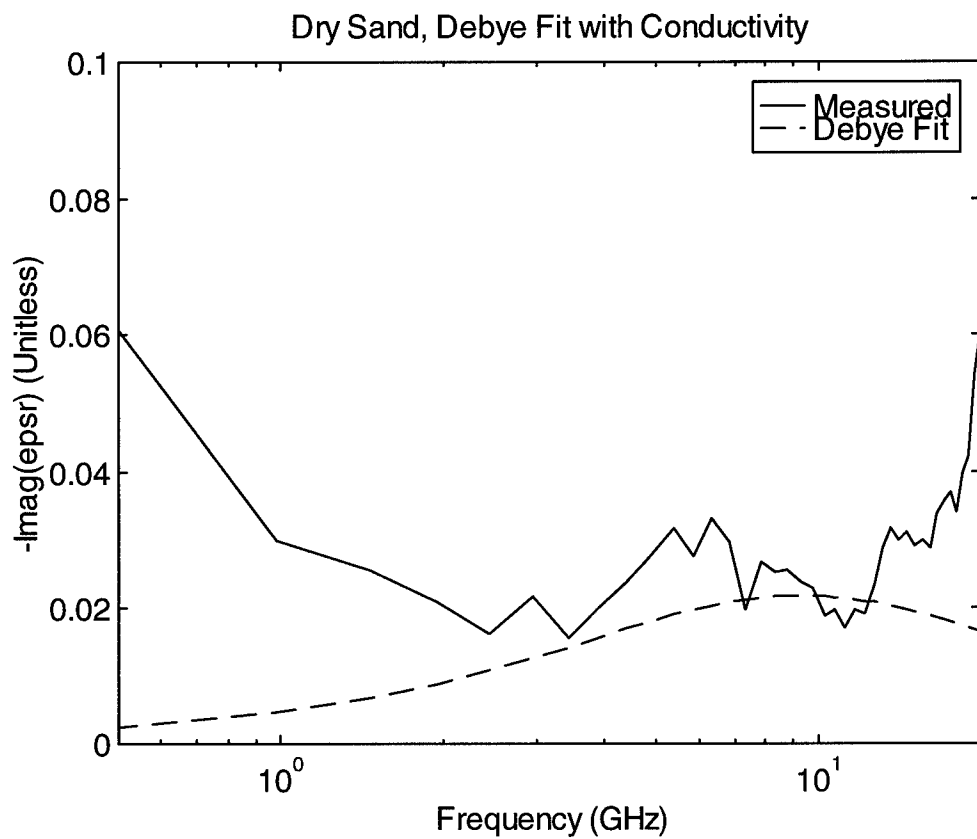
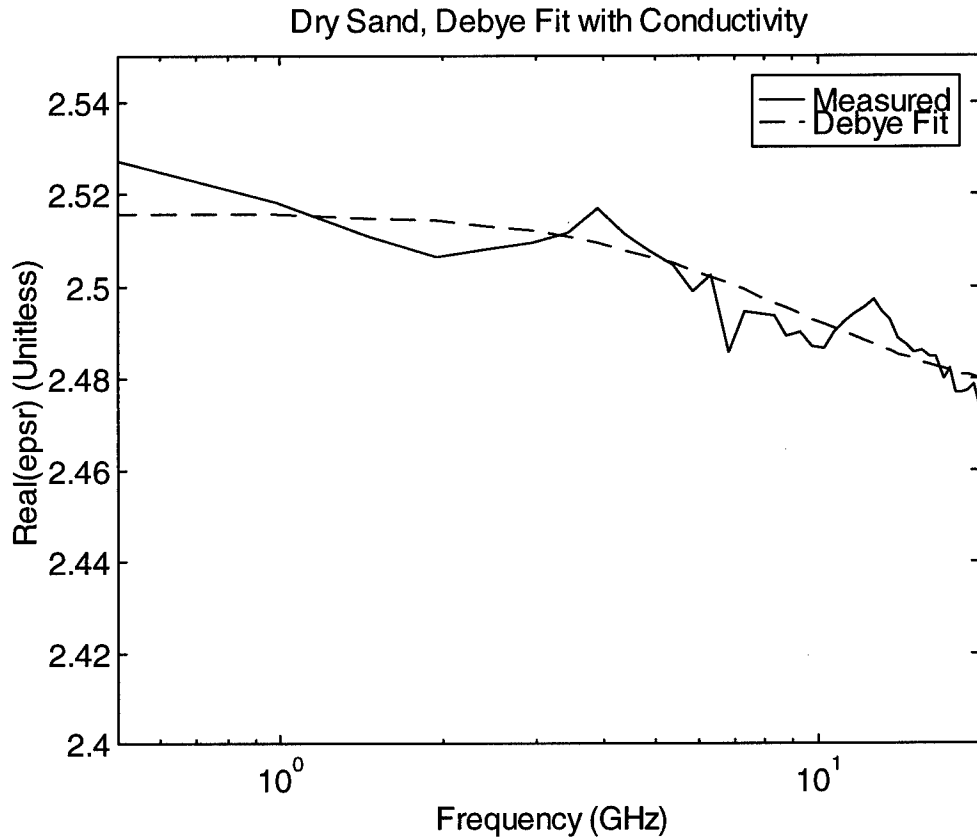


Figure 14.1. Comparison of dry sand dielectric constant to Debye fit, with conductivity.

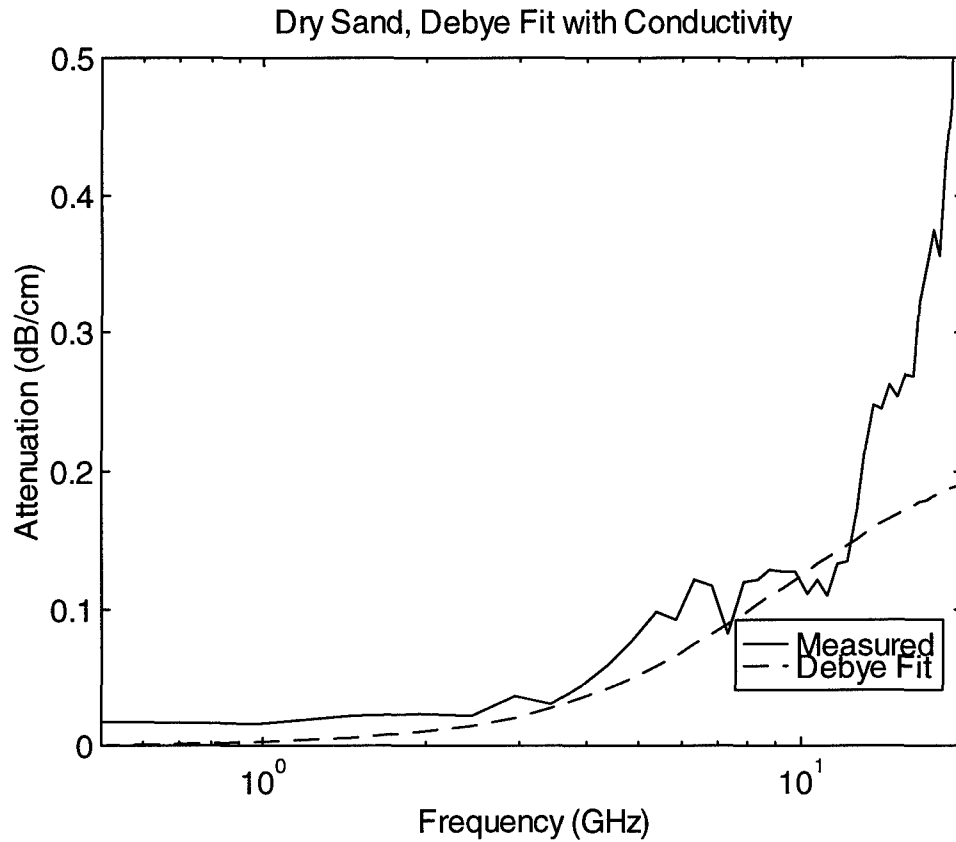


Figure 14.2. Comparison of dry sand attenuation to Debye fit, with conductivity.

Table 14.2. Lorentz Model Parameters for Concrete, Including Conductivity.

Parameter	Lorentz Model Fit for Concrete
ϵ_s	3.4406
ϵ_∞	1.9952×10^{-5}
α (ns ⁻¹)	9.8509
$f_{res} = \beta/(2\pi)$ (GHz)	50.6823 GHz
σ (mho/m)	7.6335×10^{-3}

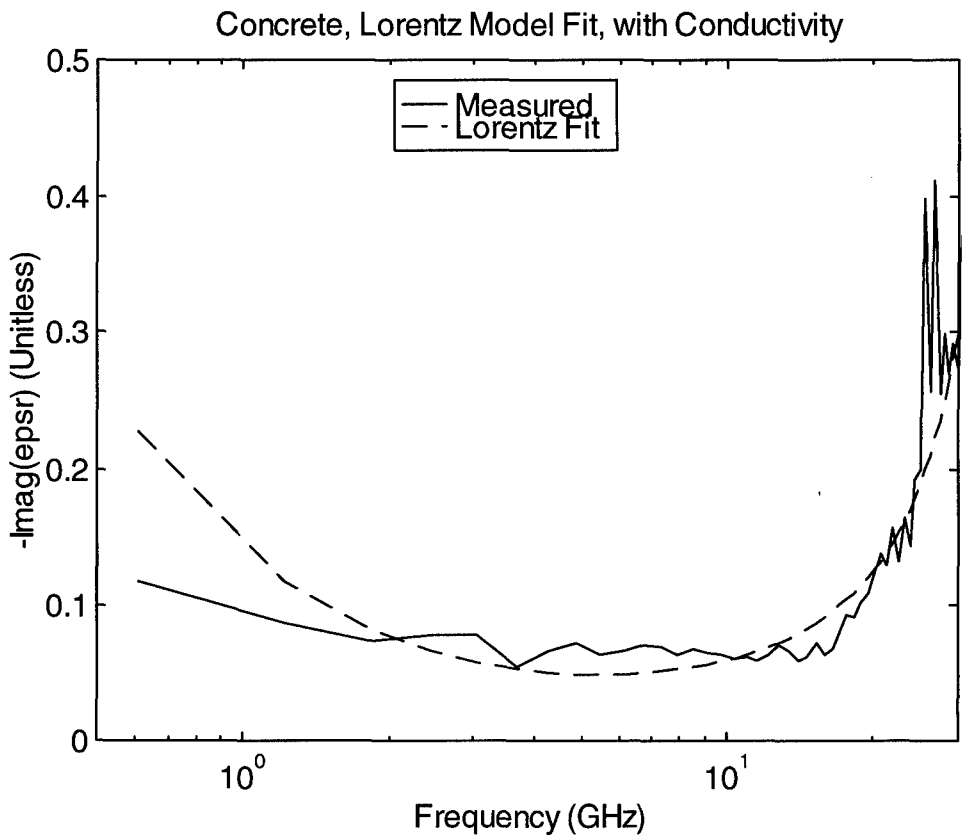
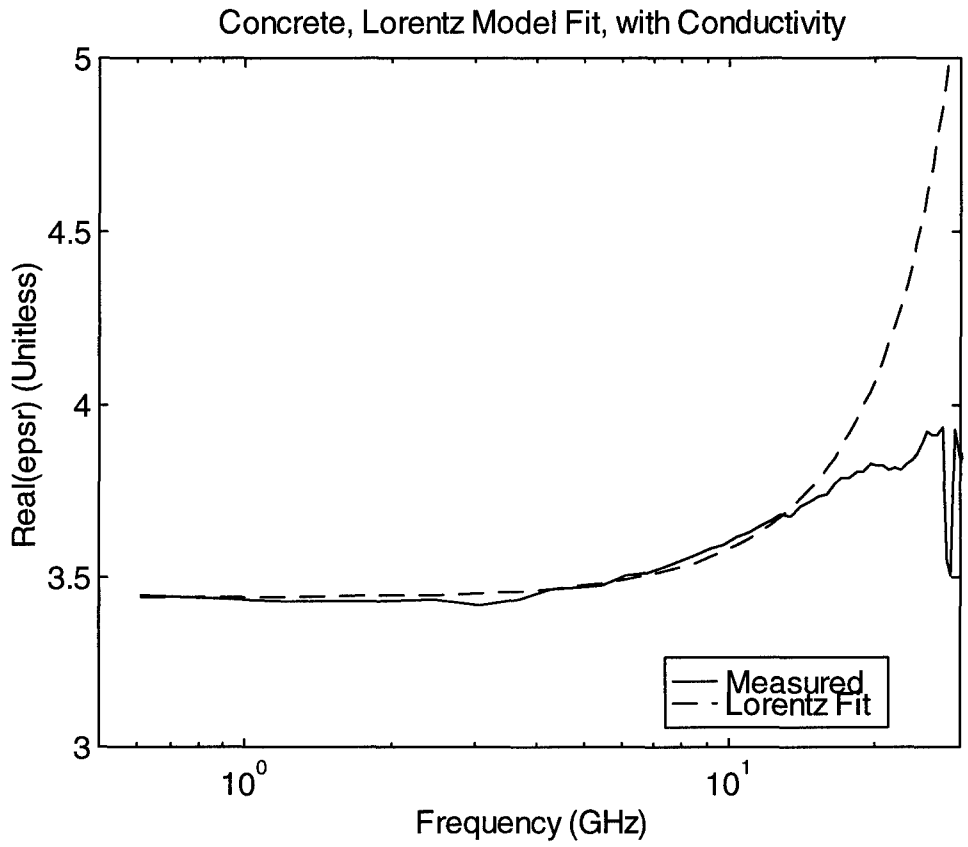


Figure 14.3. Comparison of concrete dielectric constant to Lorentz fit, with conductivity.

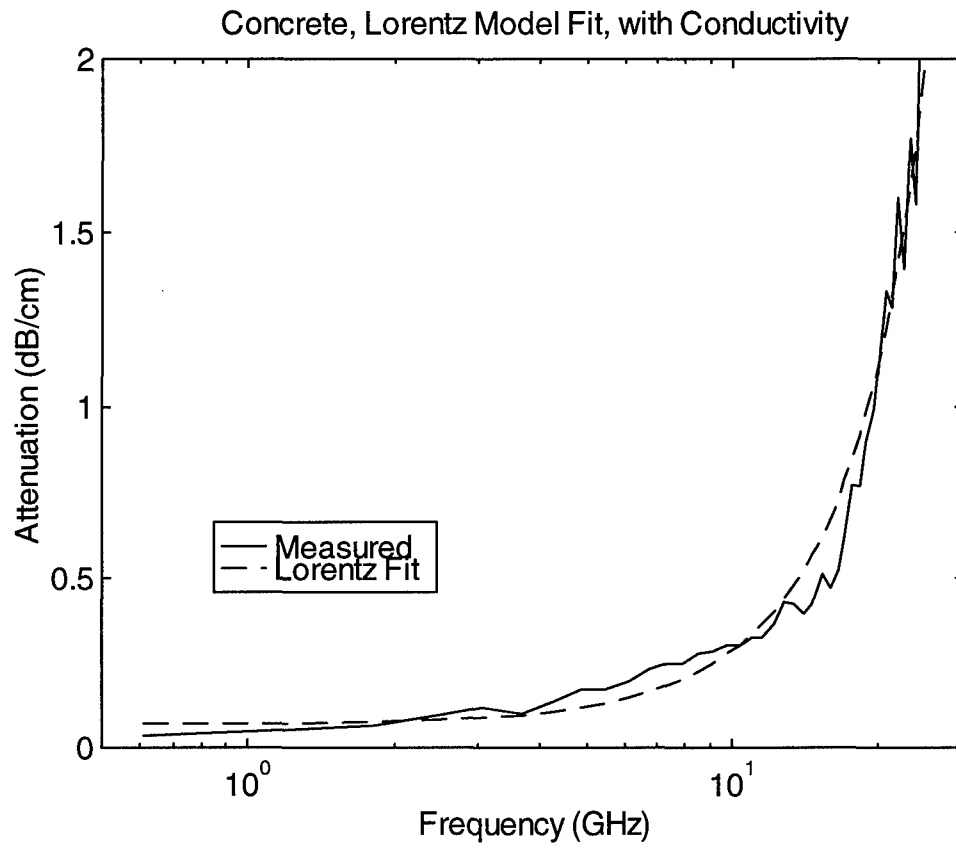


Figure 14.4. Comparison of concrete attenuation to Lorentz fit, with conductivity.

XV. Free-Field Measurements of Dielectric Constants

To demonstrate free-field measurements of dielectric properties, we performed a remote measurement of the reflection from dry sand and from concrete. Using this method, we could extract an approximate dielectric constant of the measured material, and compare the result to data from the coaxial test fixture.

The measurement was performed in TDR mode using a single antenna, and using the Tektronix CSA803 digital sequential sampling oscilloscope with the SD24 TDR sampling head. The SD24 head contains a built-in source providing a 0.25 V step waveform. The two antennas used were the nine-inch diameter lens IRA and the nine-inch diameter lens reflector IRA, both of which were built for an earlier part of this contract. The antenna was placed 35 cm from the sand sample and 31 cm from the concrete sample. The sand had a moisture content of less than 0.03% by weight. The concrete sample has dimensions of 24" x 24" x 6.5". For these dimensions, only the first nanosecond after the reflected impulse is valid.

The method involves the measurement of three waveforms. First, the TDR waveform is taken of the dielectric sample. Next, a metal plate is placed in front of the dielectric sample, and a reference (or normalization) waveform is taken. The reference waveform gives a 100% reflection. Finally, the antenna is pointed into the air, and a background waveform is taken. The background waveform contains the launched signal and reflections from the antenna and cables. The background waveform is subtracted from both the TDR waveform and the reference waveform to remove the source waveform and artifacts due to internal reflections. Background subtraction is only needed for the TDR method, and is not employed when two antennas are used in radar mode.

First, we consider reflection from sand, using a lens IRA. These data were acquired at the Eglin Air Force Base sand box facility, which uses thick wooden planks (4.13 cm) to retain the sand. It appears that the wood has little effect on the measurement.

All three waveforms of raw data for the reflection from sand are shown in Figure 15.1. The dc level of all the signals have been adjusted to zero. Next, we subtract the background waveform from the signal and reference waveforms. The results are shown in Figures 15.2 and 15.3, after adjusting the dc level, and after adding a cosine taper to the end of the signal. These waveforms show the reflected pulse from the dielectric sample and a perfect reflector. The reflection coefficient is determined by deconvolving the reference signal (reflection from a conducting plate) from the signal waveform (reflection from the dielectric layer). The deconvolution is implemented by dividing the signal waveform by the reference waveform in the frequency domain. The magnitude of the reference waveform (denominator) is limited to being no less than one percent of its maximum, in order to avoid dividing by a very small number. The resulting ratio then is filtered by a 5th order modified Butterworth filter at 8 GHz. The result of the deconvolution in the frequency domain is shown in Figure 15.4, and in the time domain in Figure 15.5. This time domain response is the impulse response of the medium. When integrated, we obtain a unitless step response, which corresponds closely to the reflection coefficient we expect.

The integrated impulse response (step response) for sand is shown in Figure 15.6. From Section IV of this report, we expect a dielectric constant of about 2.5, which corresponds to a reflection coefficient of -0.225 . Recall that the reflection coefficient, ρ , is given by

$$\rho = \frac{1 - \sqrt{\epsilon_r}}{1 + \sqrt{\epsilon_r}} \quad (15.1)$$

In our step response, we find a jump of about 0.225 at 1.2 ns. Note that a jump of $+0.225$ in the step response corresponds to a reflection coefficient of -0.225 , because we normalized to reflection from a conducting plate, with a reflection coefficient of -1 . Thus, our free field measurements of sand are consistent with our coaxial test fixture measurements.

Next, we repeat the measurement of sand using a nine-inch diameter reflector IRA. The raw data is shown in Figure 15.7. Note that the ends of the waveform have saturated the sampler, so these are time-gated out of the signal processing. We proceed with the same calculation as above, using a 5th-order modified Butterworth filter at 10 GHz, and arrive at the step response shown in Figure 15.8. Once again, we see a jump of about 0.225 in the step response at the interface, which is the predicted reflection for a step waveform from dry sand, with dielectric constant 2.5. We note that the measurements with two different types of antennas give the same result for the reflection coefficient. The raw data for the two antennas appear quite different, but after processing we see agreement on the value of ρ .

Finally, we measure the dielectric constant of a concrete sample, using the lens IRA. The three raw data waveforms are shown in Figure 15.9, and the signal and reference waveforms are shown in Figures 15.10 and 15.11. The frequency domain impulse response is calculated as before, using a 10th-order modified Butterworth filter at 8 GHz. The resulting frequency domain impulse response is shown in Figure 15.12, and the corresponding time domain impulse response is shown in Figure 15.13.

The integrated impulse response (step response) for concrete is shown in Figure 15.14. There is a sudden jump of approximately 0.5 in the step response, which is due to the interface. We calculate a reflection coefficient of 0.3 using a dielectric constant of 3.5, which was measured in the coaxial test fixture, as described in Section 8 of this report. The source of the difference in ρ is unclear, but the two concrete samples were not prepared in the same manner. It is possible that a concrete sample that has been sitting in the moist air near Eglin AFB could have a higher moisture content and dielectric constant than the smaller samples used in the coaxial test fixture, which had been baked in an oven. Also, there is no rigid formula for concrete, so it is possible that different samples could be composed of different materials. While we carefully controlled the content of the material in our coaxial test fixture, this was not possible with the concrete slab we measured in the free-space measurement.

In the previous discussion, we compared reflection coefficients of the step waveform measured in free space, to predictions based on the dielectric constant measured in a coaxial test

set. We could, however, just as easily compare dielectric constants. To do this, we simply invert equation (15.1), giving

$$\epsilon_r = \left(\frac{1-\rho}{1+\rho} \right)^2 \quad (15.2)$$

Thus, we can measure ϵ_r at a distance using antennas. Using this method, we find values of $\epsilon_r = 2.5$ for sand and 9 for concrete. This compares to measured values in the coaxial test fixture of 2.5 for sand and 3.5 for concrete. Since it was impossible to control the material content of the concrete slab, it is probably not fair to compare the free-field concrete data to the data taken in the coaxial test fixture.

Based on this data, we conclude that we can successfully find the dielectric constant of materials using reflections off an interface. In the case of sand, the extracted dielectric constants using the free-field method correspond nicely to those measured in our coaxial test fixture. In the case of concrete, we could successfully measure the dielectric constant, but we arrived at a different value than that obtained with the coaxial test fixture. This could be explained by different makeup and moisture content of the two concrete samples.

The TDR measurements with antennas demonstrated remote measurement of dielectric constant, but was not an ideal method. A true radar measurement, using separate transmitter and receiver, would be vastly superior, since the signal processing would not have to separate the transmit and receive data, and the transmit power would be many orders of magnitude higher. The TDR pulse power was 1.25 mW (0.25 V into 50 Ω), while the power for our radar transmitter is 125 kW (2.5 kV into 50 Ω). One would expect improved accuracy at higher power levels. Future experiments will address more accurate measurements using the high-power impulse radar technique.

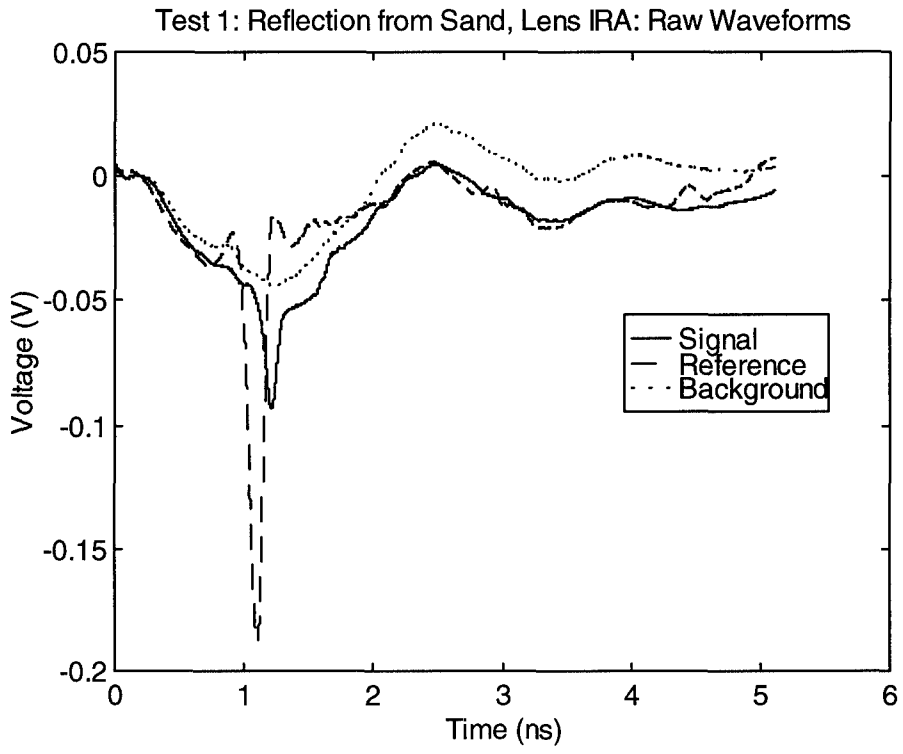


Figure 15.1. Raw data for reflection from sand with a Lens IRA.

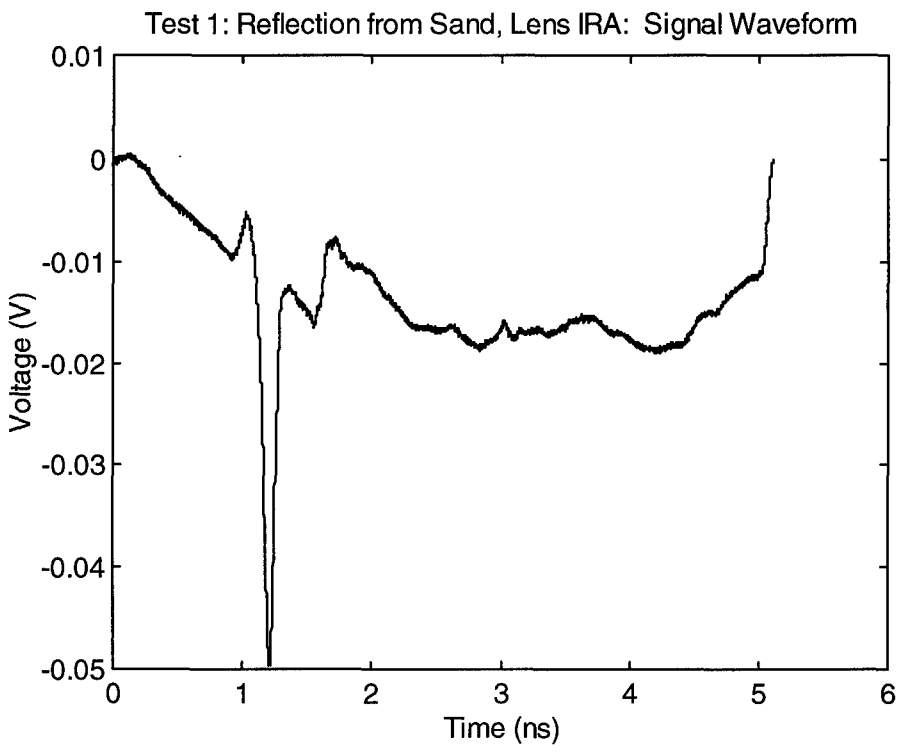


Figure 15.2. Signal waveform after background subtraction.

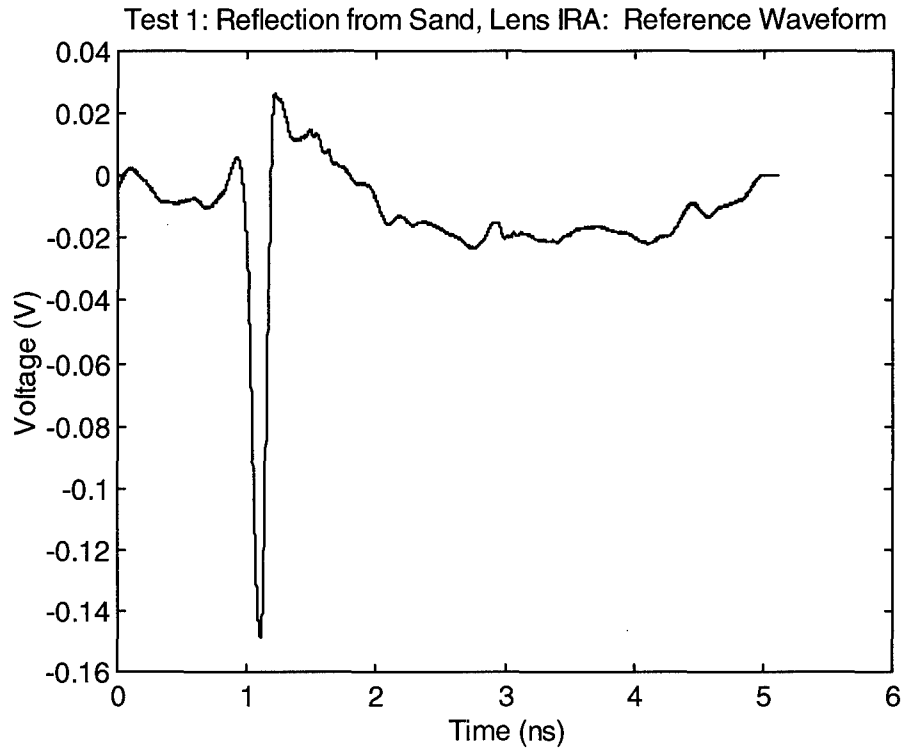


Figure 15.3. Reference waveform after background subtraction.

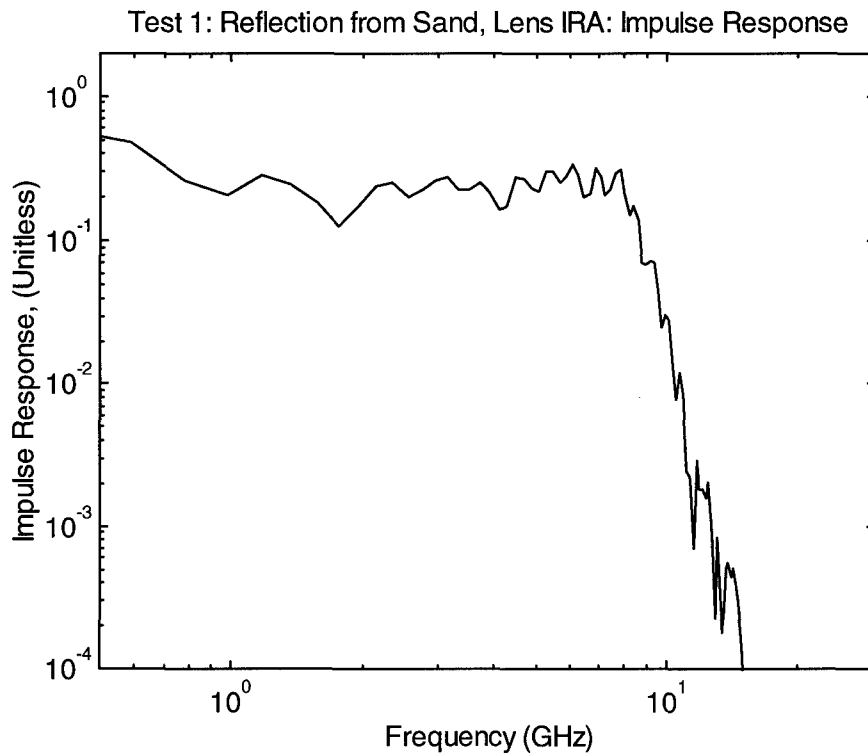


Figure 15.4. Frequency domain impulse response for sand reflection.

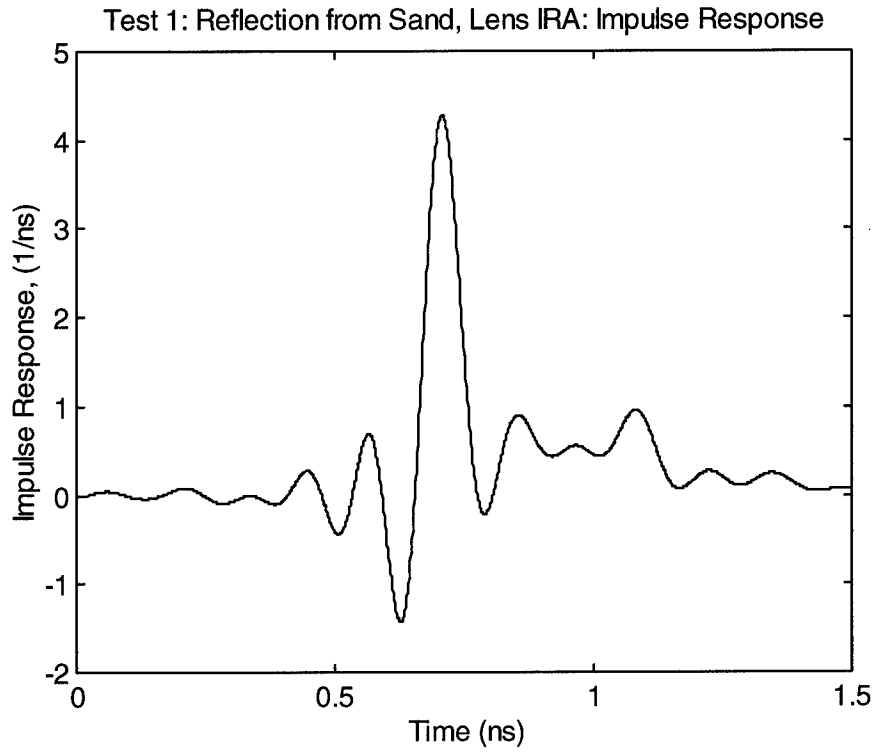


Figure 15.5. Impulse response for sand reflection.

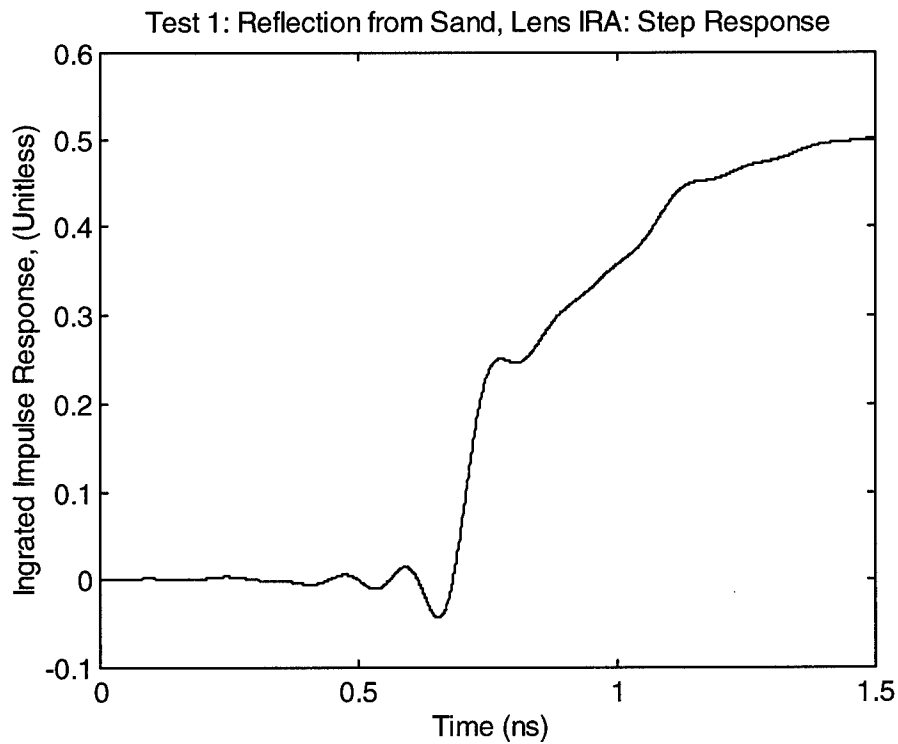


Figure 15.6. Step response for sand reflection, measured with a lens IRA.

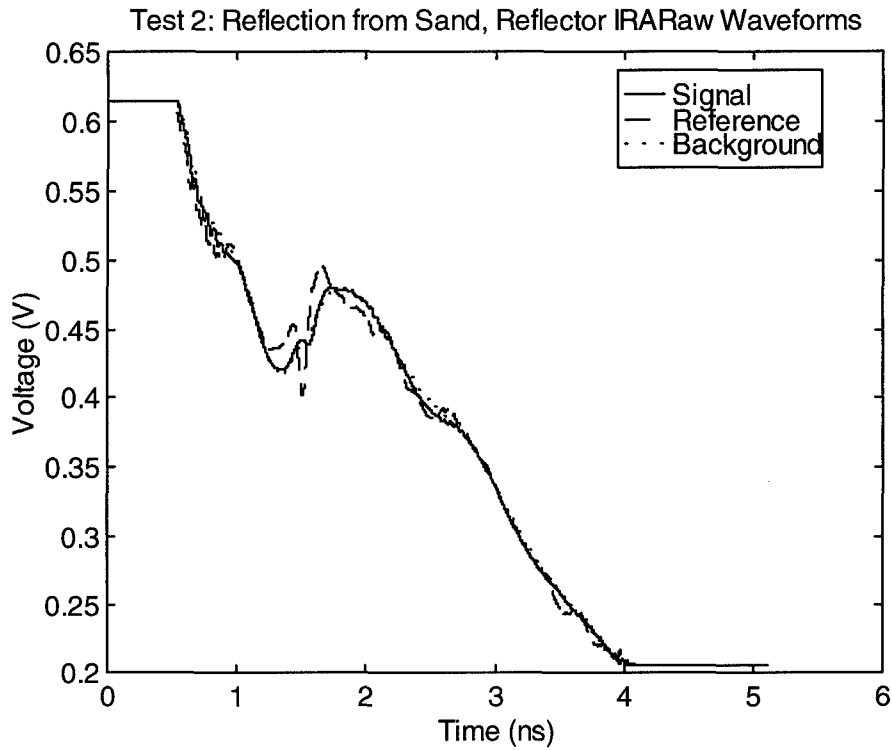


Figure 15.7. Raw data for reflection from sand with a reflector IRA.

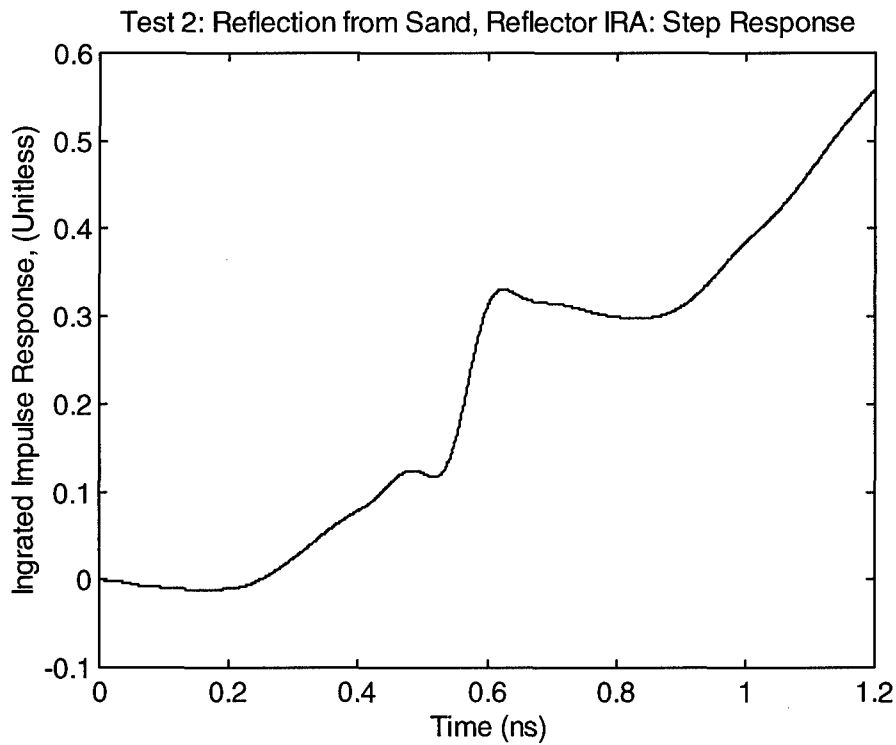


Figure 15.8. Step response for sand reflection, measured with a reflector IRA.

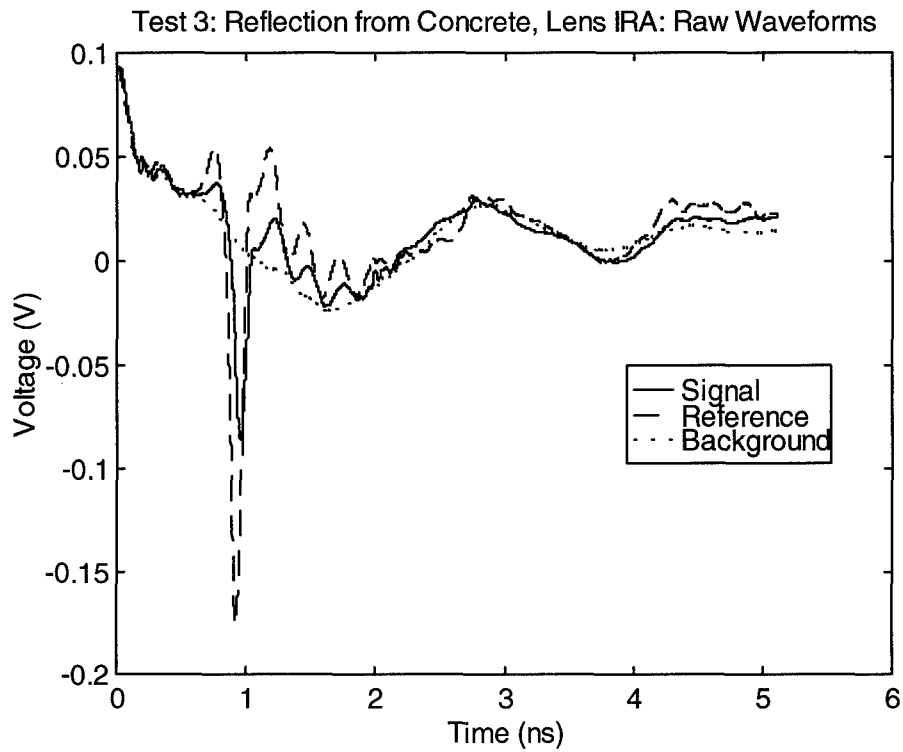


Figure 15.9. Raw data for reflection from concrete.

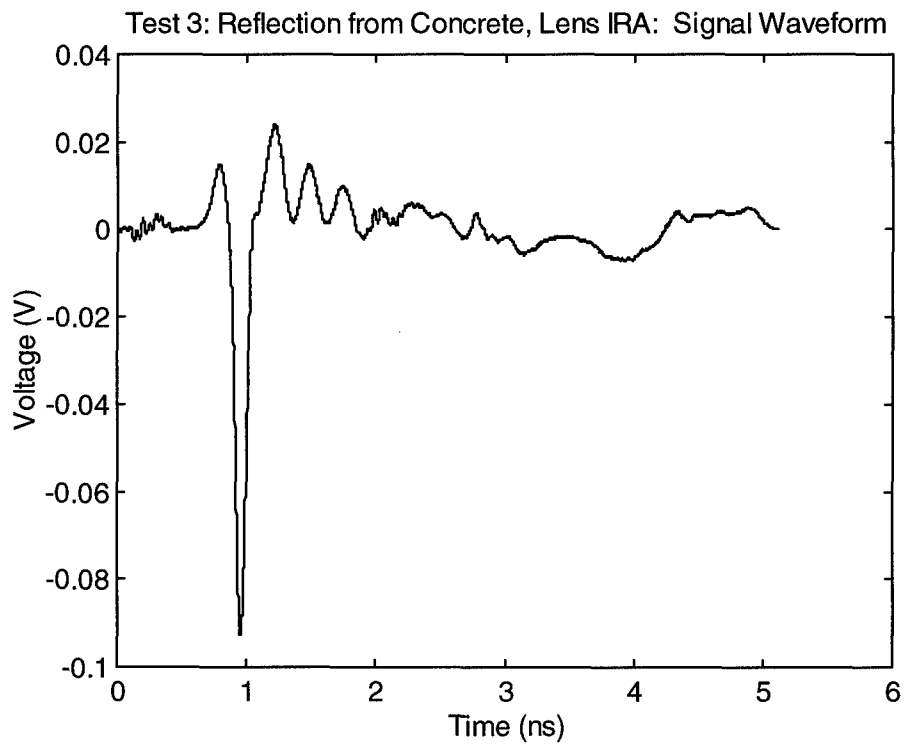


Figure 15.10. Signal waveform after background subtraction.

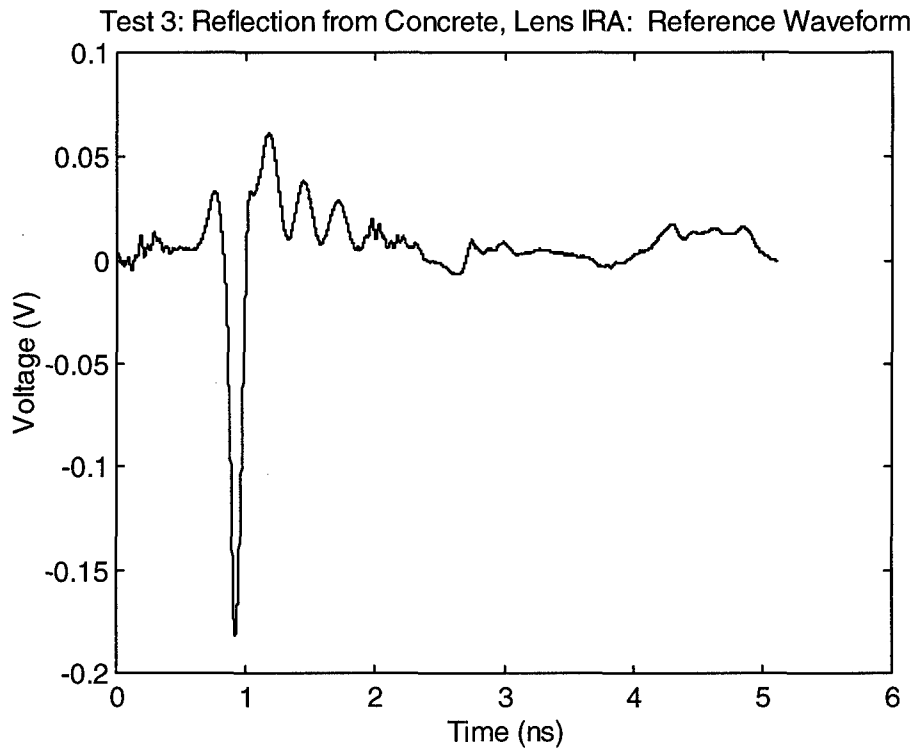


Figure 15.11. Reference waveform after background subtraction.

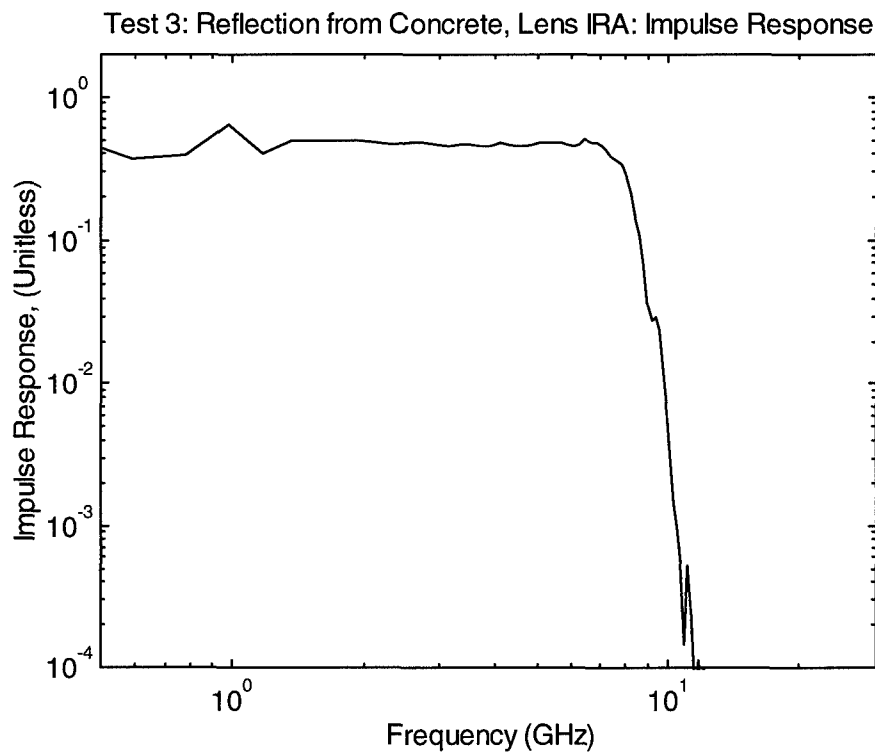


Figure 15.12. Frequency domain impulse response for concrete reflection.

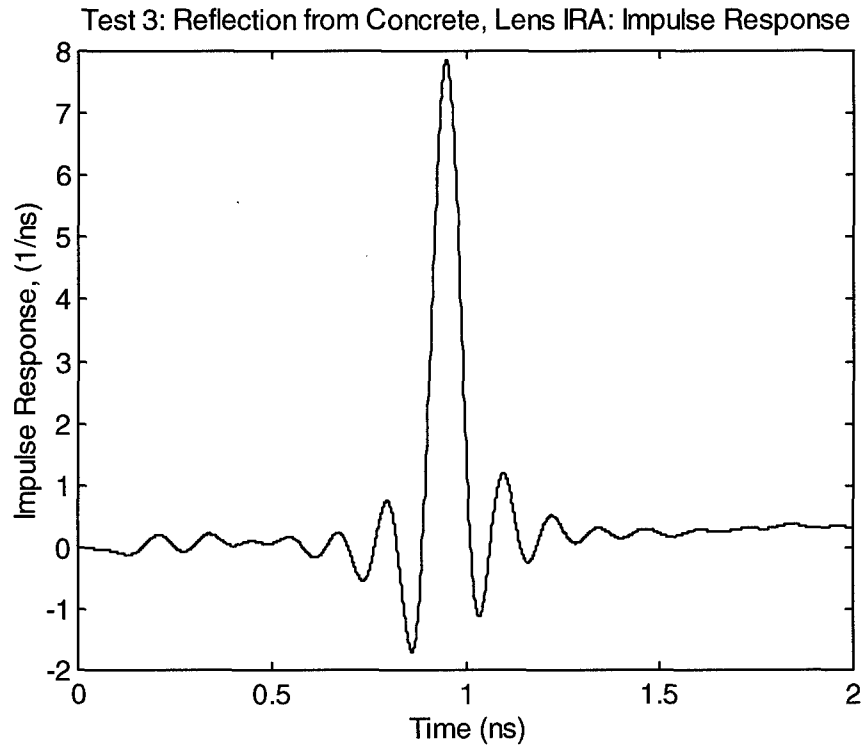


Figure 15.13. Impulse response for concrete reflection.

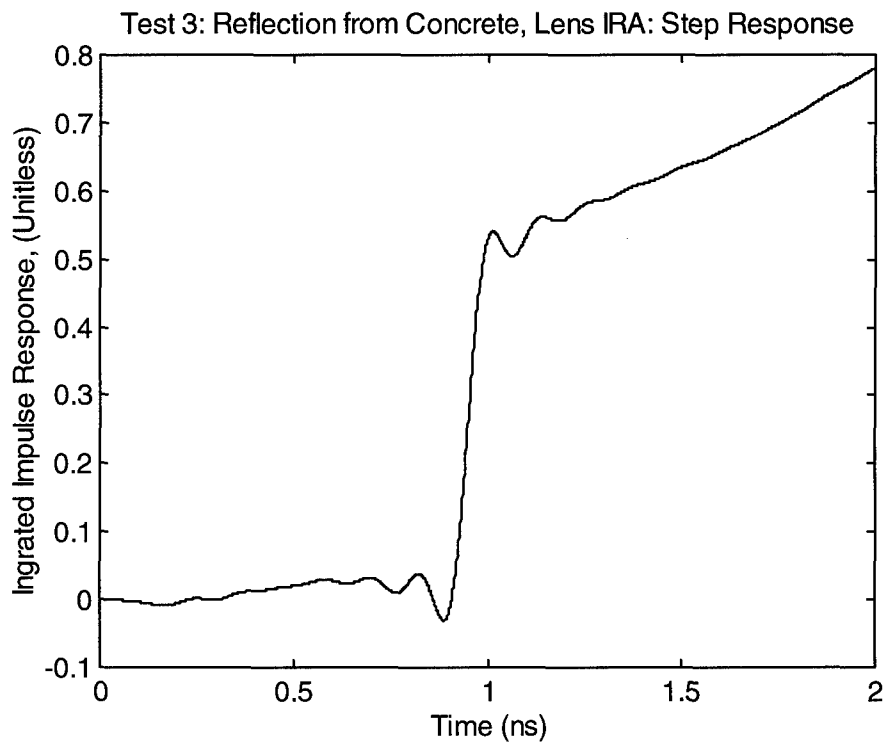


Figure 15.14. Step response for concrete reflection.

XVI. Conclusions

We have successfully measured the dielectric constant of a variety of materials using a coaxial test fixture. We have fit a model to this dielectric constant, and we have shown that the models have good predictive capability. The models have been used to model propagation through all of the materials that were studied. In each case, the agreement was excellent.

Calculations were made for longer-range propagation. These calculations imply that useful energy can penetrate the materials studied even for pulses as narrow as 30 ps out to a 10-meter distance.

We have also demonstrated a free-field method of measuring dielectric constants using a TDR technique. In the one case where we could control the material content (dry sand), we found good agreement with the coaxial test fixture measurements.

Appendix A: Correlation Between Frequency Domain and Time Domain Figures of Merit for UWB Antennas

We consider here how to convert our measured antenna parameter, $h(t)$, to something close to the IEEE definition of frequency domain gain. This may or may not be a good idea, as described below, but it is often requested of us. We consider how to implement this as well as can be done.

We begin with the standard expressions in the frequency domain. Thus, the received power is

$$P_{rec} = A_{eff} S_{inc} \quad (A.1)$$

where S is the incident power density in Watts/m² and A_{eff} is the effective aperture. Gain is related to effective aperture by

$$A_{eff} = \frac{\lambda^2}{4\pi} G \quad (A.2)$$

Combining the above two equations, we have

$$P_{rec} = \frac{\lambda^2 G}{4\pi} S_{inc} \quad (A.3)$$

Take the square root, and recast into voltages

$$\frac{V_{rec}}{\sqrt{Z_{feed}}} = \frac{\lambda \sqrt{G} E_{inc}}{2\sqrt{\pi} \sqrt{Z_o}} \quad (A.4)$$

where Z_o is the impedance of free space. Thus, the final result in the frequency domain is

$$V_{rec} = \frac{\lambda \sqrt{G f_g}}{2\sqrt{\pi}} E_{inc} \quad (A.5)$$

where $f_g = Z_{feed}/Z_o$.

Let us now compare the above equation to one that we have been using in the time domain, i.e.,

$$V_{rec}(t) = h(t) \circ E_{inc}(t) \quad (A.6)$$

where the " \circ " symbol indicates convolution. We routinely have already measured $h(t)$, so we just have to rescale to get gain. Converting this to the frequency domain, we have

$$V_{rec}(\omega) = h(\omega) E_{inc}(\omega) \quad (\text{A.7})$$

Now compare equations (5) and (7), to get

$$G(\omega) = \frac{4\pi h^2(\omega)}{\lambda^2 f_g} = \frac{4\pi f^2 h^2(\omega)}{c^2 f_g} \quad (\text{A.8})$$

We can use this to scale our $h(t)$ waveforms to get a frequency domain gain. Note the similarity between equations (A.2) and (A.8). The implication is that the effective aperture as a function of frequency is $h^2(\omega)/f_g$, which is a rather simple and pleasing result.

There is a drawback with this definition, in that it does not take into account dispersion, or time delay. If different frequencies have different time delays (as happens on more conventional antennas), the received pulse will not be clean. But the above definition of gain does not take this into account. Thus, using this definition of gain, two antennas with the same gain can have a very different peak radiated E-fields.

Using this theory, we can calculate the gain of the nine-inch diameter reflector and lens IRAs, which were originally measured in [4]. The gain of the nine-inch diameter reflector IRA is shown in Figure A.1, and the gain of the nine-inch diameter lens IRA is shown in Figure A.2. When comparing the two gains, the most striking difference is apparent at the low frequencies, between 1 and 3 GHz. The dip in $h(t)$ in this region becomes quite apparent when it is multiplied by frequency squared. We presume this dip occurs because the feed arms are not terminated in the reflector design. Future designs will include terminations of the feed arms. Even without the dip, there is a three dB advantage for the lens design.

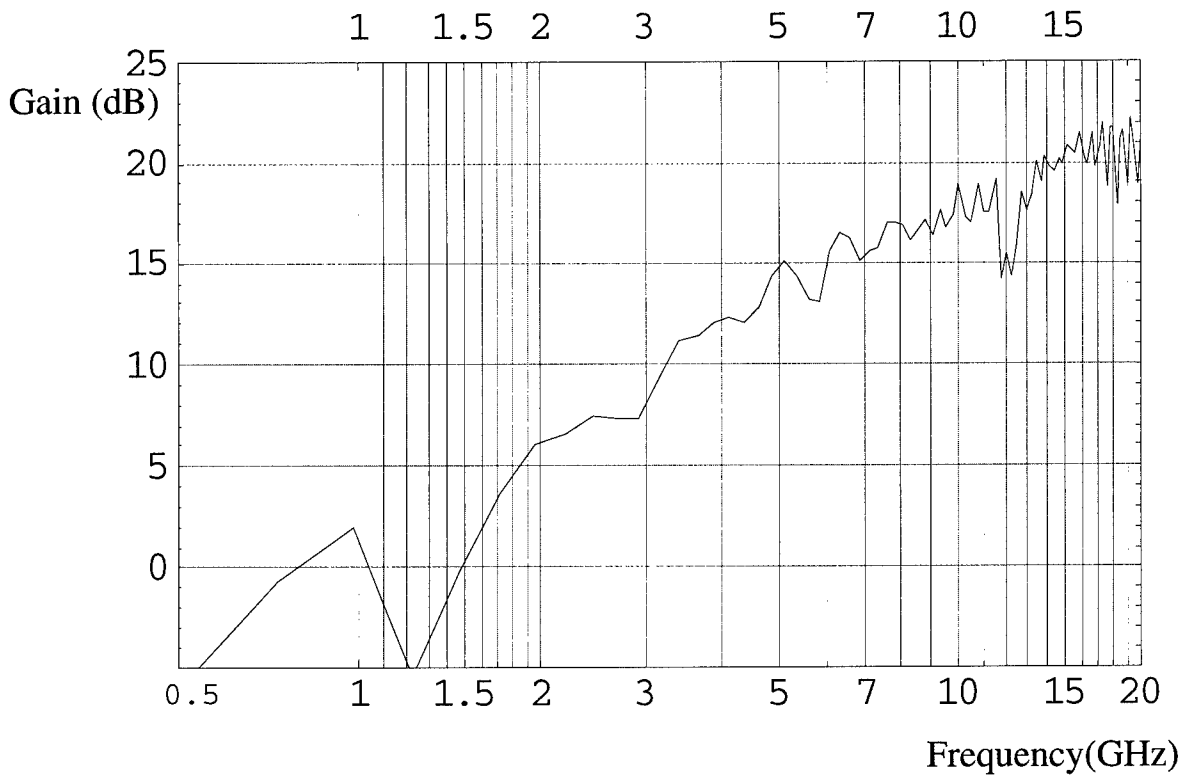


Figure A.1. Gain of the nine-inch reflector IRA.

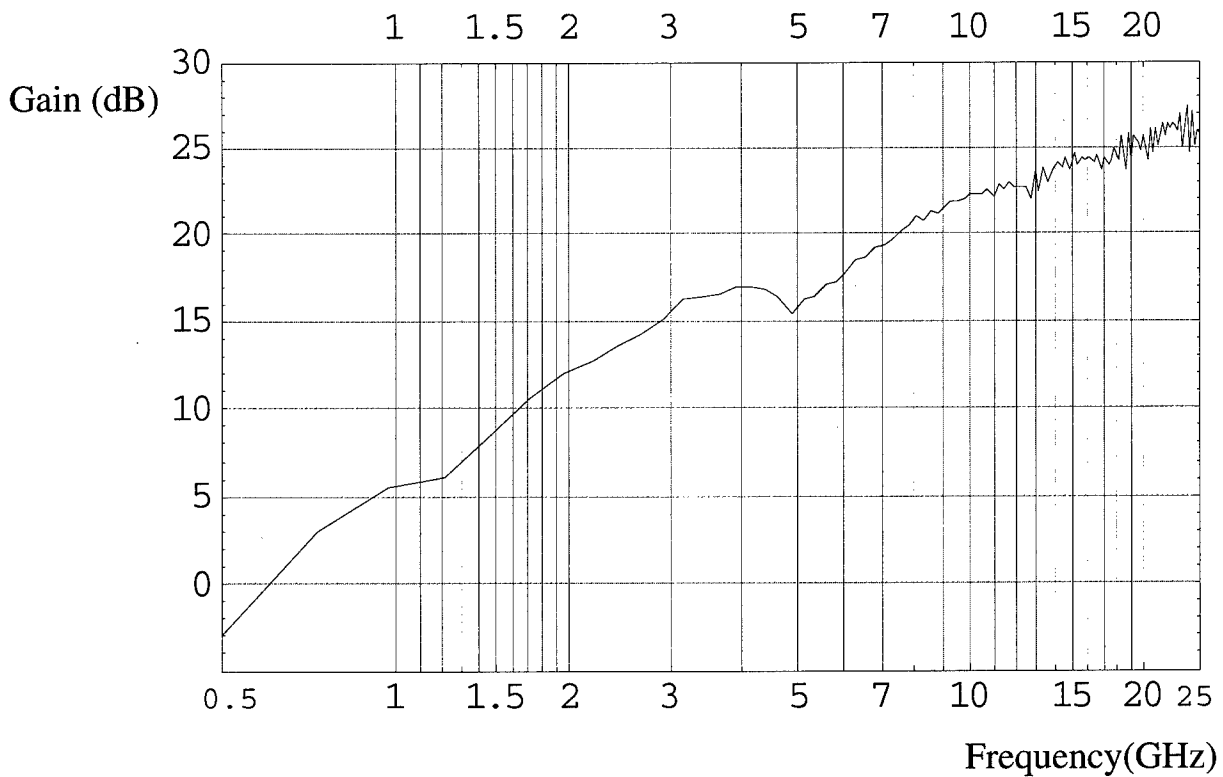


Figure A.2. Gain of the nine-inch lens IRA.

Appendix B: The Lens Effect of a Dielectric Slab

We wish to calculate here the effect of interposing a dielectric wall or slab between two antennas. Consider the configuration shown in Figure B.1, with a transmitter and receiver on either side of a dielectric slab. As a rough approximation, we can calculate the transmitted field, relative to that for free space, based on two effects. First there are Fresnel losses, which are due to reflections from either side of the dielectric slab. Second, there is a focusing effect, because the transmitter appears to move closer to the slab. This focusing effect tends to enhance the field on target, because the source appears to be closer to the wall. We can express this as

$$E_{Trans} = (\text{Fresnel losses}) \times (\text{Distance Ratio}) \times E_{Free Space} \quad (\text{B.1})$$

In other words, there are two effects at work—reflections from the front and back walls, and a field enhancement due to the virtual focus moving closer to the wall (the Distance Ratio).

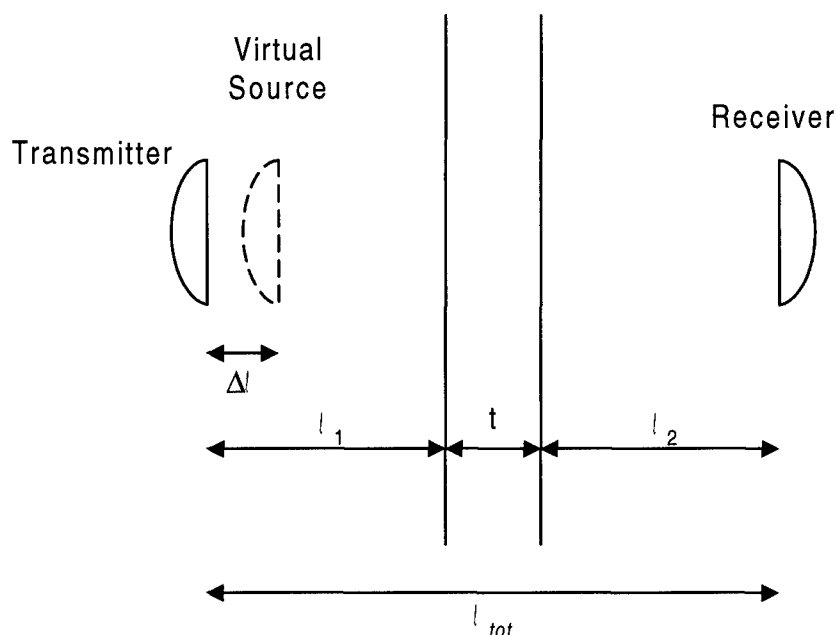


Figure B.1. Two antennas on either side of a dielectric slab, with the virtual source.

The Fresnel losses are trivial to calculate as

$$\text{Fresnel losses} = \frac{4\sqrt{\epsilon_r}}{(\sqrt{\epsilon_r} + 1)^2} \quad (\text{B.2})$$

This assumes the dielectric constant has no frequency dependence, so this is just an approximation. The distance ratio is just

$$\text{Distance Ratio} = \frac{\ell_{tot}}{\ell_{tot} - \Delta\ell} \quad (\text{B.3})$$

where ℓ_{tot} is the total distance from transmitter to receiver, and $\Delta\ell$ is the amount by which the focal length is shortened due to the slab. This gain is associated with the virtual focus of the transmitted rays moving closer to the receiver. Finally, the shift in virtual focus is

$$\Delta\ell = t \frac{\sqrt{\epsilon_r} - 1}{\sqrt{\epsilon_r}} \quad (\text{B.4})$$

where t is the wall thickness. We now derive this value of $\Delta\ell$.

To determine $\Delta\ell$, consider the geometry shown in Figure 2. This shows how a ray penetrates a dielectric slab, when it is incident at a small angle off normal θ_1 . We have invoked small-angle approximations, so the sines and tangents of all the angles are just the angles themselves.

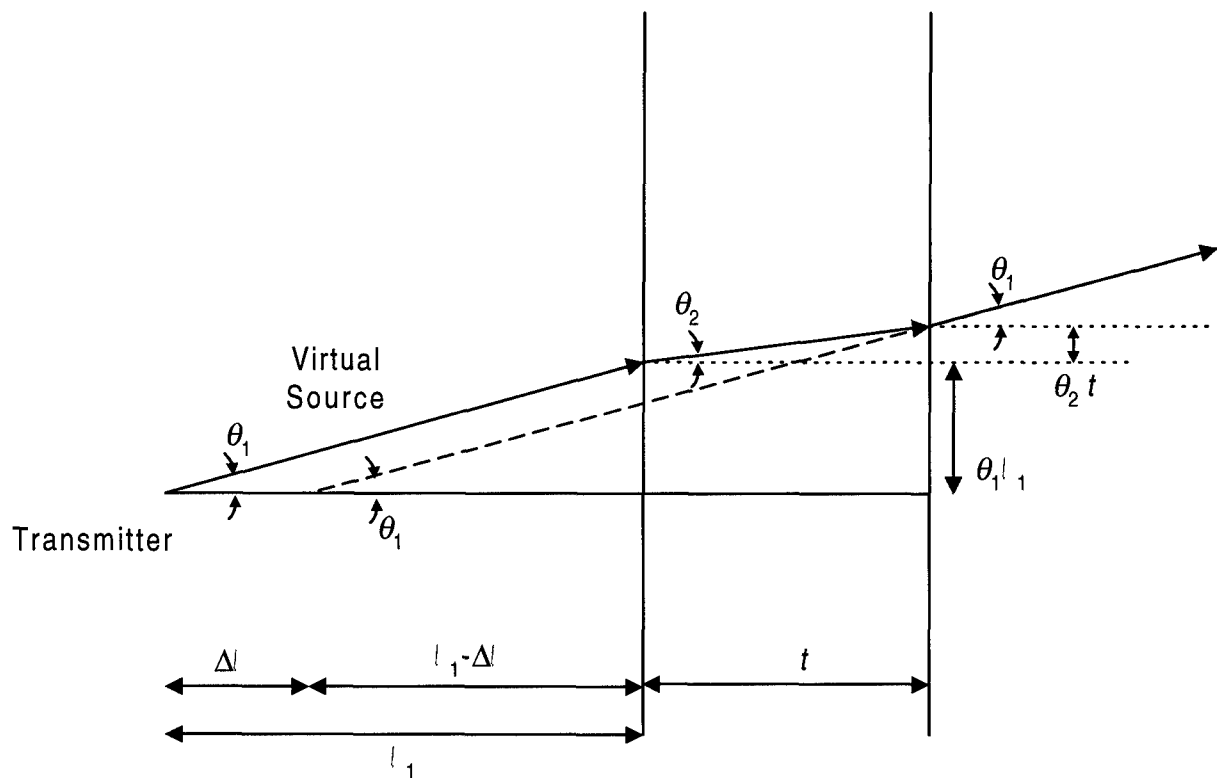


Figure B.2. Layout for determining $\Delta\ell$.

From simple geometry, we have

$$\tan(\theta_1) \approx \theta_1 = \frac{\theta_2 t + \theta_1 \ell}{t + \ell_1 - \Delta \ell} \quad (\text{B.4})$$

Snell's law is now invoked as

$$\begin{aligned} \sin(\theta_1) &= \sqrt{\epsilon_r} \sin(\theta_2) \\ \theta_1 &\approx \sqrt{\epsilon_r} \theta_2 \end{aligned} \quad (\text{B.5})$$

So if we substitute $\theta_2 = \theta_1 / \sqrt{\epsilon_r}$ into equation (B.4), we have

$$\Delta \ell = t \frac{\sqrt{\epsilon_r} - 1}{\sqrt{\epsilon_r}} \quad (\text{B.6})$$

This is the final solution for $\Delta \ell$. We can now combine the effects into a single equation,

$$\begin{aligned} E_{Trans} &= (\text{Fresnel losses}) \times (\text{Distance Ratio}) \times E_{Free Space} \\ &= \frac{4\sqrt{\epsilon_r}}{(\sqrt{\epsilon_r} + 1)^2} \times \frac{\ell_{tot}}{\ell_{tot} - t \frac{\sqrt{\epsilon_r} - 1}{\sqrt{\epsilon_r}}} \times E_{Free Space} \end{aligned} \quad (\text{B.7})$$

This is our final result.

Let us consider now an example, with $\ell_1 = \ell_2 = t = .33$ m, , and $\epsilon_r = 3.5$. These parameters are typical of some of our measurements of concrete. Using these parameters, we get Fresnel losses = 0.91, $\Delta \ell = 0.155$ m, Distance ratio = 1.18, for a total correction factor of 1.08. The result is that there has been a net gain due to the focusing effect! One might instead expect the concrete wall to reduce the field!

The above calculations are really only valid to the extent that the source appears as a single point source. In practice, the antenna is a focused aperture. Thus, the analysis is strictly valid only at distances further away than those we have calculated. In addition, real concrete has losses and dispersion, which were not included in the model. These effects may in fact prove to be more important than the effects we have calculated here.

References

(Sensor and Simulation Notes, Measurement Notes, and Theoretical Notes are all available from the Defense Technical Information Center.)

1. E. G. Farr and C. A. Frost, Ultra-Wideband Antennas and Propagation Vol.3: Time Domain Measurements of Water, Wright Laboratory Technical Report, May 1997. Also appears as Time Domain Measurement of the Dielectric Properties of Water in a Coaxial Test Fixture, Measurement Note 49, December, 1996.
2. K. S. Kunz, and R. J. Luebbers, *The Finite Difference Time Domain Method for Electromagnetics*, CRC Press, Boca Raton, 1993, pp. 124-128.
3. C. L. Longmire and H. Jerry Longley, "Time Domain Treatment of Media with Frequency-Dependent Electrical Parameters," Theoretical Note 113, September 1973.
4. E. G. Farr and C. A. Frost, Ultra-Wideband Antennas and Propagation, Vol.2: Antenna Measurements and Signal Processing, Wright Laboratory Technical Report, May 1997. Also appears as Development of a Reflector IRA and a Solid Dielectric Lens IRA, Part II: Antenna Measurements and Signal Processing, Sensor and Simulation Note 401, October 1996.

DISTRIBUTION

WL-TR-1997-7051

Defense Tech Info Center
Attn: DTIC-OCP
8725 John J. Kingman Rd, Suite 0944
Ft. Belvoir, VA 22060-6218 1

Eglin AFB offices:

WL/CA-N 1
WL/MNP-1 (Technical Library) 1
WL/MNMF 3